



Doctoral Thesis

Modelling Charge Transport in Organic Semiconducting Materials

Hui YANG

Supervisor: Prof. Jochen BLUMBERGER

Condensed Matter and Materials Physics

Department of Physics and Astronomy

University College London

August 2018

Declaration of Authenticity

I, Hui YANG, confirm that the work presented in this thesis is my own.

Where information has been derived from other sources, I confirm that this has been properly indicated in the thesis.

Acknowledgments

I would like to thank my supervisor Prof. Dr. Jochen Blumberger for his help and support. He provided guidance and encouragement throughout my project. I am also grateful to my past and present colleagues: Dr. Marian Breuer, Dr. Fruzsina Gajdos, Dr. Jacob Spencer, Dr. Guido Falk von Rudorff, Dr. Antoine Carof, Dr. Zdenek Futera, Xiuyun Jiang, Matthew Ellis, Dr. Soumya Ghosh, Samuele Giannini, Karina Chan, Dr. Ehsan Ali, Bastian Burger, Benjamin, Laura Scalfi, for their collaboration and all the discussions which helped in progressing this project.

I would like to thank the high performance computing facilities: LEGION and ARCHER and funded by UCL and CSC.

I would also like to thank my friends and family near and far for their love and support, especially Dr. Yunyan Zhang.

Abstract

Forming the active layers of organic light-emitting diodes (OLEDs), organic photovoltaics (OPVs) and organic field-effect transistors (OFETs), Organic semiconductors (OSs) have revolutionized the microelectronics industry. Compared with commonly used inorganic semiconductors, OSs combine many desirable properties: light-weight, flexible and relatively easy to produce from renewable resources. However, a drawback of OSs compared to inorganic semiconductors is their limited conductivity of electrical charges. In this thesis, I study charge transport properties of OSs in order to aid their material and structure design and to improve device efficiency.

In this work, I evaluate the performance of a systematic and sophisticated computational tool for the prediction of charge mobilities in OSs. The method is based on the assumption that the charge carrier is localized, i.e. forms a small polaron that hops from one molecule to the next. Molecular dynamics simulation and first-principle calculations are used to calculate rate constants for each polaron hopping step and kinetic Monte Carlo simulations are carried out to compute the mobility from the set of hopping rate constants. The methodology is applied to hole hopping in single crystalline benzene, rubrene, pentacene, anthracene and electron hopping in C_{60} . To find structure - property relations linking the morphology with the bulk charge carrier mobility, the methodology is further applied in few-layer thinfilm pentacene and amorphous pentacene.

Impact Statement

This thesis explains and discusses theories in use for describing charge transport (CT) in organic semiconductors (OSs) and characterizes computationally the CT properties of a number of application-relevant organics. This work includes not only well-adapted state-of-the-art methodology but also insightful numerical calculations of CT parameters. First, charge transfer is explored by inspecting the behaviour of the electronic couplings and site energies as a function of temperature in prototypical single crystalline OS formed by four organic molecules that are of different chemical structure: rubrene, pentacene, C₆₀ and anthracene. Second, structure-property relations are investigated for CT in different solids formed by pentacene: from single crystals, to experimentally characterised ordered thin films to fully disordered amorphous samples. My research findings have been presented in several international conferences or seminars, such as a CECAM workshop. After my talk at CECAM I had the opportunity to discuss my results with two engineers from IBM and Samsung Display. My publication in *J. Phys. Chem. C* has been cited 7 times since 2017.

Contents

Acknowledgments	3
Abstract.....	4
Impact Statement.....	5
Contents.....	6
Table of Figures	9
Table of Tables	14
Abbreviations	15
1 Background and Motivation	17
2 Charge Transport Theory in Organic Semiconductors	22
2.1 Polaron hopping model	22
2.1.1 ET rates.....	24
2.1.2 Adiabatic vs nonadiabatic limit	26
2.1.3 ET parameters	28
2.1.4 Charge carrier mobility.....	34
2.1.5 Kinetic Monte Carlo simulation of mobility	35
2.2 Band transport model.....	37
2.2.1 Comparison between the bandstructure of inorganic and organic semiconductor	38
2.2.2 Band transport mobility	39
2.3 Beyond hopping and band transport	41
3 Organic Single Crystals	43
3.1 Material systems	44
3.1.1 Benzene crystal	44
3.1.2 Rubrene crystal	45
3.1.3 Pentacene crystal	47
3.1.4 Buckminsterfullerene C ₆₀ crystal.....	48
3.1.5 Anthracene crystal	49

3.2 Computational details	50
3.2.1 Workflow of polaron hopping simulation in molecular organics	50
3.2.2 Force field parameterization.....	52
3.2.3 Molecular dynamics simulation	54
3.2.4 ET parameters	55
3.2.5 ET rates.....	56
3.2.6 Charge mobility.....	57
3.3 Validation of simulation protocol: benzene	58
3.3.1 Validation of force field for MD	58
3.3.2 Electronic couplings in benzene.....	59
3.3.3 Site energy in benzene.....	62
3.3.4 Frequency analysis for benzene crystal.....	66
3.3.5 Mobility calculation and convergence of KMC.....	67
3.4 Rubrene, Pentacene, and C₆₀	69
3.4.1 Thermal distributions of electronic couplings.....	69
3.4.2 Thermal distributions of site energies.....	73
3.4.3 Timescales of fluctuations.....	75
3.4.4 Existence of small polaron	76
3.4.5 Charge mobility.....	79
3.5 Band mobility of 1D-chain anthracene.....	84
3.5.1 Computational details	84
3.5.2 Dispersion corrections for density functional theory.....	87
3.5.3 Size convergence for me, El	88
3.5.4 Band, hopping and experimental mobilities	90
3.6 Summary	93
4 Pentacene Thin Films	96
4.1 Structure of thin film pentacene	97
4.1.1 Experimental observation	97
4.2 Set up of simulations	101

4.2.1	Periodic box size for thin film model.....	101
4.2.2	Structure and force field for pentacene layer on BN	102
4.2.3	Restraining pentacene layers with collective variables.....	105
4.3	Results and discussion	108
4.3.1	Intralayer and interlayer electronic couplings	108
4.3.2	Charge carrier hopping.....	111
4.3.3	Charge mobility	113
4.4	Summary.....	113
5	Pentacene Amorphous Solid	115
5.1	Amorphous materials and controlling of the growth.....	115
5.2	Disorder morphologies - structural modelling.....	118
5.2.1	Set up of quenching process	118
5.2.2	Structures – How amorphous are the disorder systems?	121
5.3	CT Results and discussion	127
5.3.1	Electronic coupling	127
5.3.2	Charge mobility	129
5.4	Summary.....	130
6	Conclusion and Outlook	132
6.1	Conclusion.....	132
6.2	Outlook	135
References.....		137
Appendix.....		152

Table of Figures

Figure 1-1 Illustration of the ranges of validity of hopping models (orange) and band models (blue). Ranges of the validity criterion depending on intrinsic materials' properties are depicted as shade areas of the respective bars.....	18
Figure 2-1 Free energy curves for electron transfer between electron donor (D) and acceptor (A)... .	23
Figure 2-2 ET free energy curves for large ratios H_{ab}/λ	28
Figure 2-3 Comparison between the energy-dispersion relationships of typical inorganic and organic (calculated by DFT). (a) The bandstructure of Si. (b) The bandstructure of a rubrene single crystal.....	38
Figure 3-1 The unit cell of crystalline benzene (left) and a snapshot of molecular dynamics at 150K (right).	45
Figure 3-2 A schematic diagram of a rubrene molecule (left top), the unit cell of crystalline rubrene (left bottom) and a snapshot of molecular dynamics at 283K (right).....	47
Figure 3-3 The unit cell of crystalline pentacene (left) and a snapshot of molecular dynamics at 283K (right).	48
Figure 3-4 A schematic diagram of a C_{60} molecule (left) and the unit cell of crystalline C_{60} (right)..	49
Figure 3-5 The snapshots of anthracene crystal within herringbone layer (left) and from side view (right).	50
Figure 3-6 Workflow of polaron hopping simulation in OSs.....	51
Figure 3-7 Experimental and computational comparison of density vs. temperature.....	59
Figure 3-8 Radial distribution function $g(r)$ of center of mass of benzene molecule as obtained from 1 ns MD trajectory at 138 K.	60
Figure 3-9 Spacing and orientation for selected donor-acceptor configurations (in pink) in a benzene unit cell..	61
Figure 3-10 The distribution of site energy differences over the benzene molecular trajectory at 150K.	62

Figure 3-11 Cosine Fourier transform of the autocorrelation function of the vertical energy gap for the excited state on one site in the crystal at 150K.....	63
Figure 3-12 Experimental Raman spectrum of benzene, in powder, with the main peaks marked.	64
Figure 3-13 Illustration of vibration in benzene for: (a) C-C-C stretching vibration mode; (b) benzene ring breathing vibration mode; (c) C-C-C deformation in plane vibration mode; (d) C-H shear vibration mode.....	65
Figure 3-14 Time scale of rates k_{ij} and cosine transform of the autocorrelation function of the vertical energy gap of the excited states ΔE_{ij} and the electronic coupling between the excited states of the neighboring molecules in benzene at 150K.....	67
Figure 3-15 Mobilities computed by Einstein method.	69
Figure 3-16 (a)-(c) Orientation of nearest neighbour molecular pairs in pentacene (a), rubrene (b) and C_{60} (c) crystals. Arrows at the right bottom corner in each panel point in the direction of eigenvectors of the mobility matrix for each system. (d)-(f) Distribution of electronic coupling matrix elements $ H_{ij} $ for hole transfer between nearest neighbor pairs in rubrene (d) and pentacene (e), and for electron transfer in C_{60} (f). The data are obtained from 1 ns MD simulation at 300 K. The overall distribution is shown in black and the decomposition in contributions from different directions is shown in colour. P and T denote parallel and transverse direction, respectively. (g)-(i) The overall distributions of electronic coupling matrix element for all nearest neighbor pairs at different temperatures for rubrene (g), pentacene (h) and C_{60} (i).	73
Figure 3-17 Temperature sensitivity of site energy difference distribution from 1ns-long MD simulation for nearest neighbours for pentacene.....	74
Figure 3-18 (a) Distribution of site energy difference from 1ns-long MD simulation for nearest neighbours at 300K. (b) Linear relationship between variance of site energy difference and temperature.	74
Figure 3-19 Frequency analysis of ET parameters electronic coupling (green) and site energy difference (blue) for rubrene (a) and C_{60} (b) at room temperature. The distributions for the corresponding inter-molecular charge transfer rates are shown in red.....	76

Figure 3-20 Distribution of activation free energy when average site energy differences are used for inter-molecular charge transfer in rubrene, pentacene and C ₆₀	78
Figure 3-21 Charge hopping mobilities at room temperature as obtained from KMC simulation.	80
Figure 3-22 Comparison of computed mobilities with experimental mobilities and their anisotropy for rubrene(a), pentacene(b) at room temperature.....	81
Figure 3-23 Mobility decay with temperature for rubrene (a) and pentacene (b).	83
Figure 3-24 1D chain anthracene (highlight) from a single crystal along b-axes.	86
Figure 3-25 The total energy E _{tot} against periodic cell length (normalized with experimental length) a along 1D anthracene.	88
Figure 3-26 (a) HOMO band in b-1 direction in 1D chain anthracene with different size of periodic cell. These periodic cells consist 3, 5 and 7 molecules, respectively. (b) converged curvature of HOMO band by rescaling them with the cell length for 3, 5- and 7- molecule systems.....	89
Figure 3-27 The E _{vbm} against periodic cell length, normalized a, along the b direction of anthracene with different size of periodic cell.....	90
Figure 3-28 Orientation of nearest neighbour molecular pairs in anthracene crystal within herringbone layer (a) and from side view (b).	91
Figure 3-29 Mobility decay with temperature along the direction b. Band, hopping and experimental mobilities are compared.....	92
Figure 4-1 Epitaxial growth of 2D pentacene crystals on BN. (a) Schematic illustration of the molecular packing of WL, 1L, and 2L within b-c plane. (b) Histogram distribution of the thickness of WL, 1L, and 2L, each taken from over 10 samples. (c) Raman spectrum of the pentacene crystals on BN, taken from a 2L sample. (d)–(f) AFM images of WL, 1L, and 2L pentacene crystals on BN, respectively.	99
Figure 4-2 Molecular packing of 1L (lower panel in blue) and 2L (upper panel in pink) pentacene within (a) b-c plane (b) a-c plane (c-d) a-b plane.	100
Figure 4-3 illustration of unit cell for (a) (c) bulk and (b) (d) thin film. a,b,c are lattice parameters. (a)(b) are b-c plane and (c)(d) are a-b plane..	100
Figure 4-4 The side view of periodic cell for (a) 1L model (b) 2L models.....	101

Figure 4-5 The top view of periodic cell for WL pentacene on the BN substrates.....	102
Figure 4-6 Similarity of geometry for (a)graphite and (b)hexagonal boron-nitride.....	103
Figure 4-7 (a) STM images for lying-down pentacene monolayer on graphite. (b) Schematic drawing of unit cell of lying-down pentacene monolayer on graphite.....	104
Figure 4-8 Generation of force field of hBN. (a,b) Top view and side view of pentacene on hBN. (c) parameterized FF to reproduce DFT potential of scanning the distance d in (b).....	105
Figure 4-9 The side view of periodic cell for double-layer pentacene system. (a) initial motif built based on experiment geometry (b) structure after minimization using current force field.	107
Figure 4-10 Restrain force constant for colvars v.s.tilt angle distribution of pantacene in 2L (top) and in 1L (bottom) in 1ns long NVT MD....	108
Figure 4-11 (a-b) Orientation of nearest neighbour intralayer pairs t_1 , t_2 , t_a (a) and interlayer pairs t_{1L-2L} and t_{WL-1L} (b). (c-d) Distribution of electronic coupling matrix elements $ H_{ij} $ for hole transfer between nearest neighbor pairs within herringbone layer (c) and across herringbone layer (d).	109
Figure 4-12 Dynamic distribution of the holes before and after hopping for WL+1L system.	111
Figure 4-13 Dynamic distribution of the holes before and after hops for WL+1L+2L system.	112
Figure 5-1 (a) Diffraction spectra for as-grown pentacene films. the film-formation temperature ranges from 28K to 300K. (b) XRD spectra of the pentacene films fabricated by evaporating at rates of 1, 3, 5, and 7 Å/s at 25 °C room temperature, and 7 Å/s at 60 °C.....	117
Figure 5-2 (a)Snapshots of crystallian pentacene melting to amorphouse phase at 800 K in the MD simulation. (b) The radial distribution functions g(r) of the center of mass of molecules when the MD simuations last 100, 200, 700, and 1000ps..	119
Figure 5-3 (a-b) Quenching simulations for melted pentacene from 800 K to 300 K in a NPT ensemble in the distinct time scales of 10ns, 1ns, 100ps and 10ps, respectively. (c-d) During the NPT simulations, the simulation cell shrank and finally reached a constant volume.....	121
Figure 5-4 Schematic diagram of disordered pentacene obtained after quenching process. (a) High density system after fast cooling includes many (shift) cofacial configurations due to molecule self-assembling. (b) Low density system after slow cooling is amorphous....	122

Figure 5-5 The radial distribution functions for the single crystal pentacene (in black), melted phase at 800K (in blue), the high density phase relaxing with fast cooling (in green), and the low density phase relaxing with slow cooling (in green).	124
Figure 5-6 (a) Schematic diagram of three orthogonal vectors for each molecule in the disordered pentacene. V1 is along the long molecular axes; V1 and V2 form the the plane of the molecular backbone; V3 is orthogonal to this plane. (b-d) The thermal distribution of cosine of the angles between neighboring molecules for each of these three vectors....	126
Figure 5-7 (a-b) Electronic coupling matrix elements $ H_{ij} $ versus intermolecular centre-to-centre distance for (a) the high density disordered pentacene and (b) the low density disordered pentacene. (c) Distribution of $ H_{ij} $ for hole transfer between nearest neighbor pairs....	128
Figure 5-8 Charge hopping mobilities for disordered pentacene at room temperature as obtained from KMC simulation.. ..	130

Table of Tables

Table 3-1 Lattice parameters of benzene, rubrene, pentacene, C ₆₀ and anthracene crystals	43
Table 3-2 Summary of reorganization energies from DFT and force field.....	53
Table 3-3 Experimental and computational comparison of density vs. temperature	58
Table 3-4 Summary of rates constant and mean values of electric couplings for inter-molecular hole transfer in benzene.....	60
Table 3-5 Comparison of experimental Raman spectrum and computational spectrum by E_{ij} frequency analysis for benzene and the corresponding vibration modes	65
Table 3-6 Mean values ($\langle H_{ij} \rangle$) and root-mean square fluctuations (σ) for electronic coupling matrix elements for inter-molecular hole transfer in rubrene and pentacene and for electron transfer in C ₆₀	70
Table 3-7 Comparison of computed mobilities from the literature and from current work with experimental mobilities at room temperature.....	81
Table 3-8 Electronic coupling matrix elements for intermolecular hole transfer in anthracene	91
Table 4-1 Experimental lattice parameters of pentacene bulk, thin film, 1L, 2L and WL motifs.	98
Table 4-2 Relation of restrain force constant for colvars and tilt angle pentacene.	108
Table 4-3 Comparison of electornic coupling values for the similar orientational configurations of crystallian, thin film and amorphous pentacene. T ₁ , T ₂ and P pairs are in the bulk. t _a , t ₁ and t ₂ pairs are in the thin film.The values in brackes are the corresponding center-to-center distance.	110
Table 4-4 Comparison of computed mobilities of TF and single crystal from current work with experimental mobilities from the literature at 110K ^a	113

Abbreviations

2D	two-dimensional
3D	three-dimensional
AFM	atomic force microscopy
Amber	Assisted Model Building with Energy Refinement
AOM	analytic overlap method
CBM	conduction band minimum
CCDC	Cambridge Crystallographic Data Centre
CGs	contracted Gaussians
colvars	collective variables
COM	center of mass
CPMD	Car–Parrinello molecular dynamics
CT	charge transport
DFT	density functional theory
ET	electron transport
FCC	face centered cubic
FF	force field
GAFF	generalized Amber force field
GGA	generalized gradient approximation
hBN	hexagonal boron nitride
HOMO	highest occupied molecular orbital
KMC	kinetic Monte Carlo
LUMO	lowest unoccupied molecular orbital
MD	molecular dynamics
MQC-NAMD	quantum-classical non-adiabatic molecular dynamics
MRCI	multi-reference configuration interaction
NEVPT2	N-electron valence state perturbation theory
OFET	organic field-effect transistors
OLED	organic light-emitting diodes
OPV	organic photovoltaics
OS	organic semiconductor
PBC	periodic boundary condition
PBE	Perdew, Burke, and Ernzerhof
PVD	physical vapour deposition
RESP	restrained electrostatic potential
RMSD	root-mean-square deviation
SAED	selected-area electron diffraction
SOMO	singly occupied molecular orbital

STO	Slater-type orbital
TEM	transmission electron microscopy
TF	thin film
VBM	valence band maximum
vdW	van der Waals
WL	wetting layer
XRD	X-ray diffraction

1 Background and Motivation

The interest in electron transport (ET) in organics has grown rapidly in recent years both in industry and in academia.¹⁻⁴ On the application side, organic semiconducting materials have the advantages of easy fabrication, mechanical flexibility, and low cost with a wide range of applications, like organic light-emitting diodes (OLED),⁵ organic field effect transistors^{3,6} and organic photovoltaics (OPVs);⁴ a number of chemical companies worldwide, such as BASF and Merck, have been involved in leading the development of organic electronics. On the applied research side, π -conjugated materials in general attract a great amount of interests, from fundamental study including theory investigation and experiment characterization to applied level, like the organics devices design and integration.

The performance of the organics devices mentioned above critically depends on the efficiency of charge transport in the π -conjugated materials. The key quantity that characterizes charge transport is the carrier mobility. There are several widely referenced experimental techniques to measure the carrier mobilities: time-of-flight, field-effect transistor configuration and diode configuration.¹

However, ultrapure samples of OSs are very difficult to prepare experimentally and the charge mobility is critically sensitive to defects.⁷ This experimental drawback sometimes misleads the understanding of the nature of charge transport. For example, incoherent hopping was observed in major organic conjugated crystals a couple of

decades ago,⁶ which was regarded as the transport mechanism in organics, while more recent measurements on highly purified samples show that the presence of defects led to the activated hopping.⁸

Computational simulation is a modern tool to reveal the properties of the pure materials, which avoids the problem discussed above. Furthermore, to complement real experiments, atomic modelling can provide parameters that cannot or only indirectly be obtained from experiment, such as electronic coupling between molecules.

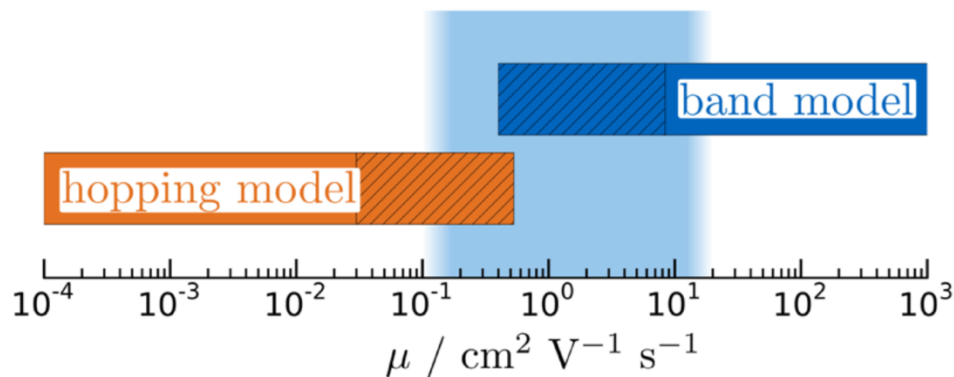


Figure 1-1 Illustration of the ranges of validity of hopping models (orange) and band models (blue). Ranges of the validity criterion depending on intrinsic materials' properties are depicted as shade areas of the respective bars. The bright blue box in the background depicts the range of charge mobilities of common materials with data taken from ref⁹. Plot from¹⁰

There are two established theories to describe ET, one is band theory^{11,12} in which an electron is assumed to be delocalized like the conduction mechanism of inorganic semiconductors. Band-theory approaches are inapplicable at ambient temperatures where the mean free path is shorter than the intermolecular lattice spacing.¹³ Hence, over the last ten years, most of the theoretical/computational studies have assumed a

charge hopping mechanism,^{2,4} but doubt has been cast as well over the validity of this model.¹⁴⁻²¹ The presence of the charge carrier creates an energy well deep enough for the carrier to localize on a single molecule. This is called a small polaron. As we will see in the following chapter, this is the case when the reorganization energy (also termed as local electron-phonon coupling or trapping energy) is larger than the electronic coupling between the molecules. In a recent review the validity regimes of the band and hopping models have been discussed and estimated using a simple model. It was suggested that band theory is valid when the mobility is high $> 10 \text{ cm}^2/\text{V}\cdot\text{s}$ and the hopping model is valid when the mobility is low $< 0.1 \text{ cm}^2/\text{V}\cdot\text{s}$, see Figure 1-1. Both models may be used for the regime between these two limits.

There are two other approaches that have been introduced. One is polaronic band theory where nuclear motion is explicitly considered in the Hamiltonian in form of on-site electron nuclear coupling (local electron-phonon coupling or Holstein term) and the other describing fluctuations of electronic coupling (non-local electron-phonon coupling or Peierls term). While this model improves on simple band theory, it also assumes that the charge carrier forms a delocalized band, which breaks down at higher temperatures. More recently, atomistic simulation techniques based on non-adiabatic molecular dynamics have been suggested to address the problem of charge transport in organics. While first application is promising, these simulations are computationally expensive and are still limited to relatively small systems.

The aim of this thesis is the computational characterization of the charge transport properties of a number of application-relevant organic semiconductors. In the first part of this thesis I probe the impact of thermal fluctuations on charge transport properties in prototypical single crystalline OS formed by four organic molecules of different chemical structure: rubrene, pentacene, C₆₀ and anthracene. This analysis permits me to obtain theoretical insight into possible charge transport mechanism in these materials. In the second part of this thesis I select one molecule, pentacene, to study the charge transport properties in different solids formed by this molecule: from single crystals, to experimentally characterised ordered thin films to fully disordered amorphous samples. This study permits me to obtain some insights into how solid state order impacts on charge transport properties.

Chapter 2 describes traditional charge transport models for OSs and recent developments of computational approaches. In this chapter all ET parameters that are calculated in later chapters are defined and it is explained how they are used for the calculation of charge carrier mobility.

In Chapter 3 the experimental crystal structures of pentacene, rubrene, C₆₀ and anthracene are presented. The details of the calculation of electron transfer parameters are reported including a detailed description of the electron hole mobility calculation for these materials using Kinetic Monte Carlo. The temperature dependence of the CT

parameters is discussed in detail and the computed mobilities is compared with experiments. The validity of the hopping model is discussed in detail.

In Chapter 4, I move the intrinsic charge transport study from the three-dimensional perfectly crystalline systems down to two-dimensional thin film. In this chapter, models of few-layer crystalline pentacene thin film (based on the experimental structure) have been built and stabilized on hexagonal boron nitride (hBN) in molecular dynamics using suitably chosen restraining potentials. Electronic transport parameters and charge mobilities within and across layers have been computed with the same computational approaches and the results were then compared to calculations on the single crystals that are presented in Chapter 3.

In Chapter 5 structural modelling and mobility calculations are presented for amorphous pentacene. Systems that generated via melting crystalline structures at various cooling rates are characterized. Furthermore, thermal distributions and average values between pairs of ET parameters are compared within amorphous motif and within 2D and 3D crystalline pentacene showed in the previous two chapters.

In the last chapter, I conclude this thesis and suggest further avenues of investigation.

2 Charge Transport Theory in Organic Semiconductors

Systematic development OSs requires a sophisticated and experimentally-validated model that can guide materials and device design as a true predictive tool. In this chapter, I will present two commonly assumed charge transport models, polaron hopping and band-like transport, as well as their limitations. Also, I will introduce the methodology of mobility prediction used in this thesis, which is based on polaron hopping model and combines multi-scale simulations.

The mechanism of charge transport (CT) in organics is still very much debated. There are two established models to describe CT in OSs, which differ in the degree of the localization of the carrier. One model is based on polaron theory^{22,23} in which charge carriers are assumed to be localized and hop between molecules. The other is based on band theory^{16,24} in which the charge carrier is assumed to be delocalized like in inorganic semiconductors. However, both models have their limits. Polaron hopping model applies if localized charge carrier and an activation barrier exist, whereas the band model applies if the mean free path of the carrier is larger than the lattice spacing.

2.1 Polaron hopping model

In the limit of small electronic couplings and high reorganization energy (or local electron-phonon coupling), polaron hopping model applies where the charge carrier

is localized on one molecule and brings about the lattice's local deformation (so called 'small polaron'). Charge transfer occurs at a transition state, and the system overcomes a barrier (an infrequent Markovian process). The nuclear configurations of initial and final polaronic states are energetically degenerate. The process can be graphically expressed with two parabolas if we assume it a simple harmonic response, see Figure 2-1. The ET reactions picture draws on the concepts of transition state theory of chemical reactions²⁵ and Landau–Zener theory^{26,27} for electronic transitions.

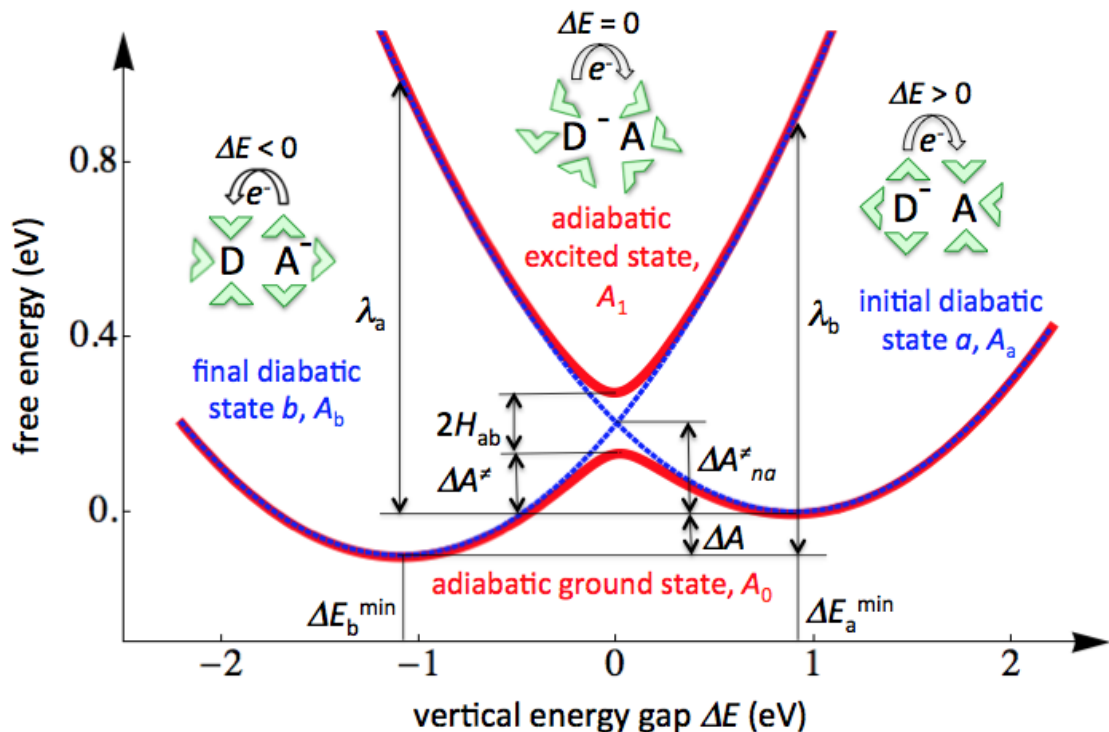


Figure 2-1 Free energy curves for electron transfer between electron donor (D) and acceptor (A). Diabatic and adiabatic free energy curves are shown in blue and in red, respectively. The environment is in green. For further details see text. The plot is from ref²⁸.

The plot describing ET reactions is free energy A (termed as G in some literatures) vs reaction coordinate generally, but the vertical diabatic energy gap ΔE is used here as the reaction coordinate, which follows Zusman and Warshel's pioneering works in

order to avoid an erroneous description of the reaction pathway. In Figure 2-1, each parabola represents a diabatic state of the system (in blue): one for the initial state a with the charge at donor (D), and one for the final state b with the charge at acceptor (A). The energy gap ΔE is a measure for the energetic preference of the electron to be on site of D rather than A, and it depends on atomic configuration of D and A and the dipolar orientation of the environment. The free energy difference between the two minima on the diabatic surfaces is the driving force ΔA which drives electron transfer. It is proportional to the ratio of configurational partition sums for E_a and E_b . The energy split between two adiabatic states is two times of electronic coupling H_{ab} (also termed as H_{ij} in this thesis). It is an essential parameter determining ET rates and mobilities and its explicit definition is given in Section 2.1.3.

2.1.1 ET rates

Charge transfer occurs when thermal fluctuations are large enough. The system is initially at the bottom of the well of the initial state, reaches the point where initial and final states cross (so called transition state), and then ends up at the bottom of the final state after thermal relaxation. The electron can hop from the initial to the final diabatic state with a probability given by Landau–Zener theory.^{26,27}

The ET rate in the donor-acceptor configuration can be simply described by a simple generalized expression^{29,30}

$$k = \kappa_{el} v_n \exp\left(-\frac{\Delta A^\dagger}{k_b T}\right) \quad (1)$$

where κ_{el} is the electronic transmission coefficient, v_n is an effective nuclear frequency along the reaction coordinate, ΔA^\dagger is the ET activation free energy. The electronic transmission coefficient is given by

$$\kappa_{el} = \begin{cases} 2P_{LZ} / (1 + P_{LZ}) & \text{if } \Delta A \geq -\lambda \\ 2P_{LZ} (1 - P_{LZ}) & \text{if } \Delta A < -\lambda \end{cases} \quad (2)$$

$$P_{LZ} = 1 - \exp(-2\pi\gamma) \quad (3)$$

$$2\pi\gamma = \frac{\pi^{3/2} |H_{ij}|^2}{hv\sqrt{\lambda k_B T}} \quad (4)$$

where P_{LZ} is the Landau-Zener transition probability for a single crossing event from the initial to the final diabatic state surface, $2\pi\gamma$ is adiabaticity parameter, h is Planck's constant, H_{ij} is the electronic coupling matrix element, and λ is the reorganization free energy. See section 2.1.3 for an explicit expression of the latter two parameters.

ET activation free energy ΔA_{ij}^\dagger in Eq 1 (when driving force is zero) takes the form³¹

$$\Delta A_{ij}^\dagger = \frac{\lambda_{ij}}{4} - \left(|H_{ij}| - \frac{1}{\lambda_{ij}} |H_{ij}|^2 \right) \quad (5)$$

It is noted that the expressions Eqs. 1 and 5 are valid in both the non-adiabatic and adiabatic limits and any intermediate regimes. The first term on the right hand side of Eq 5 is the usual expression for non-adiabatic (Marcus) ET. The second term is a

correction that becomes important in the adiabatic regime, where electronic coupling is typically an order of magnitude smaller than reorganization free energy.

From Eqs 1-5, we notice that, the ET rates within the hopping model is fully determined by the quantities H_{ab} , λ , ΔA (site energy difference in electric field free simulations) and v_n . The explicit expressions and computational techniques for these parameters will be discussed in section 2.1.3.

2.1.2 Adiabatic vs nonadiabatic limit

In the adiabatic limit, the adiabatic electronic wavefunctions change slowly as the system reaches the transition state and cross the activation barrier gradually to the final potential well.³² In this case H_{ab} is relatively large but still smaller than $\lambda/2$. As a result, adiabaticity factor $2\pi\gamma \gg 1$ in Eq 3, and Landau-Zener transition probability P_{LZ} approaches unity, thus electronic transmission coefficient κ_{el} is close unity. It means that the system has very high probability of crossing transition state from initial state to final state.

In the opposite, nonadiabatic limit where $H_{ab} \ll \lambda$, the adiabatic electronic wavefunction changes suddenly at the transition state. Adiabaticity factor $2\pi\gamma \ll 1$, resulting in $P_{LZ} = 2\pi\gamma$ and $\kappa_{el} = 2P_{LZ}$. Therefore, the probability for a charge to cross form initial state is very low due to it is proportional to the electronic coupling. In this case, ET rate can be described with Marcus theory, originally developed by Rudolph A. Marcus in 1956.^{33,34}

$$k_{na} = \frac{2\pi}{\hbar} \langle |H_{ab}|^2 \rangle_{TS} FC_c \quad (6)$$

$$FC_c = (4\pi\lambda k_b T)^{-1/2} \exp\left(-\frac{\Delta A_{na}^\dagger}{k_b T}\right) \quad (7)$$

where FC_c is the classical Franck-Condon factor and ΔA_{na}^\dagger is the nonadiabatic activation free energy

$$\Delta A_{na}^\dagger = \frac{(\lambda + \Delta A)^2}{4\lambda} \quad (8)$$

However, in the case where $H_{ab} > \lambda/2$, the free energy barrier disappears and the transition state at $\Delta E = 0$ becomes a minimum. In this case, localized states no longer exist and the polaron hopping model becomes invalid.

These limits in terms of ratios H_{ab}/λ are graphically illustrated in Figure 2-2 from ref²⁸. It shows ET free energy curves with increasing values of electronic coupling H_{ab} and constant λ . At $H_{ab} = \lambda/20$ and $\lambda/5$ the ET can be classified as nonadiabatic and as adiabatic, respectively. For $H_{ab} = \lambda/2$ the free energy barrier disappears and the transition state at $\Delta E = 0$ becomes a minimum.

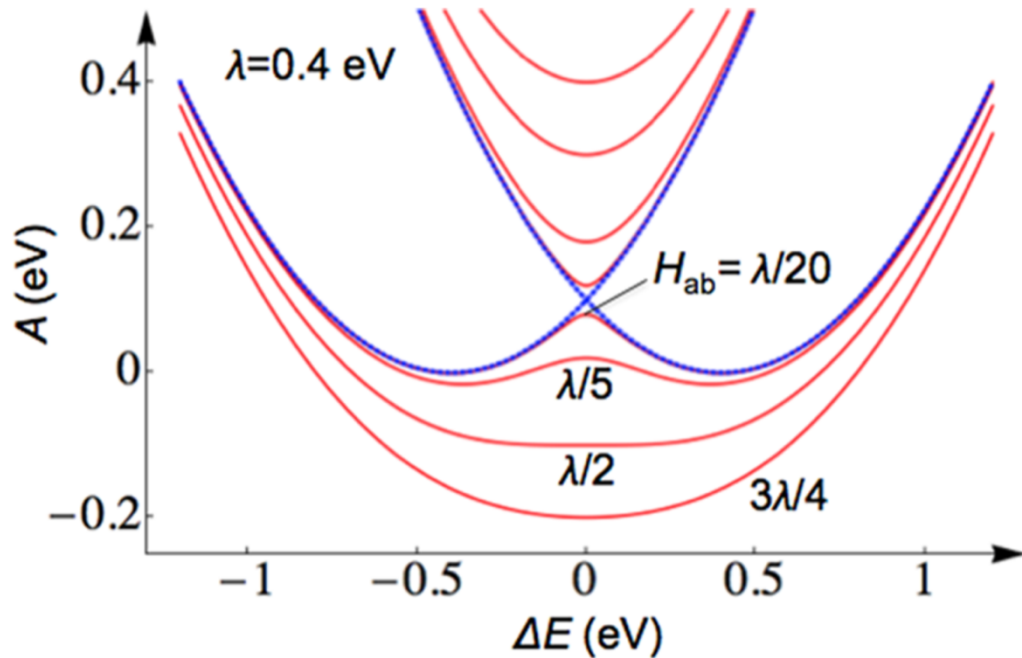


Figure 2-2 ET free energy curves for large ratios H_{ab}/λ . A diabatic and four adiabatic free energy curves are shown in blue and in red, respectively. The later curves have increasing values of electronic coupling H_{ab} at constant $\lambda = 0.4$ eV. ET is nonadiabatic at $H_{ab} = \lambda/20$ and adiabatic at $H_{ab} = \lambda/5$. The free energy barrier disappears at $H_{ab} = \lambda/2$. The plot is from ref²⁸

As we will see in later sections, the OSs materials that I investigate have large electronic coupling, described by Eq 1. Differently, many biological ET reactions mostly occur with typically very small electronic coupling, which can be well described by Marcus formula (nonadiabatic).

2.1.3 ET parameters

Electronic coupling matrix element H_{ab}

Electronic Hamiltonian in the diabatic representation H is given by

$$H = \begin{pmatrix} E_a & H_{ab} \\ H_{ba} & E_b \end{pmatrix} \quad (9)$$

where E_a and E_b are site energies of diabatic electronic states a and b, respectively.

The off-diagonal element of the electronic Hamiltonian (electronic coupling) H_{ab} are defined as the following.

$$H_{ab} = \langle \psi_a | H | \psi_b \rangle \quad (10)$$

where ψ_a and ψ_b are the N-electron wavefunctions of the initial and final diabatic states a and b, respectively, and H is the N-electron Hamiltonian operator for fixed positions of the nuclear coordinates and N is the total number of electrons of the system.

Direct calculation of H_{ab} using high level *ab-initio* methods will be desirable, such as multi-reference configuration interaction (MRCI) or N-electron valence state perturbation theory (NEVPT2).³⁵ However, it is challenging to get the Hamiltonian directly for large systems since the computational demands of quantum chemical calculations increase rapidly with the system size. It would also be more computationally expensive if dynamic disorder is taken into consideration, in which case, the Hamiltonian will be calculated for each snapshot over a trajectory.

Alternatively, H_{ab} can be estimated indirectly by empirical or semi-empirical models. An ultrafast estimation method³⁶ devised in our group has been used in this project. This method applied a well-known linear approximation between H_{ab} and

the overlap S_{ab} of the corresponding diabatic state wavefunctions (SOMO orbitals) for a given donor–acceptor pair

$$H_{ab} \approx C \langle \varphi_a | \varphi_b \rangle = CS_{ab} \quad (11)$$

C is obtained by calibration to explicit electronic structure calculations, $C = 1.819$ eV.

A similar idea is used to describe intra-molecular π -conjugation in organics in Hueckel theory,³⁷ as expressed by the resonance integral beta. The difference here is that the electronic interaction measured by H_{ab} is between two different molecules.

In the computational protocol, firstly, the molecular orbital mediating charge transport (HOMO for hole transport, LUMO for electron transport) obtained from DFT are projected onto a minimum valence shell Slater-type orbital (STO) basis of analytic atomic orbitals with optimized Slater decay coefficients. Secondly, the p_{ij} orbital are further projected onto the p_π orbitals in order to make the projection coefficients invariant to rotations of the same molecule. The calibration of this method has been done and it shows that analytic STO orbital overlap calculation makes the method 6 orders of magnitude faster with respect to reference DFT calculations with little loss of accuracy in the ET calculation in organics.³⁶

Free energy difference ΔA_{ij} and site energies difference ΔE_{ij}

The driving force ΔA_{ij} , appearing in the ET rate expressions, is the free energy difference between the two minima on the diabatic surfaces in Figure 2-1, which

drives electron transfer. They are calculated from the mean energy gaps, $\Delta A_{ij} = \langle \Delta E_{ij} \rangle - \lambda$, where the brackets $\langle \dots \rangle$ denote averaging over the MD trajectory.

The site energy difference ΔE_{ij} is defined as the total potential energy of the system with molecule j charged and all others neutral (E_j) minus the total potential energy of the system with molecule i charged and all others neutral (E_i), both energies evaluated at the same nuclear geometry.

$$\Delta E_{ij}(R^N) = E_j(R^N) - E_i(R^N) \quad (12)$$

where R^N denotes the $3N$ dimensional configuration vector of all N atoms of the system. It indicates that these energies are dependent on the nuclear coordinates. The site energies E_i and E_j cancel each other out in perfect homomolecular crystals by the symmetric equivalence of initial and final states, but do not in disordered systems or crystals with inequivalent sites.

The site energies, E_i and E_j respectively, are diagonal elements of the electronic Hamiltonian, which can be computed with a constrained electronic structure approach³⁸. Nevertheless, for reasons of computational efficiency again, on-the-fly approach is used in this thesis, where Spencer et al. determined site energies purely from classical force field calculations.³⁹

In this approach, classical path method⁴⁰ is a simple approximation to model the charge carrier propagation which has been used in this work. First a molecular

dynamics trajectory of a neutral crystal was pre-computed which ignores the presence of excess electrons. This trajectory was then used to populate the site energies by analyzing its energy for each case of a single excess electron localized on one of the molecules. This provided for each molecular timestep a set of site energy values and then the vertical energy gap ΔE can be simply obtained from the energy difference over the trajectory.

Reorganization energy λ

The reorganization energy (λ) is the free energy required to distort the equilibrium configuration of one diabatic state to the equilibrium configuration of the other diabatic state while remaining on the same diabatic free-energy surface. It consists of inner-sphere (or intramolecular) and outer-sphere (or intermolecular) contributions. The latter contribution takes into account rearrangements of the surrounding medium, such as solvent molecules (e.g. green molecules in Figure 2-1), which is normally the cases for biological reactions. The outer-sphere reorganization energy is usually very small in organic semiconductors due to the small dielectric constant and is neglected in this work.¹⁷

The inner-sphere reorganization energy measures the energy required to rearrange the geometries of the two molecules involved in the charge transfer event. It can be obtained from the standard four-point formula⁴¹

$$\lambda = [E_c(R_n) + E_n(R_c)] - [E_n(R_n) + E_c(R_c)] \quad (13)$$

where $E_{n,c}$ represent the energy of the neutral and the charged states, respectively, and $R_{n,c}$ represent neutral and charged geometries, respectively.

To calculate λ in this work, the neutral and charged geometries of a single molecule in vacuum are optimized in density functional theory (DFT) calculations using B3LYP functional with basis set of 6-311G* associated with dispersion corrections. The two resulting geometries are then fixed and exchange electron sites to compute the total energies separately. This yields the four energies required in Eq 13. In order to save computational cost, classical force fields for the charged state is parameterised for given molecular systems to reproduce the DFT reorganizations energy.

Effective nuclear frequency v_n

The effective frequency v_n in Eq 1 was obtained according to Eq 14

$$v_n = \frac{1}{2\pi\lambda} \frac{2}{\pi} \int_0^\infty d\omega \omega \frac{J(\omega)}{\omega} \quad (14)$$

$$\lambda = \frac{2}{\pi} \int_0^\infty d\omega \frac{J(\omega)}{\omega} \quad (15)$$

$$\frac{J(\omega)}{\omega} = \frac{1}{2k_B T} \int_0^\infty dt \langle \delta\Delta E(0) \delta\Delta E(t) \rangle \cos(\omega t) \quad (16)$$

where $J(\omega)$ is the spectral density function. In Eq 14 each frequency coupling to ET is weighted proportional to its contribution to the reorganization energy, therefore Eq

14 can be considered as a finite temperature, non-harmonic extension of the weighting procedure by Huang and Rhys. The computational details can be found in ref⁴².

2.1.4 Charge carrier mobility

Charge carrier mobility μ characterizes how quickly an electron can move through a semiconductor. It can be obtained by either the Einstein relation for Brownian motion or the numerical derivative of the drift velocity with respect to the external field. These two definitions of charge mobility are discussed below.

Without any external potential, a carrier purely diffuses. The charge mobility μ can be generally derived from the Einstein-Smoluchowski equation with the diffusion coefficient D.

$$\mu_{ij} = qD_{ij} / (k_B T) \quad (17)$$

where q is the electron charge, k_B is the Boltzmann constant, and T is the temperature.

The diffusion coefficient D in the three dimensional system can be obtained from the mean square displacements (MSD):

$$2D_{ij}t = \langle (R_i(t) - R_i(0))(R_j(t) - R_j(0)) \rangle \quad (18)$$

where t is the time, $R_i(t)$, $i = x, y, z$, is the successive Cartesian coordinates for the centre of mass of the molecule carrying the excess charge that were monitored along a kinetic Monte Carlo trajectory (see section 2.1.5).

Thus, the mobility tensor can be computed as

$$\mu_{ij} = \frac{q\text{cov}(R_{ij})}{2t k_B T} \quad (19)$$

Alternately, a carrier will drift in the material due to an external electric field. The mobility can also be defined as the the drift velocity response of a charge carrier v to the external electric field E .^{43,44} Since this response is not generally linear, derivative of each velocity component, $v_i, i = x, y, z (t)$, is taken with respect to the external electric field E in direction $j, E_j, j = x, y, z$

$$\mu_{ij} = \frac{\partial v_i}{\partial E_j} \quad (20)$$

It is worth noticing that μ is a 3*3 mobility tensor, since v and E are three-dimensional vectors.

2.1.5 Kinetic Monte Carlo simulation of mobility

In order to derive macroscopic mobilities from microscopic charge hopping steps, electron diffusion within the organic molecular crystals was modeled as a random walk using a kinetic Monte Carlo (KMC) code developed recently in our group, in which the charge carrier hops were assumed to be infrequent events and the system has time to thermalise between each event. This state-to-state dynamics in this type of

system corresponds to a Markovian walk,⁴⁵ in which the transition probabilities for a previous state have no effect on the current state.

In the KMC model, excess electrons introduced in the lattice diffuse via first nearest-neighbor hops. The carrier can only occupy a single molecule at any one time. Thus, the mobility was studied by tracing the successive positions of the centre of mass of the molecule at a certain temperature.

The electron is propagated using the Borz-Kalos-Leibowitz (BKL) algorithm which describes a no-rejection ‘residence-time’ procedure with Monte Carlo.⁴⁶ This algorithm requires 2 random numbers per hop: one determines the hopping direction and the other determines the residence time at the current site.

At each KMC step, a list of all possible hops is established, the rate of each hop is determined from Eq 1, and a hop is selected with a probability proportional to its rate,

$$\sum_{j=1}^{i-1} k_j < r_1 k_{tot} \leq \sum_{j=1}^i k_j \quad (21)$$

where k_j is the rate of the j th hop, r_1 is a random number in (0,1). k_{tot} is the sum of all the rates,

$$k_{tot} = \sum_j k_j \quad (22)$$

Eq 22 shows the procedure for picking the reaction pathway to the next state.

A residence time Δt is given by

$$\Delta t = -\frac{\ln r_2}{k_{tot}} \quad (23)$$

where r_2 is a second random number in $(0,1]$. This time drawn from an exponential distribution,

$$p_j(t) = k_j \exp(-k_j t) \quad (24)$$

Similar KMC approaches have been used to model charge transport in organic disordered materials,⁴⁷⁻⁴⁹ doped semiconductors,⁵⁰ in hematite⁵¹ and to model vacancy mobility in defected metals.⁵²

2.2 Band transport model

The band transport, in the opposite of charge hopping regime where the charge carrier electron is assumed to be delocalized. It only applies at relatively low temperatures where electron-phonon coupling is small so that the mean free path of the charge carrier is significantly longer than the lattice spacing. There has been vast of literatures on the topic of band transport and semiconductor research over the years on inorganics^{53 54} and organic ultrapure crystal^{55,56}.

The band theory is based on Bloch's theorem. The transport properties of the periodic system are determined by its band structure represented as a reciprocal space function of electronic eigenenergies, i.e., the dispersion relation.

2.2.1 Comparison between the bandstructure of inorganic and organic semiconductor

Inorganic and organic are two cases in terms of energy-dispersion relationships. In inorganic semiconductors, electrons move freely, leading to a valence band and a conduction band with pronounced curvature, and a low effective mass (Figure 2-3a). Electrons and holes move with high mobility. By contrast, in organics, molecular orbitals are derived from delocalized $2p \pi$ electrons the gap between HOMO and LUMO, like the gap between the valence and conduction bands (Figure 2-3b). However, the overlap of the orbitals of adjacent molecules is so small that the bands in the organic material are flat, with low dispersion and a large effective mass. Therefore, in the band model picture the charge mobility in OS is smaller than that for inorganic semiconductors.

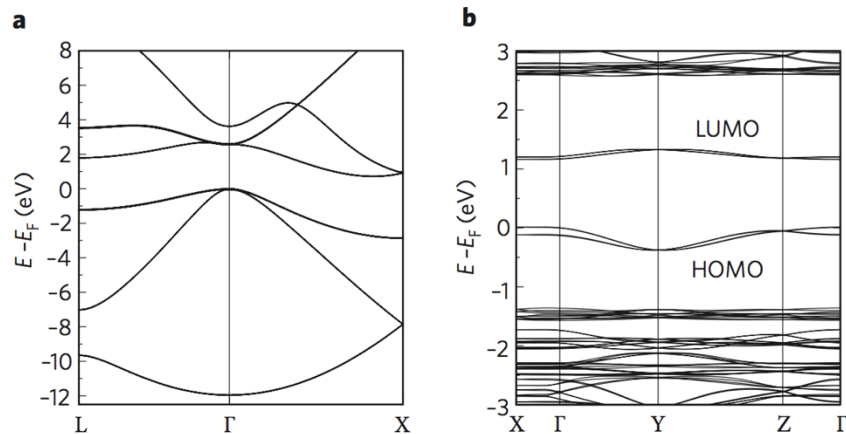


Figure 2-3 Comparison between the energy-dispersion relationships of typical inorganic and organic (calculated by DFT). **(a)** The bandstructure of Si. **(b)** The bandstructure of a rubrene single crystal. From ref⁵⁷.

2.2.2 Band transport mobility

Band transport regime has two basic assumptions: (1) Charge carriers occupy only the lowest subbands, i.e. valence band maximum (VBM) and the conduction band minimum (CBM) for holes and electrons; (2) According to deformation potential theory, electronic energy dispersion is shifted by the crystal deformation due to acoustic phonon scattering carriers.⁵⁸

The carrier mobility μ is without any dependence on the applied electric field in the band theory. It is determined by two parameters: the effective mass along the transport direction m_e and on the relaxation time $\bar{\tau}$ (Eq 25). The former is defined as the curvature of the respective band dispersion relation, and the latter is the average time between (elastic) scattering events that reset the carrier distribution in a band.

$$\mu = q \frac{\bar{\tau}}{m_e} \quad (25)$$

Effective mass m_e

The effective mass m_e can be simply obtained from parabolic fit of the VBM and the CBM for holes and electrons, respectively, $\varepsilon(k)$ with respect to \mathbf{k} vector. Note that Eq 26 is a harmonic approximation valid only near the VBM or CBM.

$$m_e = \hbar^2 \left[\frac{\partial^2 \varepsilon(k)}{\partial k^2} \right]^{-1} \quad (26)$$

where \hbar is reduced Planck's constant.

Relaxation time $\bar{\tau}$

The relaxation time $\bar{\tau}$ is not as straightforward to calculate. It can be determined within the relaxation-time approximation. In organic crystals, charge transport is often restricted to a lower dimensionality. The one-dimensional (1D) expression of relaxation time⁵⁹ is of the form

$$\bar{\tau} = \frac{\hbar^2 C}{E_l^2 \sqrt{2\pi|m_e|k_B T}} \quad (27)$$

where \hbar is reduced Planck's constant, k_B is Boltzmann's constant, temperature T , E_l is deformation potential and C is elastic constant of the crystal.

The elastic constant C , is a measure for the total energetic response to lattice strain, it is determined by the length a of the respective unit cell vector.

$$C = a_0 \frac{\partial^2 E_{tot}}{\partial a^2} |_{a=a_0} \quad (28)$$

The deformation potential constant E_l describes the single electron response to a lattice deformation. It can be calculated from the response of the eigenenergy of the band in VBM or CBM at the extremal k-point (k_e) to a lattice deformation along the transport direction.

$$E_l = a_0 \frac{\partial \varepsilon(k)}{\partial \delta a} |_{a=a_0} \quad (29)$$

As you will see later, hole transfer mobility of 1D-chain anthracene has been computed from electronic band structure. Effective mass along the transport direction m_e is obtained from parabolic fit of the valence band minimum. The elastic constant of the crystal C is obtained from parabolic fit of the total energy change with the lattice constant. The deformation potential E_l is obtained from linear fitting of valence band minimum shift with the dilatation / contraction of the cell. The latter two constants yield the relaxation time $\bar{\tau}$.

2.3 Beyond hopping and band transport

In the previous section, two regimes of charge transport and their limitations have been discussed. Nevertheless, there are cases beyond these two mechanisms, where charge carrier is neither localized at a site, nor fully delocalized in a carrier band.

Recently, advanced simulation methodologies including mixed quantum-classical non-adiabatic molecular dynamics (MQC-NAMD) have been developed in first attempts to address this challenging problem^{20,39,60-63} (see Ref.³⁹ for a discussion of some of these works). Here the charge carrier is explicitly propagated in the time-dependent potential created by the nuclei avoiding any *a priori* assumptions of the CT mechanism. For instance, Elstner and co-workers have simulated charge mobilities in 1D chains of organic molecules using Ehrenfest MD with electronic Hamiltonians at the level of self-consistent charge density functional tight binding.⁶² Our group has developed a similar approach denoted fragment orbital-based surface hopping which

has been successfully applied to 1D chains and dimers of simple molecules.³⁹ Unfortunately, nonadiabatic MD simulations are computationally expensive even when combined with semiempirical electronic Hamiltonians, and applications to extended 3D materials investigated here are still impractical. In addition, MQC-NAMD schemes are not straightforward to apply in practice. Several remedies have been suggested to cure a number of inherent problems such as electronic overcoherence⁶⁴⁻⁶⁹, trivial surface crossings^{61,70,71} and detailed balance⁷²⁻⁷⁵ but their effect on charge mobility calculations in realistic molecular systems is still under investigation.

3 Organic Single Crystals

In the previous chapter, ET theory and computation approaches have been introduced.

In this chapter, the methodology is applied on single crystals. The computational tool based on polaron hopping model is presented combining molecular dynamics with quantum chemical calculations to compute the key parameters that determine the charge transport. Kinetic Monte Carlo approach is used to compute hole mobilities, and temperature dependence of mobility are presented and compared with experimental values. Also, the ET parameters and validation of hopping model are discussed.

Table 3-1 Lattice parameters of benzene, rubrene, pentacene, C₆₀ and anthracene crystals

	benzene ⁷⁶	rubrene ⁷⁷	pentacene ⁷⁸	C ₆₀ ⁷⁹	Anthracene ⁸⁰
unit cell dimensions	a(Å)	7.4	7.2	6.3	14.2
	b(Å)	9.4	14.4	7.8	14.2
	c(Å)	6.8	26.9	14.5	14.2
	α(deg)	90.0	90.0	76.7	90.0
	β(deg)	90.0	90.0	87.5	90.0
	γ(deg)	90.0	90.0	84.6	90.0
lattice system	orthorhombic	orthorhombic	triclinic	cubic (FCC)	monoclinic
room temperature density (g/cm⁻³)	0.88	1.2	1.3	1.65	1.25
molecules per unit cell	4	4	2	4	2
molecules per supercell (3*3*3 unit cell)	108	108	54	108	54

Material systems cover benzene, rubrene, pentacene, fullerene and anthracene crystals. Benzene is simple and small and is a good candidate for testing the model;

rubrene, pentacene and fullerene are three popular and application-relevant OSs, which are recently reported high-performance materials;^{7,81,82} and anthracene is selected to compare hopping and band transport mobilities with experiments.

A careful characterization of electronic couplings, charge trapping energies and site energies, as well as their thermal fluctuations, is required as a basis for the investigation of the CT mechanism in OSs. Here I present calculations of these quantities for rubrene, pentacene and C₆₀. The molecules forming these three crystals exhibit an increasing degree of thermal motion. While rubrene molecules are “locked” to their lattice sites due to their bulky substituents, pentacene molecules fluctuate more freely but are still constrained by neighbouring molecules, whereas C₆₀ buckyballs show unhindered rotational diffusion above 255 K⁸³.

3.1 Material systems

3.1.1 Benzene crystal

Benzene is liquid at room temperature. Below the transition temperature of 278.68K, the crystal lattice becomes face-centred cubic (FCC) and the benzene crystal structure has orthorhombic symmetry. There are four centro-symmetrical molecules in the unit cell, within two molecules in pairs roughly perpendicular to each other. The experimental lattice parameters are shown in Table 3-1 and Figure 3-1 shows a molecular dynamics snapshot of a crystalline benzene supercell at 150K, in which a herringbone structure can be seen.

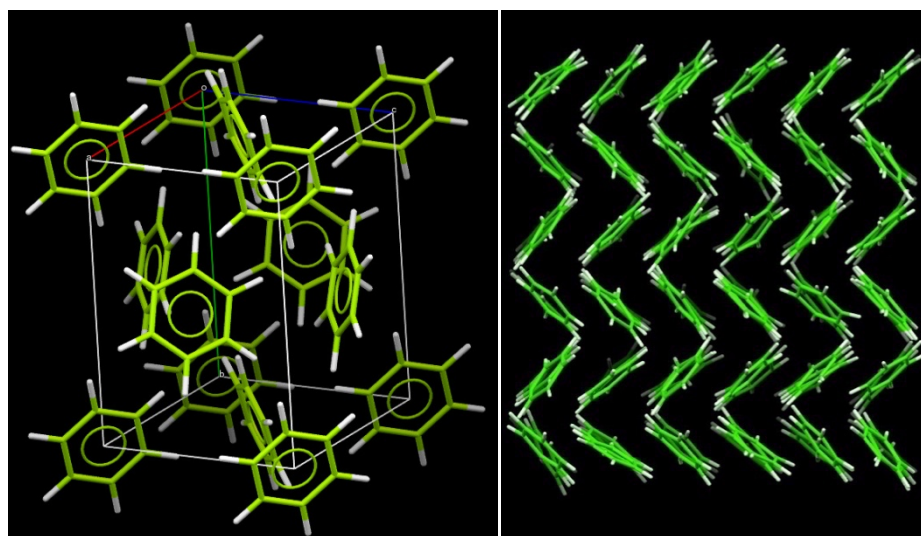


Figure 3-1 The unit cell of crystalline benzene (left) and a snapshot of molecular dynamics at 150K (right).

There are reasons that this benzene model has been selected to test the computational model even though benzene is not used in a device due to its low melting point and there is little experimental data to compare for its electron transfer behavior. Because the most organic semiconducting materials typically have benzene rings as the basic unit; benzene as the simplest and the smallest π -conjugated material is computationally cheap to test the simulation protocol in an early stage of the work, which will be implemented further to other material systems with larger molecular size and higher complexity.

3.1.2 Rubrene crystal

Rubrene is a derivative of tetracene, with four additional phenyl side groups that lie planes that are perpendicular to the plane of the tetracene backbone. At room

temperature it is FCC, similar to the packing of crystalline benzene, with 4 molecules per unit cell.

Tetracene backbone in rubrene and pentacene (showed in the next section) have high planarity and rigidity, which facilitates strong intermolecular ordering, and their π -conjugation over the whole molecule enables large intermolecular orbital overlap.

While rubrene has less orientational disorder than pentacene because the former's side groups lock the molecule tightly in the crystal.

The modeling challenge of the rubrene crystal is that the four phenyl side groups increase the complexity of the classical force field by introducing a distinct C-C-C-C dihedral angle from the rest within backbone.

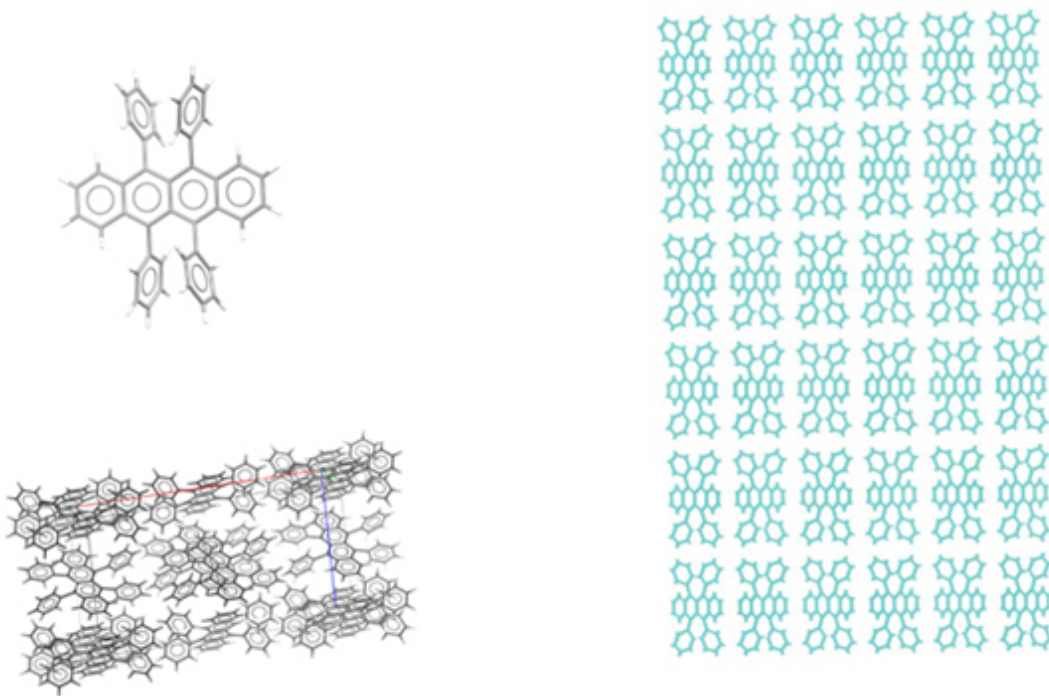


Figure 3-2 A schematic diagram of a rubrene molecule (left top), the unit cell of crystalline rubrene (left bottom) and a snapshot of molecular dynamics at 283K (right).

3.1.3 Pentacene crystal

Pentacene ($C_{22}H_{14}$) is a polycyclic aromatic hydrocarbon consisting of five linearly-fused benzene rings. At room temperature, the crystal structure of pentacene has triclinic packing with 2 molecules per unit cell. Figure 3-3 is a snapshot of the crystal structure at 283K.

Pentacene has a significantly lower reorganization energy than shorter oligoacenes molecules, such as benzene. Its triclinic crystal structure leads to a modeling challenge of molecular dynamic simulation and ET properties are expected to be anisotropic due to the long molecular axis.

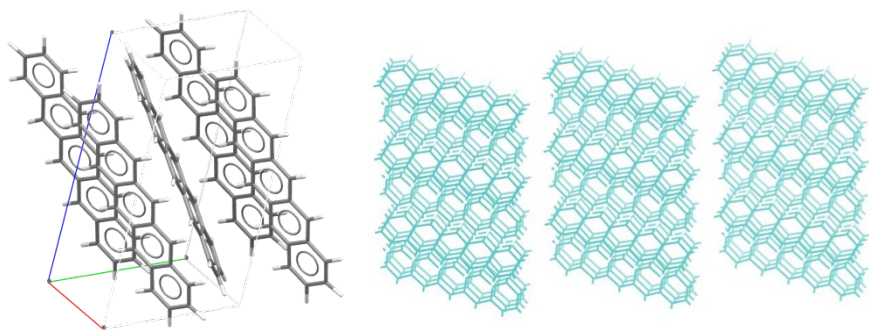


Figure 3-3 The unit cell of crystalline pentacene (left) and a snapshot of molecular dynamics at 283K (right).

3.1.4 Buckminsterfullerene C₆₀ crystal

Buckminsterfullerene (C₆₀) has a cage-like fused-ring structure, made of twenty hexagons and twelve pentagons. C₆₀ molecules adopt the face-centered cubic (fcc) motif, thus there are 4 molecules in a unit cell. They start to rotate freely at about 255K.⁸³ The covalent bonds between carbon atoms make buckyballs very strong so that buckyballs are used to strengthen materials. Buckyballs also have the interesting electrical property of being very good electron acceptors, and C₆₀ crystal is an n-type semiconductor with a low activation energy of 0.1–0.3 eV.

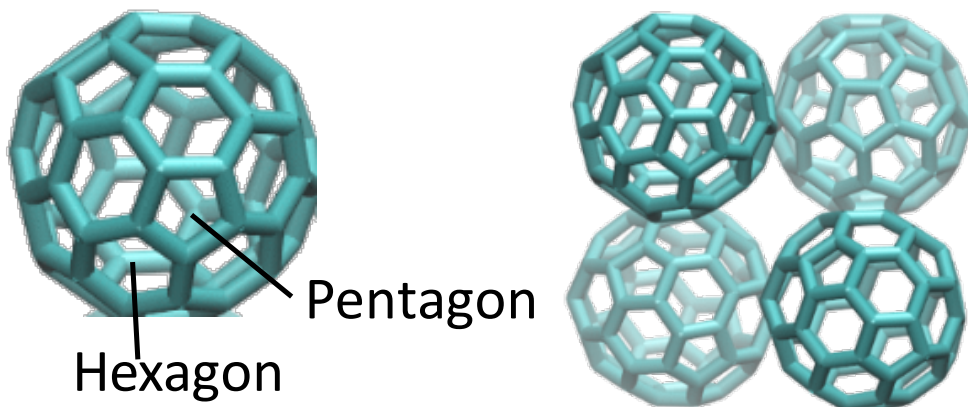


Figure 3-4 A schematic diagram of a C_{60} molecule (left) and the unit cell of crystalline C_{60} (right). It is noted that each molecule reorients randomly at room temperature and there are no intermolecular rotational correlations.⁸⁴

3.1.5 Anthracene crystal

Anthracene ($C_{14}H_{10}$) is a polycyclic aromatic hydrocarbon consisting of three linearly-fused benzene rings. At room temperature, the crystal structure has 2 molecules per unit cell, like the case in pentacene, but differently, its group space is monoclinic with higher symmetry. It has a significantly higher reorganization energy compared with pentacene. Anthracene is a wide-bandgap organic semiconductor and it can operate at much higher temperatures, on the order of $300\text{ }^{\circ}\text{C}$, this makes them a suitable type of material for photovoltaic cells.

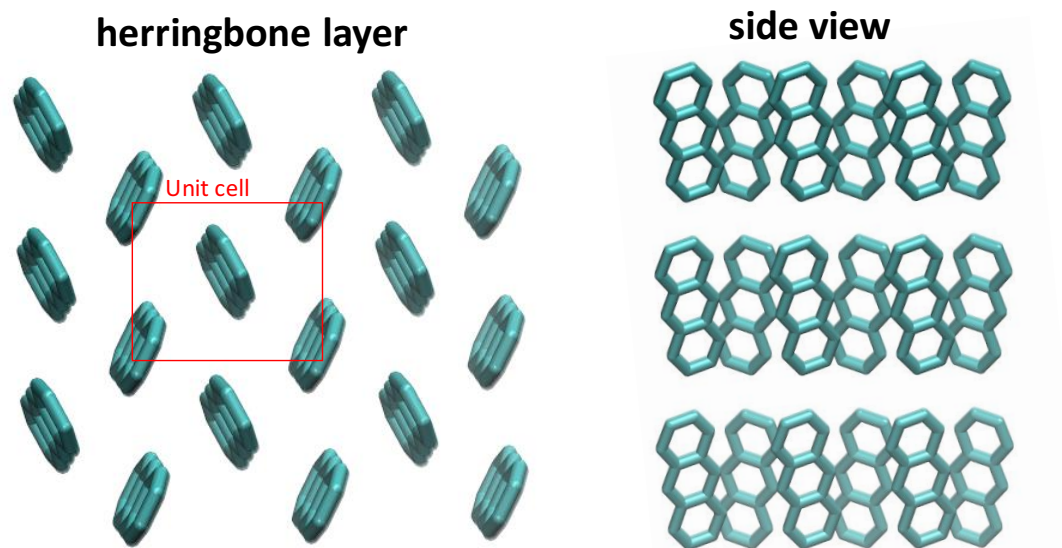


Figure 3-5 The snapshots of anthracene crystal within herringbone layer (left) and from side view (right).

3.2 Computational details

3.2.1 Workflow of polaron hopping simulation in molecular organics

- 1) Download crystal structure from the Cambridge Crystallographic Data Centre (CCDC).
- 2) Build the supercell with periodic boundary condition (PBC) and generate input files (configuration, coordinate, and topology files) to molecular dynamics package. Molecular dynamics simulations are carried out at a given temperature.

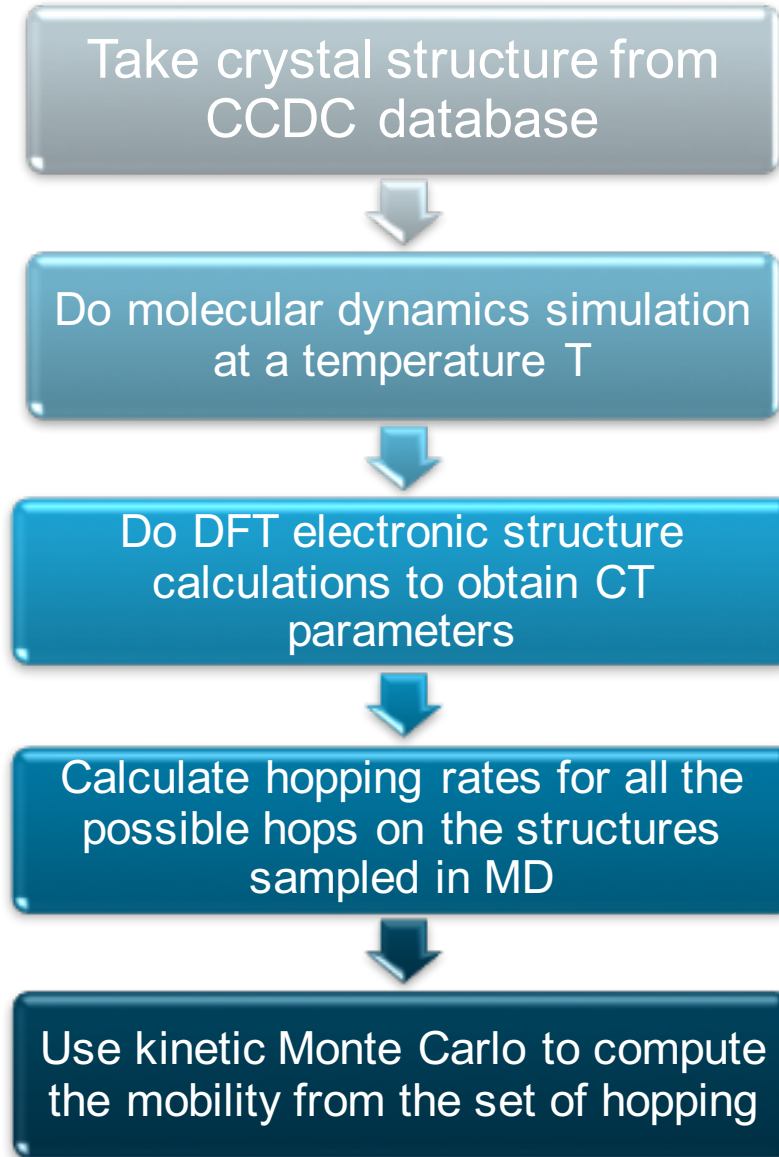


Figure 3-6 Workflow of polaron hopping simulation in OSs

- 3) Do DFT electronic structure calculations to obtain ET parameters. To guarantee low computational cost and high accuracy of our charge hopping model, the diagonal elements of the electronic Hamiltonian were computed by molecular dynamics and the off-diagonal elements of electronic Hamiltonian were obtained by the ultrafast analytic overlap method (AOM). Parametrize the classical force field (FF) to reproduce DFT reorganization energy (λ).

- 4) Calculate hopping rates for all the possible hops on the structures sampled in MD trajectories.
- 5) Compute mobility tensor from the set of hopping rates using KMC followed by diagonalization. The diffusion coefficient D in the three-dimensional system can be obtained from the mean square displacements.

3.2.2 Force field parameterization

Calculations were carried out using a combination of quantum chemical calculations and molecular dynamics (MD) simulation. Electronic structure calculations were carried out with the Gaussian programme package⁸⁵ or CPMD⁸⁶ and force-field calculations with the Amber programme package⁸⁷. What has been done here was parameterizing the classical force field (FF) to reproduce reorganization energy (λ) for charge transfer between the corresponding dimers at infinite separation using density functional theory (DFT) calculations as a reference.

The quantum chemical calculations were undertaken with DFT method. A hybrid functional in the form of B3LYP was used with a 6-311G* basis set. This functional and basis set were selected by considering a balance between accuracy and efficiency as well as keeping the same with our database set.³⁶ The * denotes the addition of single first polarization functions to heavy atoms, this ensures that the contracted Gaussians (CGs) beyond the expected angular momentum for a ground state description is included. For example, d-functions are added for carbon atoms in a

polarized basis set. Atomic charges of the molecules were computed by fitting the restrained electrostatic potential (RESP) rather than the default setting of Mulliken population analysis, and they are used as atomic point charges in the force field description.

Even though Mulliken population analysis is the simplest way to determine quantum chemical charges, it poorly reproduce electrostatic moments without taking any account of differences in atom type, coefficients, electronegativity. This method simply distributes the charge according to the atomic orbital occupation, and the overlap population between pairs of atoms is evenly divided between the two atoms. An alternative way is to fit electrostatic potentials (ESP), though ESP charges are known to overestimate the strengths of hydrogen bonded interactions. Thus, RESP-charges are used by adding a restraint function during the fitting of the partial charges to the electrostatic potentials so that magnitudes of the charges may be attenuated.

Table 3-2 Summary of reorganization energies from DFT and force field

molecule	λ from DFT (B3LYP/6-311G*) (meV)	λ from optimized force field (meV)
benzene	300.0	300.0
rubrene	152.7	151.0
pentacene	97.9	96.7
C ₆₀	105.4	104.5
anthracene	140.0	140.0

In terms of force field parameterization, an Amber generalized force field (GAFF)⁸⁸ were used to generate the neutral charge state of the molecules and all the force field parameters for the charged molecule are the same as for the neutral molecule except

for the position of the minimum of the C=C harmonic bond potential, which was adjusted in order to match the reorganization energy at DFT level. λ was obtained from the standard four-point formula Eq 13. The charges are from the DFT calculations above.

The bond lengths and atomic point charges used are summarized in Figure S1 and Figure S2 for each molecule and charge state, and the resultant reorganization energies at DFT and force field level are summarized in Table 3-2.

The details of how the parameterization was done is in the protocol included in Support information.

3.2.3 Molecular dynamics simulation

Crystal structures were taken from the Cambridge Crystallographic Data Centre (CCDC). Each system was modelled by supercells containing 108 benzene,⁸⁹ 54 pentacene,⁹⁰ 108 rubrene,⁹¹ 108 C₆₀,⁷⁹ and 54 anthracene molecules⁸⁰, respectively, by replicating the respective crystal unit cells three times along each crystallographic axes. MD simulations were carried out with the NAMD package.⁹²

MD simulations of the crystals were carried out for the neutral system at five different temperatures (100, 200, 300, 400 or 500 K) and at a pressure of 1 bar applying periodic boundary conditions. After equilibration (less than 50 ps), a trajectory of length 1 ns was run in the isothermalisobaric NPT ensemble using a Langevin thermostat. This

trajectory was used for the calculation of ET parameters. The structure was stable during the finite temperature MD runs with RMSDs between 0.31–0.95 Å with respect to experimental crystal structures. The relative error with respect to the experimental density (where known) was between 1.4-2.7%.

The time step was set to 1 fs amounting to approximately 10 integration timesteps per oscillation for the fastest vibration (10^{-14} s for O-H stretch vibration). By monitoring the volume of the system over time, the lattice constant equilibrated after approximately 50 ps.

3.2.4 ET parameters

One thousand snapshots were taken in equidistant intervals of 1 ps for calculation of ET parameters (electronic coupling matrix elements H_{ij} , site energy difference ΔE_{ij} and free energy difference ΔA_{ij}) and charge hopping rates k_{ij} between adjacent molecules (typically 300-1300 pairs per snapshot). Electronic-coupling matrix elements (H_{ij}) were calculated using the ultrafast Analytical Overlap Method (AOM).³⁶

This method is based on a linear approximation $H_{ij} = CS_{ij}$, where S_{ij} is the overlap of the SOMO orbitals of charged donor and acceptor, and C is obtained by calibration to explicit electronic structure calculations, $C = 1.819$ eV.³⁶ AOM gives couplings with small mean errors of about a factor of 1.9 over 4 orders of magnitude relative to DFT calculations, but saves 6 orders of magnitude of computational cost.³⁶

The site energy difference ΔE_{ij} is computed as the total potential energy of the system with molecule j charged and all others neutral minus the total potential energy of the system with molecule i charged and all others neutral, both energies evaluated at the same nuclear geometry. The force field parameters for the neutral and charged molecules are used as explained above.

Reorganization energy is obtained by four-point scheme (Eq 13) and assumed to be the same for each pair and equal to the intramolecular (or “inner-sphere”) contribution, $\lambda_{ij} = \lambda$ summarized in Table 3-2. The intermolecular (or “outer-sphere”) contribution is small and neglected in this work.

Free energy differences ΔA_{ij} for charge hopping were calculated from the mean energy gaps, $\Delta A_{ij} = <\Delta E_{ij}> - \lambda$, where the brackets $<\dots>$ denote averaging over the MD trajectory. I found that ΔA_{ij} is vanishingly small for any hopping direction because the molecules i, j of the simulated crystals are chemically identical and interact with similar environments. Thus, I set this parameter equal to zero.

3.2.5 ET rates

The ET rates k_{ij} are obtained from the semiclassical expression, Eq 1. In the Eq 14, the spectral density function $J(\omega)$ is obtained from MD simulation for the neutral crystalline systems at 300 K. Trajectories of length 100 ps are run and the site energy difference for a selected donor acceptor pair, ΔE used for the calculation of the site energy time correlation function $\langle \delta\Delta E(0)\delta\Delta E(t) \rangle$. This gives values $v_n/c = 1539$

cm^{-1} , 1399 cm^{-1} and 1624 cm^{-1} for pentacene, rubrene, and C_{60} , respectively (c the speed of light). The difference in effective frequency for the different donor-acceptor pairs within the same crystal can be neglected.

3.2.6 Charge mobility

The microscopic rate constants for charge hopping were used to obtain macroscopic charge mobilities using an in-house developed kinetic Monte Carlo simulation programme that implements the Borz-Kalos-Leibowitz (BKL) algorithm⁴⁶. The diffusion of only a single excess charge in the crystal is considered, hence the simulations correspond to the limit of low charge carrier concentration. For each of the 1000 structures sampled along the 1 ns MD trajectory KMC simulation of charge carrier diffusion is carried out (at fixed nuclear positions). The successive Cartesian coordinates $R_i(t)$, $i = x, y, z$, of the centre of mass of the molecule carrying the excess charge were monitored along a KMC trajectory and the diffusion tensor D_{ij} calculated from the mean square displacements (Eqs 18-19), $2D_{ij}t = \langle (R_i(t) - R_i(0))(R_j(t) - R_j(0)) \rangle$ where the bracket indicates averaging over about 1000 KMC trajectories per structure. The mobility tensor was obtained using the Einstein relation (Eq 17), $\mu_{ij} = qD_{ij} / (k_B T)$, followed by diagonalisation. The eigenvalues of the mobility tensor thus obtained were averaged over all MD configurations. To validate of the model, the computed mobilities obtained from the hopping model need to be compared to experimental mobilities.

3.3 Validation of simulation protocol: benzene

3.3.1 Validation of force field for MD

Before results on charge transport being presented, I would like to assess here the performance of the classical force field in describing structural and dynamic properties.

Benzene is taken for validation. The computational densities of benzene are compared with experimental values ranging from 0 K to melting point, see Figure 3-7 and Table 3-3 It shows that MD simulations predict slightly lower densities of benzene crystal by 2-10%, and provide a lower melting point by ~60K. The experimental densities are from different literatures and the characterize methods and samples may also vary. At 150K, the MD density has the best agreement with experiential data.

Table 3-3 Experimental and computational comparison of density vs. temperature

temperature(K)	experimental density (g*cm ⁻³)	MD density (g*cm ⁻³)
4	1.23 ⁹³	1.123
15	1.207 ⁹⁴	1.117
138	1.094 ⁸⁹	1.057
150	1.05 ⁷⁶	1.038
218	1.055 ⁸⁹	liquid
270	1.024	
279	liquid	

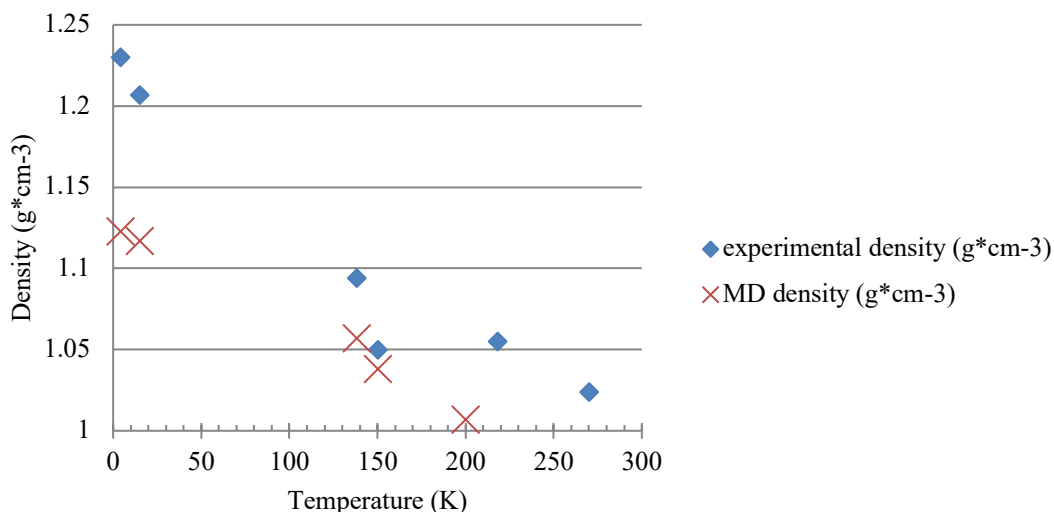


Figure 3-7 Experimental and computational comparison of density vs. temperature.

3.3.2 Electronic couplings in benzene

Only the electronic couplings between adjacent dimers have been taken into consideration since these have been reported to be sufficient to get quantitative results.^{95,96} Thus, a distance cut-off is implemented to guarantee the speed of calculations. In the case of the benzene model, the dimers in first and second major peaks in the radial distribution function (Figure 3-8) are taken in ET simulations.

The values of the couplings span a large range of 5 orders of magnitude from $\sim 10^{-3}$ to 10^2 meV (see Table 3-4). The distinct spacing and orientational dimers, which are distinguished along various crystal directions using the crystallographic parameters presented in Figure 3-9, in which we observe the orientations and how the orbitals overlap between a molecule and its neighbours in the unit cell.

The largest electronic couplings, 58.26 meV, corresponds to the (0.5, 0, 0.5) directions in benzene (the first donor-acceptor configuration in Figure 3-9). The charge transfer rate is approximately proportional to the square of electronic couplings from Eq 5; the largest rates in benzene will be expected along the directions of this type of dimers. This dimer with closest separation will be under investigation specifically further. I note that in structures No. 3 the pairs have a longer average distance (5.90 Å) but stronger coupling than No.2 pairs (5.81 Å), probably because the former dimer has a higher orbital overlap than the latter.

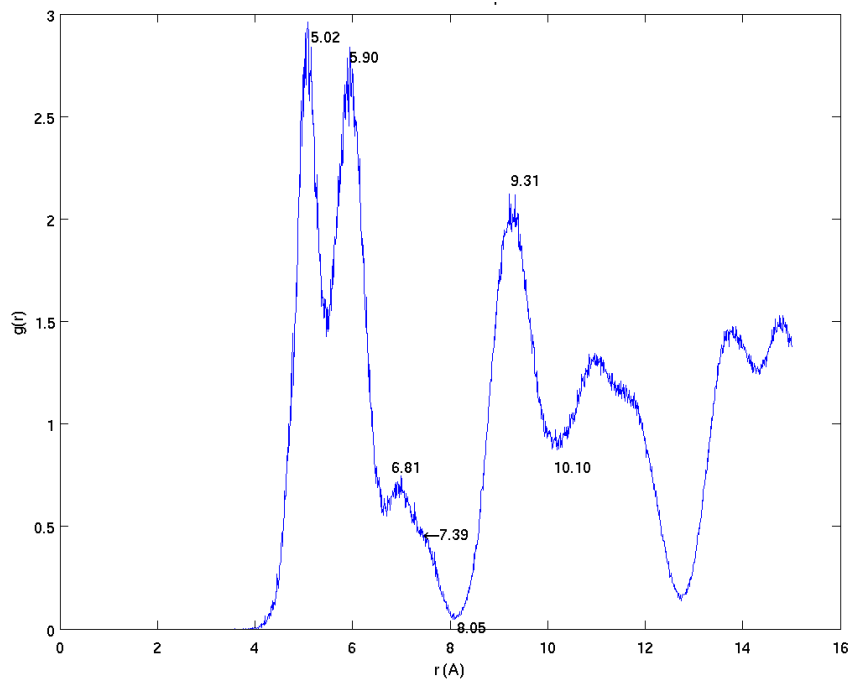


Figure 3-8 Radial distribution function $\bar{g}(r)$ of center of mass of benzene molecule as obtained from 1 ns MD trajectory at 138 K.

Table 3-4 Summary of rates constant and mean values of electric couplings for inter-molecular hole transfer in benzene.

dimers	k_{ij} , Hz	$ H_{ab} $, meV	a	b	c	Distance of center of mass, Å
1	4.29E+12	58.26	0.5	0	0.5	5.02
2	2.01E+11	21.10	0	0.5	0.5	5.81
3	2.70E+11	23.60	0.5	0.5	0	5.90
4	6.60E+10	14.34	0	0	1	6.81
5	1.00E+10	6.79	1	0	0	7.39
6	3.80E+06	0.06	0	1	0	9.42
7	1.00E+08	0.33	0.5	0.5	1	9.07
8	6.52E+07	0.25	1	0.5	0.5	9.40

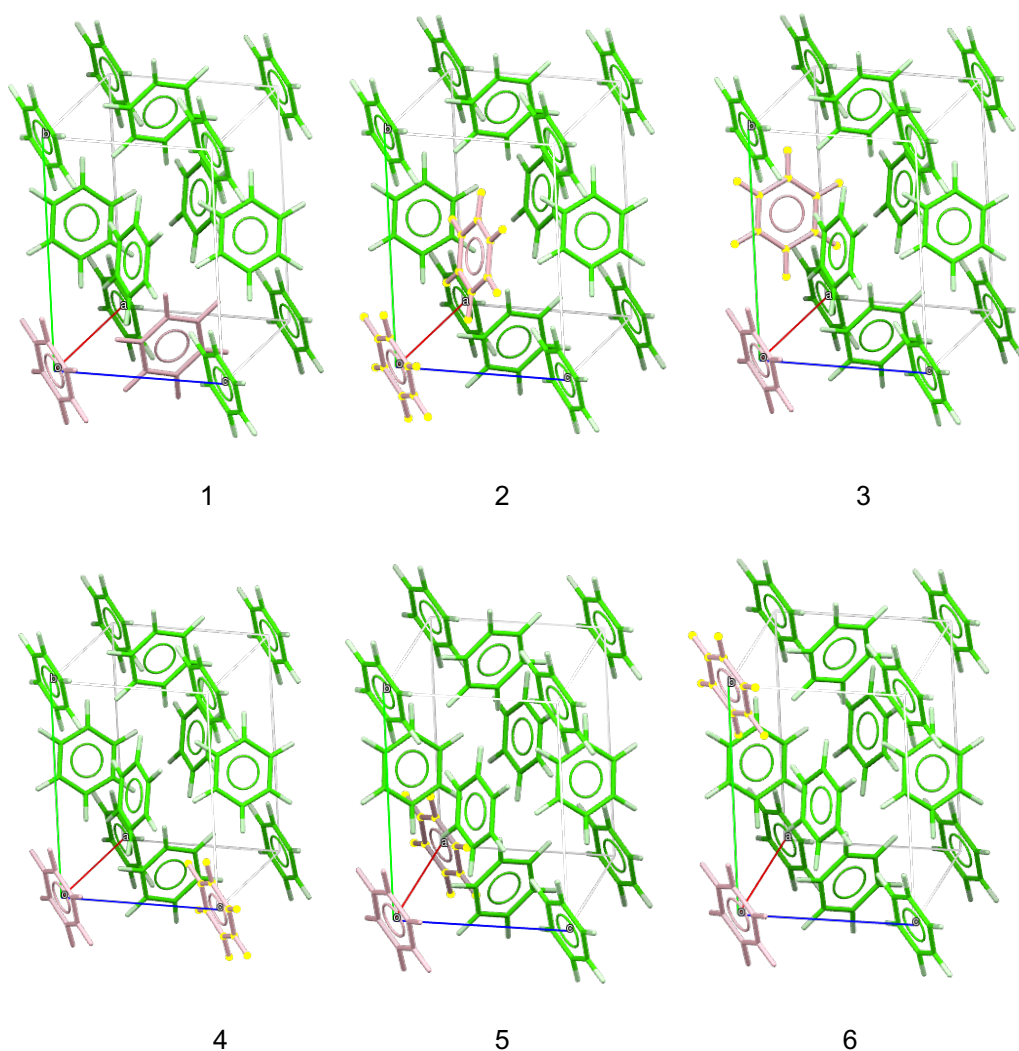


Figure 3-9 Spacing and orientation for selected donor-acceptor configurations (in pink) in a benzene unit cell. The index increases with the distance of center of mass for dimers and keep consistency with that in Table 3-4. Lattice parameters: a= 7.4 Å (red), b=9.4 Å (green), c=6.8 Å (blue).

3.3.3 Site energy in benzene

Thermal distribution of site energy ΔE_{ij}

The vertical site energy gap ΔE_{ij} was calculated between all pairs of molecules in the crystal and the distributions were found to fit a Gaussian distribution centered on 0 meV with a standard deviation of 88.58 meV.

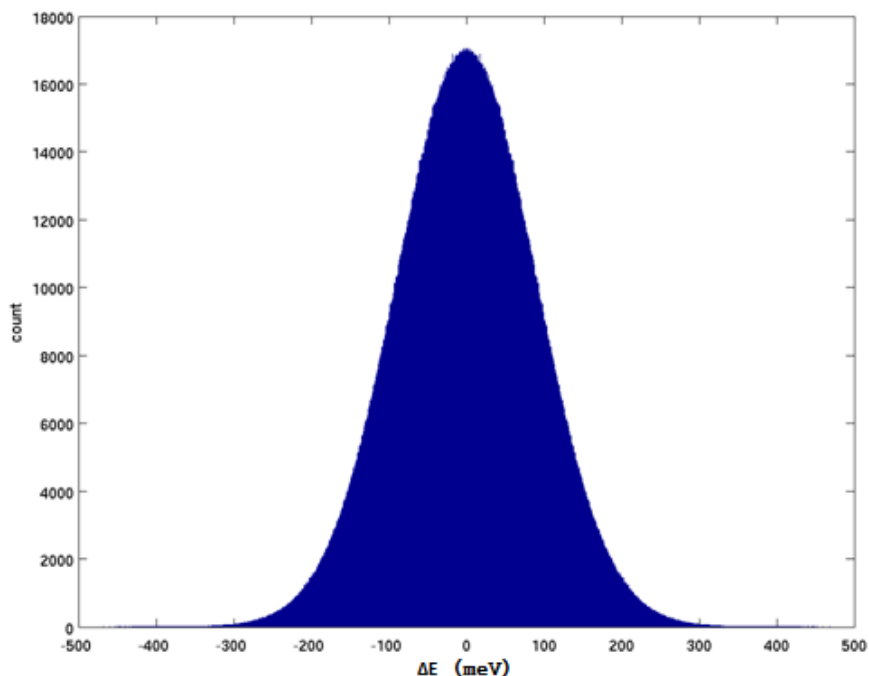


Figure 3-10 The distribution of site energy differences over the benzene molecular trajectory at 150K.

Cosine transform of ΔE_{ij} in benzene

Here we wish to interpret the site energy fluctuations in terms of the vibrational modes of the molecules. We do so by analysing the spectral density function $J(\omega)$ (see Eq 16), from molecular simulation as the cosine transform of the autocorrelation function $c(t)$ of the vertical energy gap.

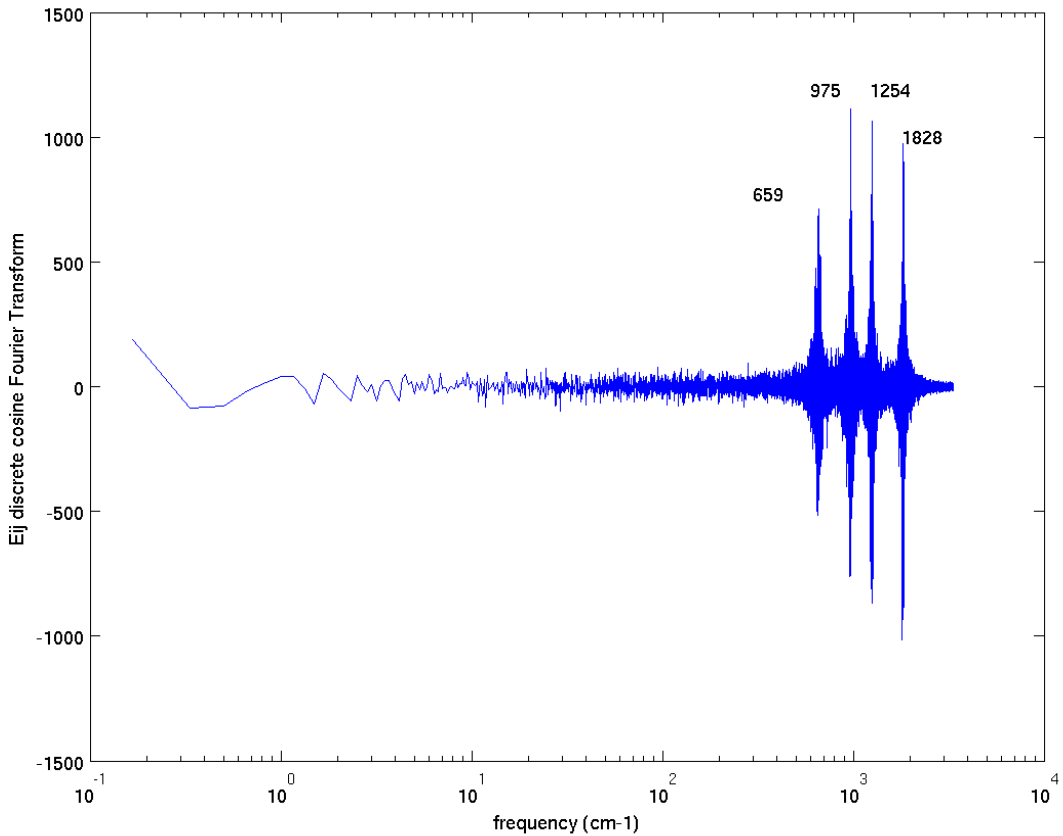


Figure 3-11 Cosine Fourier transform of the autocorrelation function of the vertical energy gap for the excited state on one site in the crystal at 150K.

Four main peaks were obtained in cosine transform of ΔE_{ij} in Figure 3-11 vibration modes from the experimental Raman spectrum⁹⁷ of benzene in Figure 3-12 match along with each main peak. The figure shows the computed spectrum of benzene, where the peaks at 1828, 1254, 975, and 659 cm^{-1} represent its characteristic features. The peak at 1828 cm^{-1} possibly represents the C-C-C stretching vibration mode (Figure 3-13(a)), which is 15% higher than experimental counterpart. The peaks at 1254, 975, and 659 cm^{-1} have good agreement with Raman spectrum with up to 10% difference, corresponding to C-H shear vibration mode (Figure 3-13(d)), the benzene ring breathing vibration mode (Figure 3-13(b)), and C-C-C deformation in plane

vibration mode (Figure 3-13(c)), respectively. It is noted that 3063 cm^{-1} and 2950 cm^{-1} in the experimental spectrum, representing the C-H symmetrical and anti-symmetrical stretching vibration mode, respectively, cannot be observed in the computed spectrum, since the C-H bond was constrained in MD simulations.

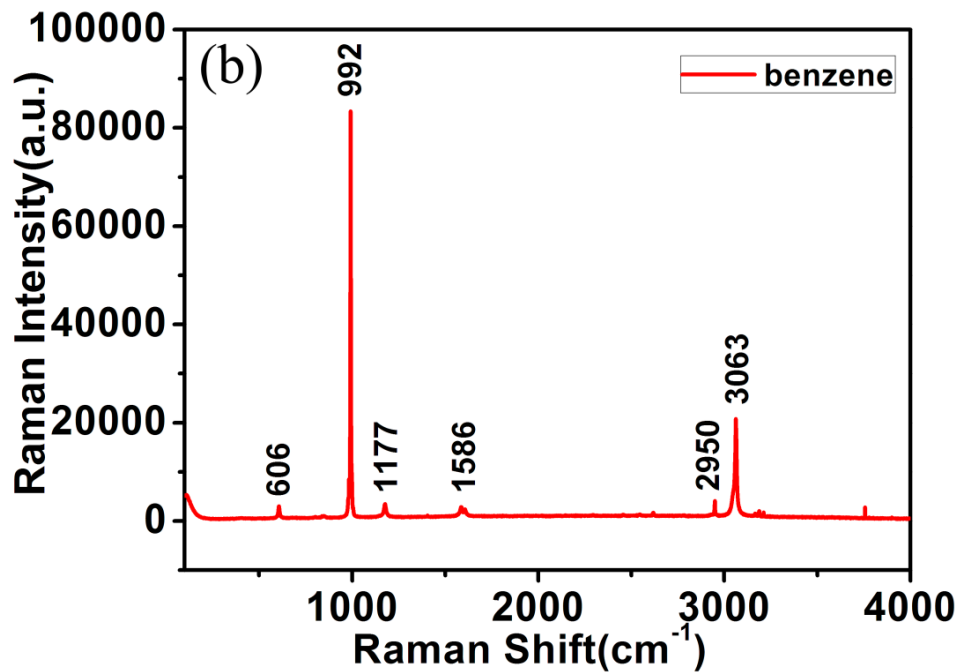


Figure 3-12 Experimental Raman spectrum of benzene, in powder, with the main peaks marked. Data are from ref⁹⁷.

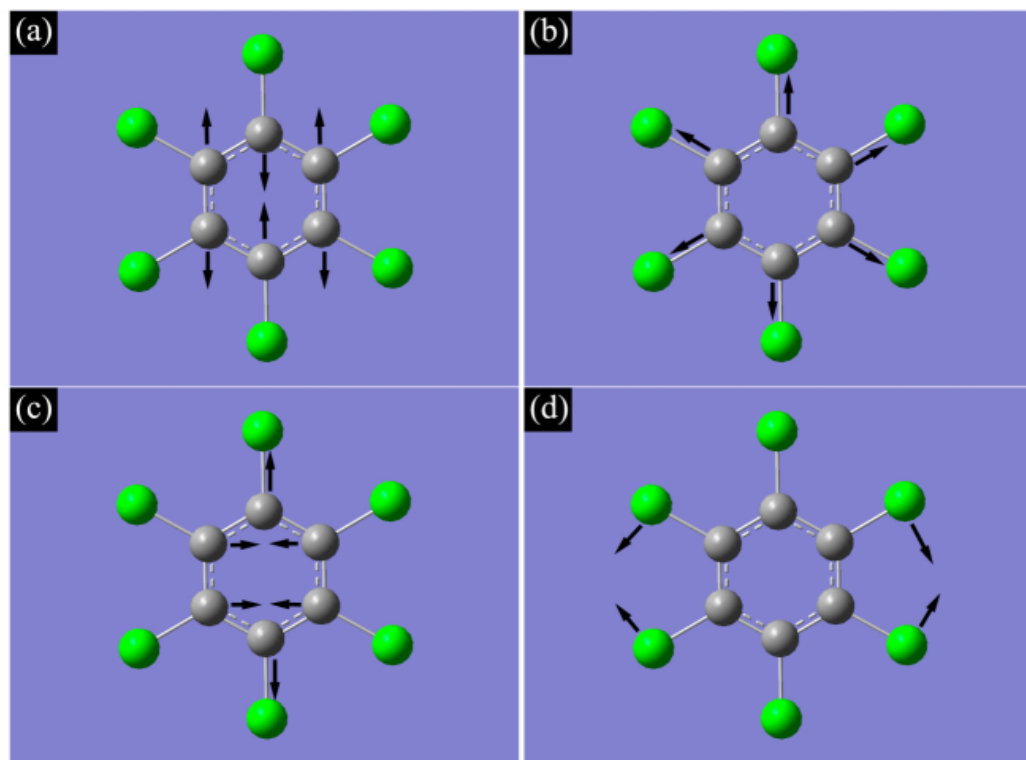


Figure 3-13 Illustration of vibration in benzene for: (a) C-C-C stretching vibration mode; (b) benzene ring breathing vibration mode; (c) C-C-C deformation in plane vibration mode; (d) C-H shear vibration mode.

Table 3-5 Comparison of experimental Raman spectrum and computational spectrum by E_{ij} frequency analysis for benzene and the corresponding vibration modes

computational peaks from Cosine transform E_{ij} (cm^{-1})	experimental peaks from Raman spectrum (cm^{-1})	difference	vibration mode	panel in Figure 3-13
1828	1586	15.3%	C-C-C stretch	a
1254	1177	6.5%	C-H shear	d
975	992	-1.7%	the benzene ring breathing	b
659	606	8.7%	C-C-C deformation in plane	c

3.3.4 Frequency analysis for benzene crystal

For calculation of the rate constants k_{ij} one needs to make a choice how to average over the ET parameters that appear in the rate equation Eq 1 (electronic couplings, site energies and reorganization energies).

Here I use the thermal average of the site energies and reorganization energies to evaluate the rate with each instantaneous value of the electronic coupling (i.e. I do not average over the couplings). This results in a distribution of k_{ij} , shown in Figure 3-14 in red. We see that the rates span 2-3 orders of magnitude ranging from 10^{11} to 10^{13} Hz corresponding to an average hopping time of about 0.4 ps. Importantly, the rate distribution is well separated from the distribution of the site energy distribution (shown in blue). The latter is at frequencies 1-2 orders of magnitudes higher than the rates. Therefore, the electron will see an average site energy difference during the electron hop, justifying the use of the average energy level difference in the calculation of the ET rate.

The situation is more complicated for the electronic couplings. The distribution obtained from the same MD trajectory is shown in Figure 3-14 in green. The coupling distribution strongly overlaps with the rate constant distribution. This means there is no time scale separation: ET occurs on the same time scale as the electronic coupling fluctuations. Therefore, strictly speaking, it is not justified to average over the couplings to calculate the rate constant, nor is it justified to calculate the rate constants

for different coupling values (as done here) and then average over the rate distribution.

Our remedy to this problem is to carry out mobility calculations for both averaging procedures and investigate whether this makes any difference to the final result.

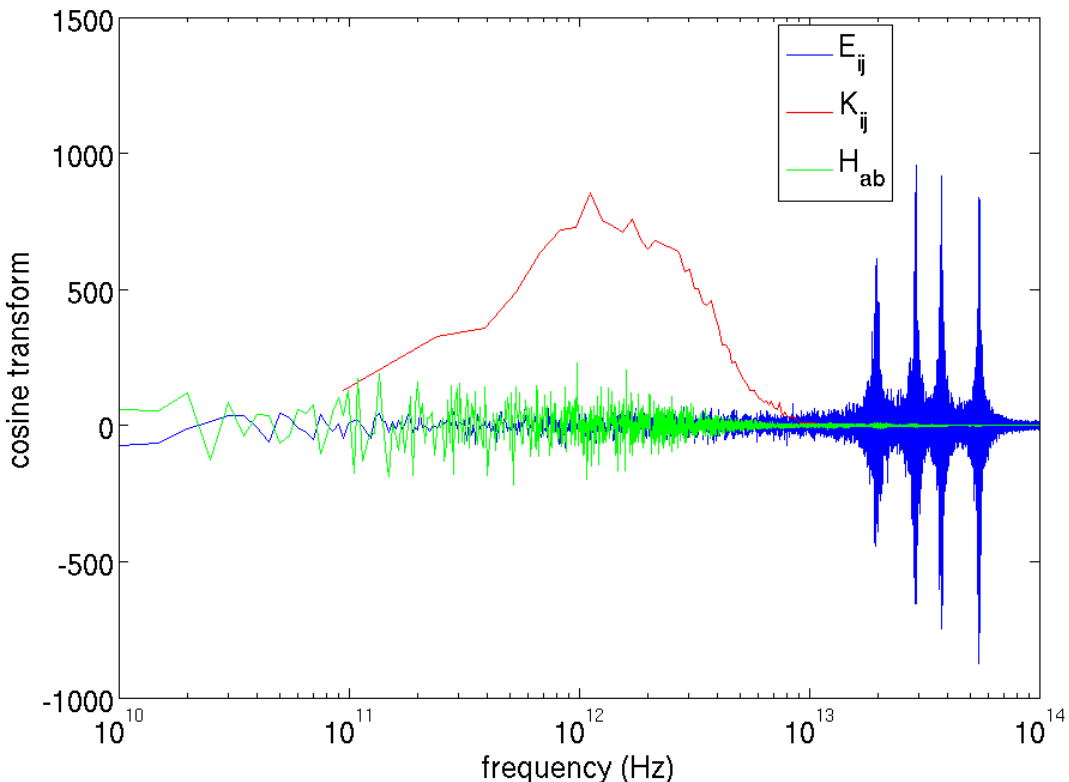


Figure 3-14 Time scale of rates k_{ij} and cosine transform of the autocorrelation function of the vertical energy gap of the excited states ΔE_{ij} and the electronic coupling between the excited states of the neighboring molecules in benzene at 150K.

3.3.5 Mobility calculation and convergence of KMC

In this KMC algorithm, generalised rate expression Eq 1 was used. The inputs of the method are the activation energies for all possible jumps, the electronic coupling matrix element between the molecules of interest, the reorganisation energy, and the

effective nuclear frequency along the reaction coordinate. The code also accounts for the nuclear motions in the crystal within MD trajectories. All these electron transfer parameters except for the effective nuclear frequency required to calculate hopping rates were computed in previous studies. The effective nuclear frequency can be obtained from MD simulation by spectral deconvolution of the reorganization free energy. The effective nuclear wavenumber is 1359.5 cm^{-1} (equal to 168.23 meV) for benzene.

The convergence of the electronic mobilities was tested with respect to the number of KMC trajectories for benzene. The results show $10^5 - 10^6$ are suitable numbers of KMC trajectories needed to reach convergence (a similar result is obtained for pentacene and C₆₀). Mobilities are then calculated for each snapshot taken from the equilibrium trajectory and equidistantly spaced by 1 or 10 ps (use the spacing that applies to benzene here).

Figure 3-15 shows the mobility value for each snapshot along the 100 ps trajectory for benzene at 150K by Einstein method. The continuous curves present the accumulated average of the mobility vs time snapshot. The simulation showed that 1×10^5 individual KMC trajectories for a single snapshot are enough to reach convergence. The fluctuation of mobilities is because of the fluctuation of corresponding electronic couplings. Anisotropic property is observed with high mobility in xy-plane and low mobility along z axis. The Einstein method predicts slightly higher mobility than

numerical derivative method. Unfortunately, there is little experimental mobilities for a benzene crystal to compare with.

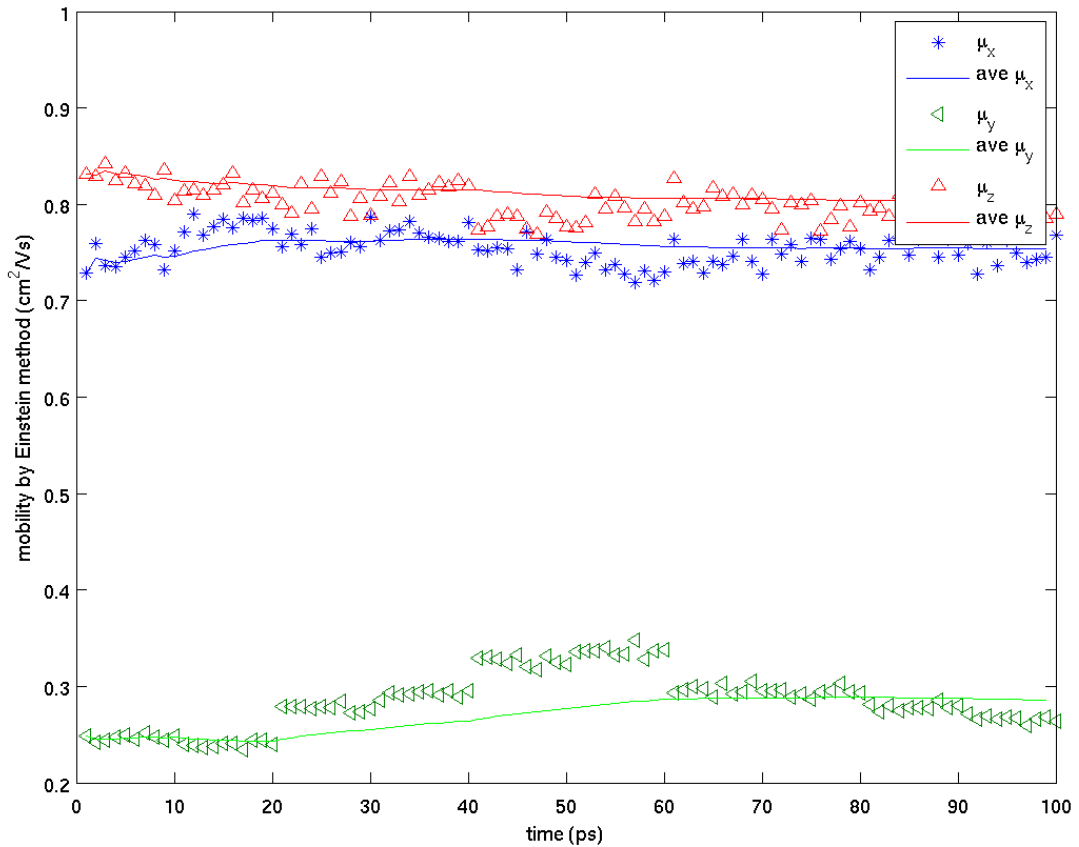


Figure 3-15 Mobilities computed by Einstein method. Each point is a mobility value for each snapshot equidistantly spaced along the 100 ps trajectory for benzene crystal at 150K. The continuous curves present the accumulated average of the mobilities vs time snapshot.

3.4 Rubrene, Pentacene, and C₆₀

3.4.1 Thermal distributions of electronic couplings

The thermal distribution of electronic couplings H_{ij} are shown in Figure 3-16 1d, e and f for rubrene, pentacene and C₆₀ at room temperature (300 K). They span about 5 orders of magnitude from 10^{-3} to ~ 200 meV. For rubrene and pentacene the total distribution is broken down in distributions for nearest neighbour pairs along the

directions indicated in panels (a) and (b). The latter are very well approximated by Gaussian fit functions in Figure S3, $P(|H_{ij}|) = A \exp[-(|H_{ij}| - \langle |H_{ij}| \rangle)^2/(2\sigma^2)]$, with R^2 values between 0.937-0.998 (see Table 3-6). Rubrene exhibits the strongest electronic coupling along the P (“Parallel”) direction (83.5 meV) due to almost perfect pi-pi stacking in this direction. The coupling between the T-shaped pairs (T) within the same herringbone layer is significantly smaller but still sizable. In pentacene there are no pairs that form ideal pi-stacking interactions as in rubrene but there are two T-shaped motifs within the herringbone layer (T1 and T2) that exhibit large electronic couplings (66.3 and 41.4 meV, respectively). In both materials the width of the coupling distribution is of the same order of magnitude as the mean, which is a common characteristic of OSs. The mean coupling values obtained here from our ultrafast AOM method are in good agreement with values reported in previous investigations^{17,98-100} (see Table 3-6).

Table 3-6 Mean values ($\langle |H_{ij}| \rangle$) and root-mean square fluctuations (σ) for electronic coupling matrix elements for inter-molecular hole transfer in rubrene and pentacene and for electron transfer in C₆₀.^a

crystal	dimer type	distance of center of mass (Å)	$\langle H_{ij} \rangle$ (meV)	σ (meV)	correlation coefficient ^b	$\langle H_{ij} \rangle$ literature values (meV)
rubrene	P	7.2 ± 0.2	83.5 ± 0.3	17.2 ± 0.5	0.980	$78^e, 107^f$
	T	8.0 ± 0.3	19.3 ± 0.2	11.6 ± 0.2	0.997 ^c	$10^e, 21^f$
pentacene	T1	4.8 ± 0.1	66.3 ± 0.5	24.6 ± 0.9	0.937	$96.7^g, 81^f$
	T2	5.2 ± 0.2	41.4 ± 0.7	22.5 ± 0.3	0.979	$64.0^g, 68^f$
	P	6.3 ± 0.3	17.6 ± 0.3	12.1 ± 0.2	0.985	$41.7^g, 39^f$
C ₆₀	P	10.0 ± 0.1	16.7 ± 0.1	3.9 ± 0.1	0.998 ^d	14 ^h

a. All H_{ij} values reported are obtained from the analytic overlap method (AOM)³⁶ and averaged over a 1 ns MD trajectory at

300 K. Statistical uncertainties due to the finite length of the trajectories are obtained from block averages (blocksize = 200 ps).

- b. Fit to a single Gaussian $P(|H_{ij}|) = A \exp(-(|H_{ij}| - \langle |H_{ij}| \rangle)^2/(2\sigma^2))$, unless noted otherwise.
- c. Fit to two-Gaussians $P(|H_{ij}|) = A_1 \exp(-(|H_{ij}| - \langle |H_{ij}| \rangle_1)^2/(2\sigma_1^2)) + A_2 \exp(-(|H_{ij}| - \langle |H_{ij}| \rangle_2)^2/(2\sigma_2^2))$.
- d. Fit to a log-normal distribution ($\log(|H_{ij}|)$ instead of $|H_{ij}|$).
- e. Ref.⁹⁸. H_{ij} values were obtained using a fragment orbital approach and Zerner's intermediate neglect of differential overlap.
- f. Ref.⁹⁹. H_{ij} values were obtained by the energy-splitting-in-dimer (ESID) method, where the electronic coupling is approximated to be half of the energy splitting between the HOMO and HOMO-1 in the dimer, in case where charge transfer from HOMO of molecule 1 to HOMO of molecule 2 is considered.
- g. Ref.¹⁰⁰.
- h. Ref.¹⁷. H_{ij} values obtained from fragment orbital density functional theory (FODFT).

In contrast to rubrene and pentacene, C₆₀ (panel f) exhibits only one single peak due to the free rotational diffusion of the buckyballs around their lattice sites at 300 K, averaging out any directional dependence. The distribution is better described by a log-normal distribution ($R^2= 0.998$) than by a Gaussian ($R^2= 0.979$) due to a long tail at larger coupling values. A similar observation has been made for the C₆₀ derivative PCBM in Ref.¹⁵. We also note that the mean coupling value for C₆₀ (16.7 meV) is much smaller than for rubrene and pentacene. This is a consequence of the large spatial extent of the SOMO orbital of C₆₀⁻ and the small orbital coefficients on any of the carbon atoms including the ones on donor and acceptor that are in van-der Waals distance and contribute most to the coupling. Evidently, the isotropy of electronic coupling and charge mobility in room temperature C₆₀ (which is beneficial in actual devices) is paid for by the modest electronic coupling strength.

The sensitivity of the coupling distribution with respect to a change of temperature is shown in Figure 3-16 g, h and i. We find three qualitatively distinct T -dependences for rubrene (panel g), pentacene (panel h) and C₆₀ (panel i). The distribution for rubrene is found to be very robust in the wide temperature interval 100-500 K. The

qualitative features in the distribution are retained even at temperatures as high as 500 K. The peaks just become slightly wider and shift to somewhat smaller values. By contrast, the peaks for pentacene gradually disappear and coalesce to a smooth distribution as the temperature is increased, whereas for C₆₀ the peaks gradually merge in a single, broad peak.

The different behaviour is due to the different packing structure and degree of orientational disorder of the molecules. Whilst the rubrene molecules are “locked” to their lattice sites by the bulky phenyl groups, the pentacene molecules undergo strong hindered rotations around their lattice sites as the temperature is increased. Hence, pentacene becomes structurally much more disordered than rubrene as the temperature is increased, resulting in a continuous, featureless coupling distribution at 500 K. The effect of thermal motion is even more pronounced in case of C₆₀ (panel i). Below 255 K rotation of the buckyballs around their lattice sites is hindered⁸³ resulting in a peaked distribution. Above that temperature they have enough kinetic energy to rotate freely. The molecules are then orientationally fully disordered, resulting in a single smooth distribution.

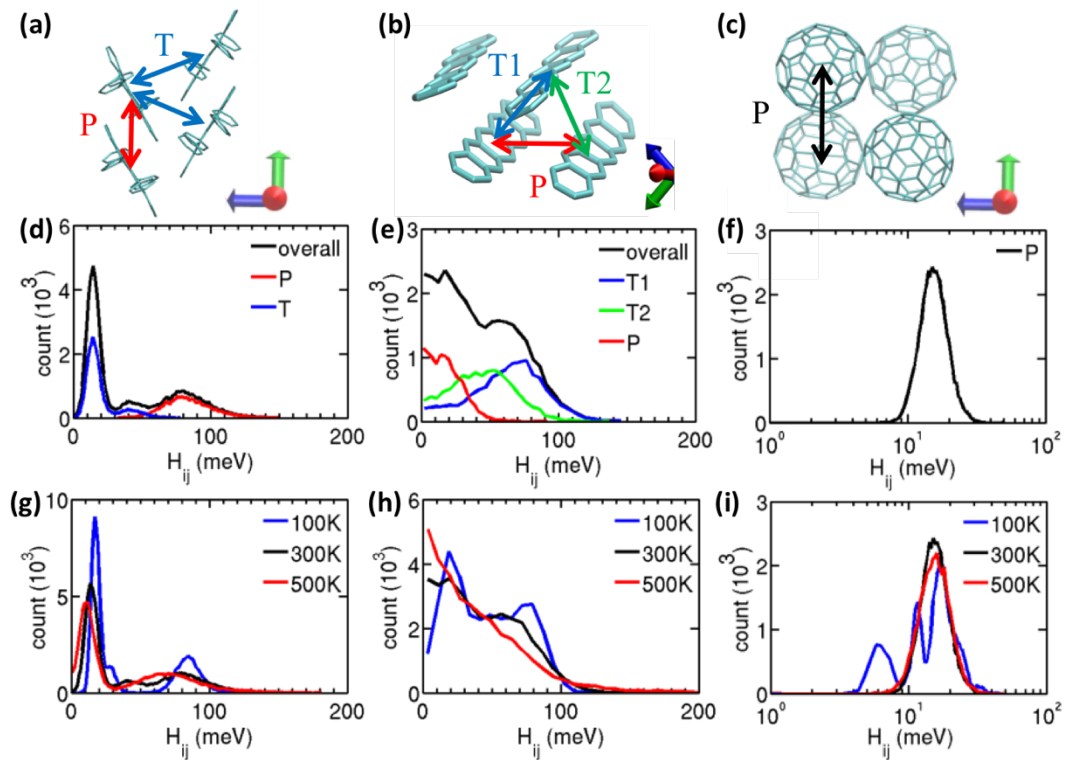


Figure 3-16 (a)-(c) Orientation of nearest neighbour molecular pairs in pentacene (a), rubrene (b) and C₆₀ (c) crystals. Arrows at the right bottom corner in each panel point in the direction of eigenvectors of the mobility matrix for each system. (d)-(f) Distribution of electronic coupling matrix elements |H_{ij}| for hole transfer between nearest neighbor pairs in rubrene (d) and pentacene (e), and for electron transfer in C₆₀ (f). The data are obtained from 1 ns MD simulation at 300 K. The overall distribution is shown in black and the decomposition in contributions from different directions is shown in colour. P and T denote parallel and transverse direction, respectively. (g)-(i) The overall distributions of electronic coupling matrix element for all nearest neighbor pairs at different temperatures for rubrene (g), pentacene (h) and C₆₀ (i).

3.4.2 Thermal distributions of site energies

The thermal distributions of site energy differences between molecules, ΔE_{ij} , are shown in Figure 3-18a. They are well described by Gaussian distributions centered at zero mean. The mean gap vanishes because the molecules i, j are chemically identical and interact with similar environments. The width of the distributions is significantly larger for rubrene than for pentacene or C₆₀ in accordance with the larger inner sphere-reorganization energy λ_i for rubrene. In addition, we find that the width increases

linearly with temperature and the slope is approximately proportional to λ_i (Figure 3-18 b). This can be understood by the well known relation for Gaussian energy gap distributions,²⁸ $\sigma^2 = 2k_B T \lambda$, implying that λ is virtually T -independent.

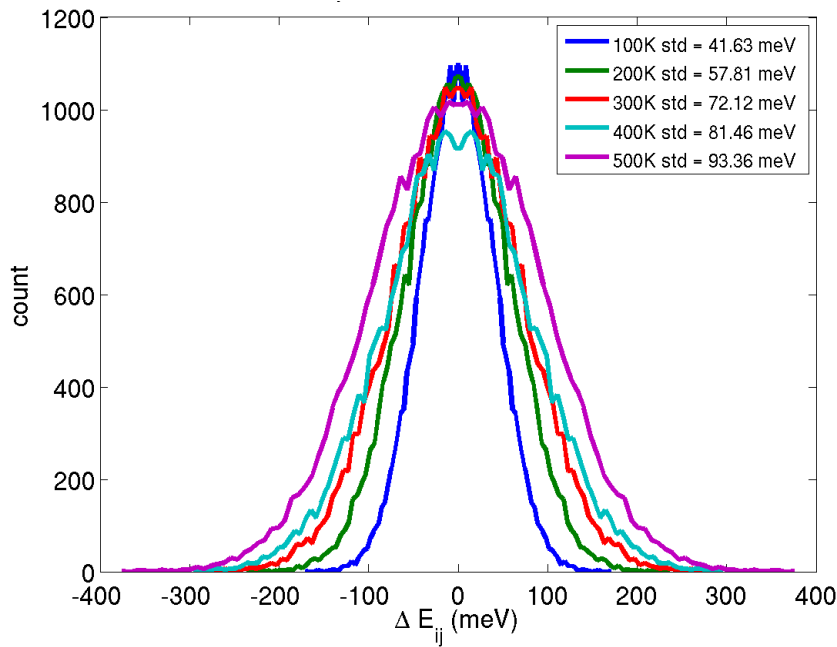


Figure 3-17 Temperature sensitivity of site energy difference distribution from 1ns-long MD simulation for nearest neighbours for pentacene.

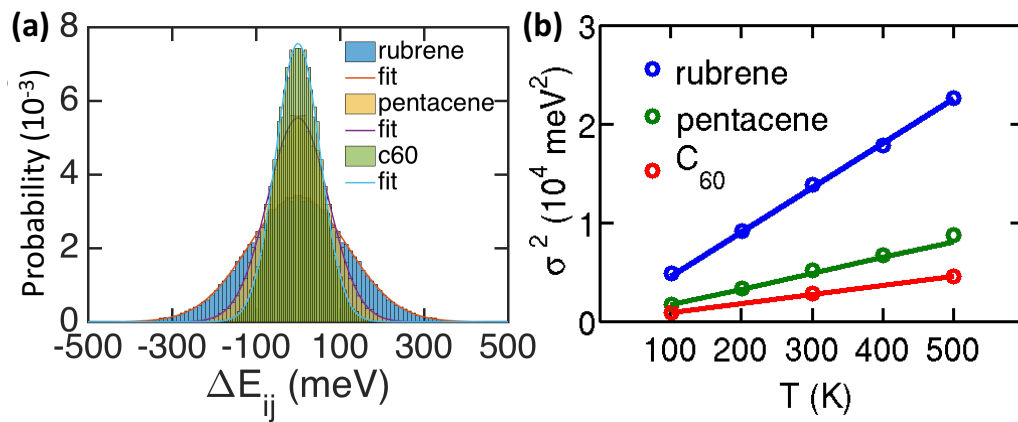


Figure 3-18 (a) Distribution of site energy difference from 1ns-long MD simulation for nearest neighbours at 300K. (b) Linear relationship between variance of site energy difference and temperature.

3.4.3 Timescales of fluctuations

An analysis of the time scale of the fluctuations gives a complementary perspective on electronic couplings and site energy difference. Besides, it gives insight how those energies should be averaged for the calculation of ET rates. To this end I have carried out a frequency analysis of the fluctuations for a single CT event between two nearest neighbour molecules (Figure 3-19). For rubrene and pentacene the electronic coupling fluctuations extend from the nanosecond domain (lower limit of our simulation) well into the 0.1 ps regime (100 cm^{-1}) typical of low frequency molecular motion (e.g. hindered rotations). Therefore, the coupling fluctuations strongly overlap with the spectrum for the site energy difference. The situation is different for C_{60} . The coupling fluctuations (1-10 ps) are slower than for rubrene/pentacene due to slow rotations of C_{60} (high moment of inertia) correlating well with the orientational correlation time of C_{60} (10 ps)⁸³. There is no overlap with the spectrum for site energy fluctuations which is dominated by two high-frequency modes, the C=C stretch (1650 cm^{-1}) and breathing mode (485 cm^{-1}). This implies that in C_{60} electronic coupling can be considered as static on the time scale of the site fluctuations, whereas in rubrene and pentacene coupling and site energy fluctuations occur on the same time scale.

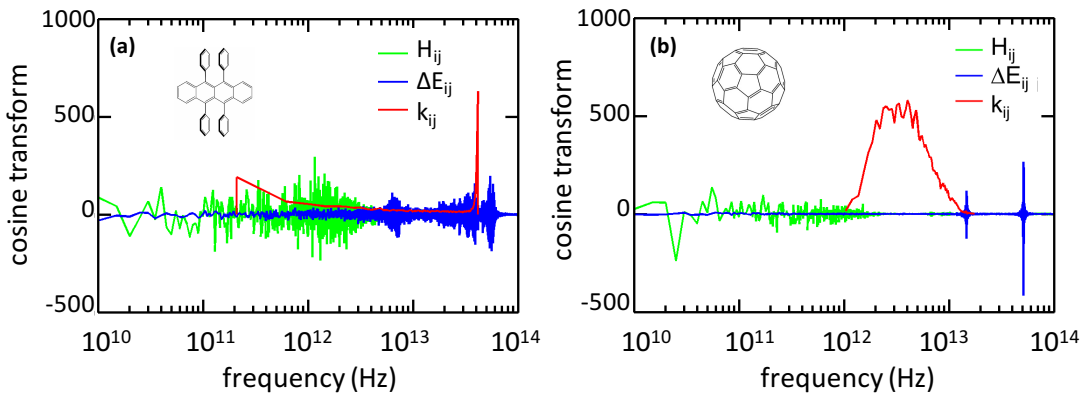


Figure 3-19 Frequency analysis of ET parameters electronic coupling (green) and site energy difference (blue) for rubrene (a) and C₆₀ (b) at room temperature. The distributions for the corresponding inter-molecular charge transfer rates (Eq 1) are shown in red.

3.4.4 Existence of small polaron

Having characterized the magnitude and the thermal fluctuations of electronic couplings and site energy differences, we are now in the position to investigate whether small polarons can form in these materials. This is the case when the nuclear distortions in response to the charging of a molecule i create a sufficiently deep potential well so that the excess charge remains localized on the molecule. A necessary condition for small polaron formation to occur is that the activation free energy for charge transfer between the molecules i and its neighbours j , Eq 5, is finite, $\Delta A_j^\dagger > 0$. Eq 5 implies that the free energy barrier disappears, $\Delta A_j^\dagger = 0$ for $|H_{ij}| > \lambda/2$. In this case, charge localized states no longer form and the rate formula Eq 1 for polaron hopping becomes inapplicable. (For two-state systems Rabi-oscillations occur instead, as discussed in ref³⁹)

I have calculated the activation free energies Eq 5 for rubrene, pentacene and C₆₀ for the different electronic coupling values obtained from MD. Here, the distributions of activation free energies are compared with feeding instantaneous and averaged site energy differences in the calculations of ET rates, respectively. Because as we can see from Figure 3-19, site energy fluctuations and ET rates occur on the same time scale for rubrene and pentacene. I find that for a large fraction of configurations the activation free energies Eq 5 vanishes: 29.9% for rubrene and 28.9% for pentacene when rates are calculated for instantaneous site energies and 32.6 % for rubrene and 50.9% for pentacene when average site energy differences are used. The latter has been used in my mobility calculations since I assume that the fluctuations of site energy differences determining λ_{ij} and ΔA_{ij} are much faster than for electronic coupling, and can thus be averaged over. Thus, the resultant distributions for activation free energy are shown in in Figure 3-20.

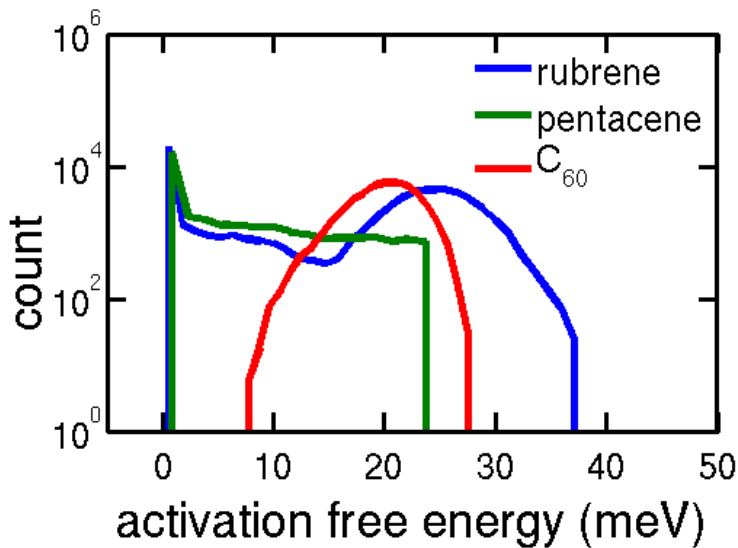


Figure 3-20 Distribution of activation free energy (ΔA_j^\dagger , Eq 5) when average site energy differences are used for inter-molecular charge transfer in rubrene, pentacene and C_{60} . Note the peak at vanishing activation free energy ($\Delta A_j^\dagger = 0$) for rubrene and pentacene.

Unsurprisingly, in rubrene most of the activationless transitions are for the P pairs, and in pentacene for the T1 and T2 pairs, all of which exhibit high electronic couplings. For C_{60} no configuration with vanishing activation free energy was found due to the smaller electronic couplings in this crystal, but a large fraction of activation free energies is below the thermal energy, implying that small polarons would be thermally unstable in this system. These findings are very similar to the results obtained previously in the group for the fullerene derivative PCBM.¹⁰¹

3.4.5 Charge mobility

The disappearance of an activation barrier for a significant number of configurations means that the charge carrier will delocalize and possibly form percolation paths. On the other hand, the thermal fluctuations of the site energies and couplings may lead to (temporary) re-localisation of the carrier. Therefore, a good theory for this problem should not make any *a priori* assumptions with regard to the degree of localisation of the charge carrier. In this regard, non-adiabatic molecular dynamics simulation techniques that explicitly propagate the charge carrier wavefunction in the time-dependent external (nuclear) potential may present a way forward to deal with this challenging problem.^{39,62,63,102-104} Our group has recently developed such a methodology based on Tully's fewest switches surface hopping³⁹ and successfully applied it to small model systems. Unfortunately, the calculation of charge mobilities for the 3D crystals studied here are still out of reach and will be a major objective of future work. Here I proceed with the calculation of charge mobilities assuming charge hopping even though we know from the above analysis that this model is problematic. Nonetheless, the results obtained for charge hopping are of interest because mobilities obtained from any improved theoretical approach (including non-adiabatic MD simulation) will be compared to hopping mobilities as this has been the most popular and widely used model in the literature for the last ten years.

Hopping mobilities were calculated for rubrene, pentacene and C₆₀ using Kinetic Monte Carlo (KMC) simulation as detailed in Section 2.1.5. The eigenvalues of the

charge mobility tensor obtained for the structures from 1ns MD are shown in Figure 3-21 (for 300 K), and the averaged eigenvectors are indicated as arrows in Figure 3-16a, b, and c. The calculations can reproduced experimental mobilities and anisotropy well (Figure 3-22 and Table 3-7).

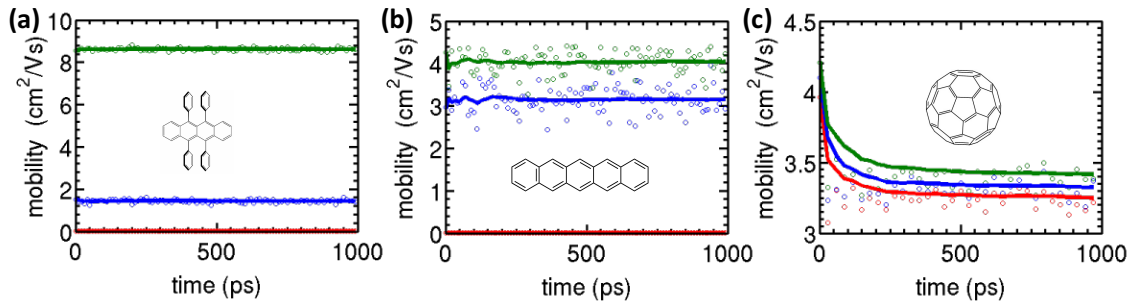


Figure 3-21 Charge hopping mobilities at room temperature as obtained from KMC simulation. Data points are instantaneous mobility values for snapshots equidistantly spaced along the 1ns trajectory and continuous curves present the accumulated average of the mobilities vs time. The corresponding eigenvectors of the mobility tensor are shown as arrows in Figure 3-16 (a)-(c) using the same color code. The strong thermal fluctuations of pentacene molecules around their lattice sites cause significant fluctuations in instantaneous mobility, in contrast to rubrene where mobility is virtually independent on the structure used. The mobilities for C₆₀ become converged only after about 300 ps due to the slow rotational diffusion of the buckyballs.

Rubrene exhibits 2D conduction within the herringbone layer with the highest mobility along the parallel (P) direction ($\mu_1 = 8.71 \text{ cm}^2 \text{ V}^{-1} \text{ s}^{-1}$) and a smaller mobility along the direction intersecting the two transverse (T) directions ($\mu_2 = 1.44 \text{ cm}^2 \text{ V}^{-1} \text{ s}^{-1}$). The mobility along the long molecular axes, perpendicular to the herringbone layers, is nearly zero. Pentacene also exhibits 2D conduction, yet the highest mobility is slightly lower than in rubrene ($\mu_1 = 4.07 \text{ cm}^2 \text{ V}^{-1} \text{ s}^{-1}$ along T1) and the anisotropy within the herringbone layer is smaller ($\mu_2 = 3.19 \text{ cm}^2 \text{ V}^{-1} \text{ s}^{-1}$ along T2). For C₆₀, the room temperature mobility obtained is somewhat smaller than for pentacene ($\mu = 3.30$

$\text{cm}^2 \text{V}^{-1} \text{s}^{-1}$). Overall, the agreement with previously reported theoretical hopping mobilities is good (see Table 3-7). Within the hopping model used, mobility can be easily understood in terms of the electronic coupling strength along the respective hopping directions because all other ET parameters are the same for the different directions of a given OS or similar for the different OSs investigated.

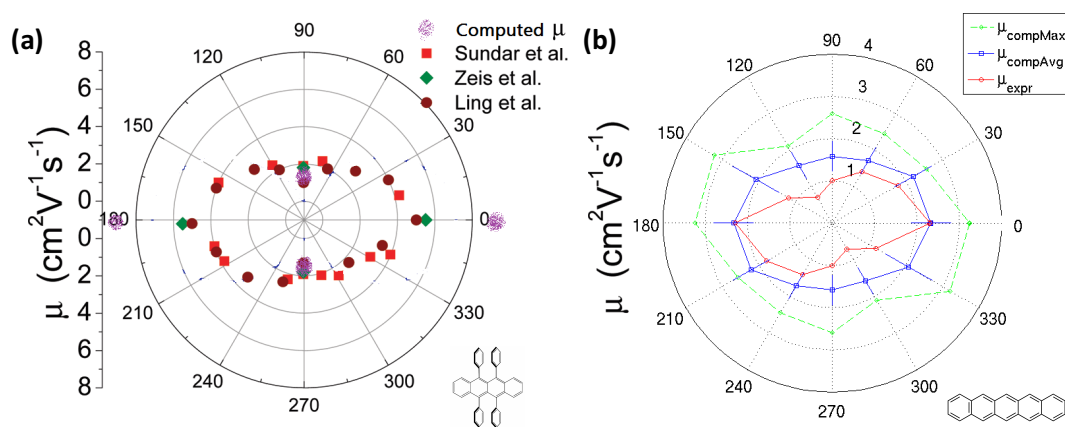


Figure 3-22 Comparison of computed mobilities with experimental mobilities and their anisotropy for rubrene(a), pentacene(b) at room temperature.

Table 3-7 Comparison of computed mobilities from the literature and from current work with experimental mobilities at room temperature. All values are given in $\text{cm}^2/(\text{Vs})$.

	rubrene		pentacene		C_{60}
	μ_1	μ_2	μ_1	μ_2	μ
computed this work	8.7	1.4	4.07	3.19	3.30
computed literature	8.1 ^a , 3.1 ^b , 43 ^c		3.5 ^b , 2.2 ^f		3.0 ⁱ
experimental	20 ^d , 10 ^e	7.6 ^d	2.3 ^g , 11 ^h	0.7 ^g	0.5 ± 0.2^j

^a Ref. ⁹⁸, charge hopping model.

^b Ref. ⁹⁹, charge hopping model.

^c Ref. ¹⁰⁵, charge propagation using model Hamiltonian.

^d Ref. ¹⁰⁶ Field-Effect-Transistor (FET) mobility, surface of single crystal.

^e Ref. ¹⁰⁷ Hall mobility, surface of single crystal.

^f Ref. ¹⁰⁰, charge hopping model.

^g Ref. ¹⁰⁸ FET mobility.^h Ref. ¹⁰⁹ Space-charge-limited current (SCLC) mobility as measured. Corrected to $\mu_1 = 35 \text{ cm}^2/(\text{Vs})$ using effective crystal thickness.ⁱ Ref. ¹⁷, charge hopping model.^j Ref. ¹¹⁰, time-of-flight mobility.

The computed mobilities in this work have very good agreement with the mobilities reported in the literature that use charge hopping model for all these three molecular crystals, while band mobilities are higher than hopping mobilities in general due to the electron delocalization assumption. In terms of experiments, there are various mobility characterization methods. Among these, time-of-flight is the most likely measurement to provide comparable mobilities to this work. Because both of them reflect intrinsic mobilities of bulk materials without imposing any external fields. But unfortunately, time-of-flight mobilities have not been found in the literatures except for C₆₀ due to the difficulty of both preparing the ultra-pure samples and capturing the weak signal during the measurement. In contrast, other approaches measure the mobilities on the surface of single crystal applying external fields. As a result, the concentration of charge carriers greatly enhanced so that the mobilities are higher than intrinsic mobilities.

The room temperature mobilities predicted by the hopping model are in surprisingly good agreement with experimental values¹⁰⁷⁻¹¹³ (see Table 3-7, deviation of about a factor of 0.09-6.4 depending on the experiment). However, the shortcomings of this model manifest themselves in the temperature-dependence of charge mobility (Figure 3-23). The mobility decreases with temperature as T^{-n} where $n \sim 1$ ($n = 1.00$ for

rubrene and $n = 1.16$ for pentacene), whereas in experiment $n = 1.38$ for rubrene¹⁰⁷ and $n = 2.61$ for pentacene¹⁰⁹. As the hopping rates and diffusion constant obtained from KMC are almost temperature-independent because of the small or vanishing activation free energies for charge hopping, the T^{-1} dependence of charge mobility is simply due to the denominator in the Einstein Equation (Eq 17). Hence, the hopping model cannot explain the different exponents observed in experiments. This leaves us to conclude that the good agreement with experimental room temperature mobilities is likely to be fortuitous.

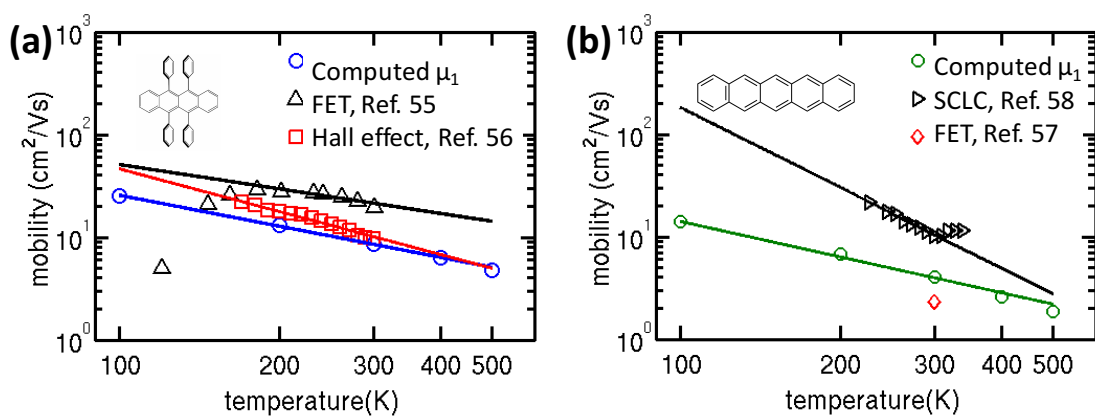


Figure 3-23 Mobility decay with temperature for rubrene (a) and pentacene (b). Computed hopping mobilities are shown in blue and green symbols and experimental mobilities¹⁰⁶⁻¹⁰⁹ in black and red symbols, respectively. Best linear fits are shown in solid lines.

3.5 Band mobility of 1D-chain anthracene

In order to further study charge transport mechanism, I calculate here band mobility as well as hopping mobility and compare calculations with experimental results. The material system I take for this comparative study is anthracene single crystal for which I compute hole mobility along the direction of the highest mobility (along b axes in Figure 3-24). Anthracene has been chosen because the hole mobility tensors of ultrapurified highly perfect anthracene crystal as well as its temperature dependency of all tensor elements have been very well experimentally measured by the time-of-flight method.¹¹⁴ I choose to model a one-dimensional chain along the experimental high mobility direction. This system is small enough to permit mobility calculations with non-adiabatic molecular dynamics simulation and comparison of the latter with the present band and hopping mobility calculations. The non-adiabatic MD simulations are not part of this thesis, however, they will be carried out by another group member in the near future.

The hopping mobilities were computed with the same methodology as before. The band mobilities were calculated using the theory and formula presented in Section 2.2.2. Next I will describe the details of band mobility calculations.

3.5.1 Computational details

The carrier mobility μ in the band theory depends on the effective mass along the transport direction m_e and on the average scattering relaxation time $\bar{\tau}(C, E_l, T)$. m_e ,

C and E_l were obtained by the following procedure using first principle band calculations. m_e is obtained from a parabolic fit of the band structure along the b direction of the crystal. To calculate this band structure, 11 K-points along this axis were chosen.

E_{tot} and E_{vbm} were calculated by dilatation / contraction of the unit cell along the b axes. In these calculations, only the center of mass (COM) of molecules were moved without changing the intramolecular geometry of the molecules. E_{tot} and E_{vbm} were plotted against the unit cell length along b, and fitted by quadratic and linear functions, respectively. Then, C and E_l . were obtained from Eqs 28 and 29, respectively. The first principle band calculations were carried out with the CPMD package,⁸⁶ using DFT with planewave basis and pseudopotentials. A generalized gradient approximation (GGA) functional, Perdew, Burke, and Ernzerhof (PBE),¹¹⁵ is used for exchange-correlation energy. The Monckhorste-Pack scheme¹¹⁶ was used for the Brillouin zone sampling.

The energy cutoff for the wave function is 90Ry. K-point sampling is carried out on a 1*2*2 grid, and k-points ensure the convergence of total energies. The vdW-DF take van der Waals interaction into account.

The DFT-D2 scheme¹¹⁷ is used for the dispersion correction, where Grimme's empirical correction was added to the exchange-correlation potential and forces. Then, the total energy is given by

$$E_{DFT-D} = E_{KS-DFT} + E_{disp} \quad (30)$$

where E_{KS-DFT} is the Kohn–Sham energy and E_{disp} is a dispersion correction.

A periodic supercell of a 1D chain including 12 anthracene molecules was used for hopping mobility calculations. The alignment of the molecules remain similar to the one in the anthracene single crystal along b-axes (see Figure 3-24.).

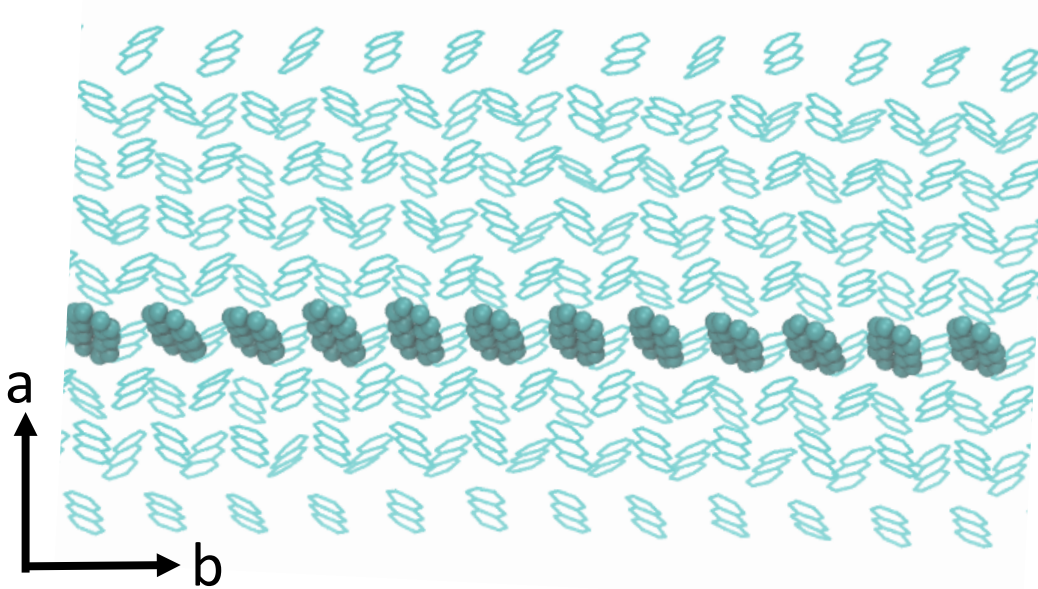


Figure 3-24 1D chain anthracene (highlight) from a single crystal along b-axes.

For band mobility calculation, however, a periodic cell of 12 molecules is too expensive to be carried out, e.g. to run a single wavefunction optimization cycle on this system, it takes $\sim 20\text{min}$ on the ARCHER high performance computing platform. Thus, the model is simplified to a periodic cell of 3 molecules (the band structure of the smallest system consisting only 2 molecules is too flat to fit a second degree polynomial curve.). And then, to eliminate system size effects 5- and 7- molecule systems have been tested.

3.5.2 Dispersion corrections for density functional theory

Van der Waals (vdW) interactions play an important role for the relaxation time. Without vdW-correction, the errors in the lattice constants are large, leading to inaccurate values for C and E_l . Here, I will show the impact of vdW-correction for C fitting.

The total energy E_{tot} against unit cell volumes obtained from the GGA and vdW-correction are shown in Figure 3-25. It is clear that the vdW-correction gives results consistent with the experiment (underestimated by approximately 3%, minima obtained at 0.97a), whereas the GGA functional overestimated the lattice constant (no minima observed). This overestimation of the equilibrium cell length is attributed to the absence of van der Waals interaction in GGA.

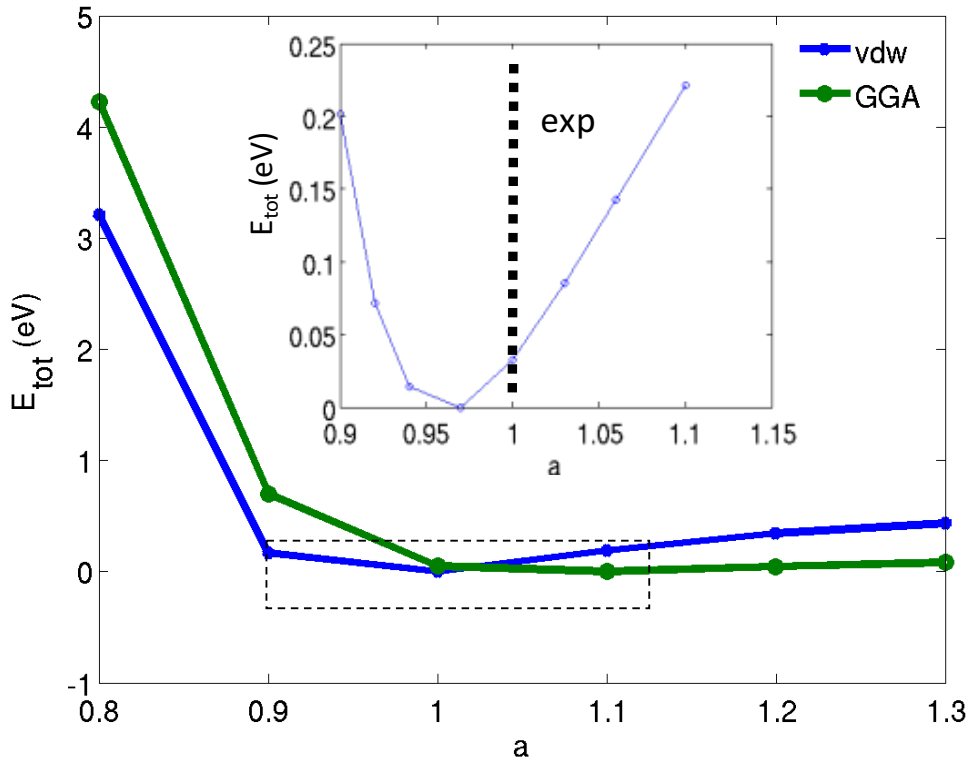


Figure 3-25 The total energy E_{tot} against periodic cell length (normalized with experimental length) a along 1D anthracene. Two curves are obtained with the GGA (green) and vdW-correction (blue), respectively. The insert plot is enlarged view of the block within dash line. The dotted line indicates the experimental a . The energies at equilibrium points are shifted to be zero for both E_{tot} plots.

The elastic modulus C is obtained as $0.152 \text{ eV}/\text{\AA}$ by fitting this parabolic curve from the total energy dependence on the lattice constant.

3.5.3 Size convergence for m_e, E_l

Although band mobility calculations are performed with period boundary condition (PBC), systems with different cell size will have different band structure due to the different number of states. Thus, the system convergence needs to be verified.

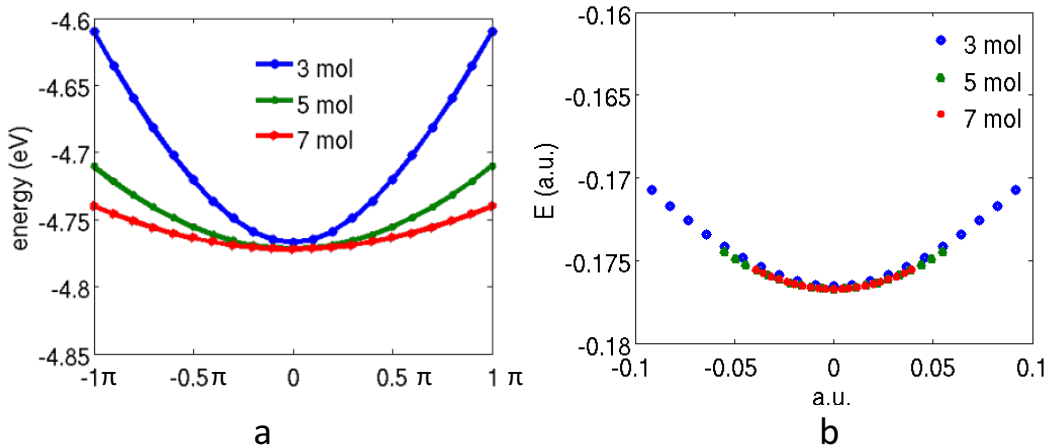


Figure 3-26 (a) HOMO band in \mathbf{b}^{-1} direction in 1D chain anthracene with different size of periodic cell. These periodic cells consist 3, 5 and 7 molecules, respectively. (b) converged curvature of HOMO band by rescaling them with the cell length for 3-, 5- and 7- molecule systems.

An increasing size of systems are tested for band limit calculation. The HOMO band structures of 3 -, 5 - and 7 - molecule systems are shown in Figure 3-26a. The larger the number of the molecules in a periodic cell, the smaller is the curvature of the band. After rescaling the band structure with the supercell length (3 , 5 and 7 times of unit cell lattice along b direction), the curves of 3 -, 5 - and 7 - molecule systems overlay in Figure 3-26b, thus the effective mass m_e exhibits convergence, 1.43, 1.33, 1.30 for 3 -, 5 - and 7 - molecule systems respectively.

Besides, the convergence with E_l also needs to be investigated. It is obtained from the linear fit of the valence band minimum shift with the lattice constant change. The E_{vbm} calculations here are with vdW-correction.

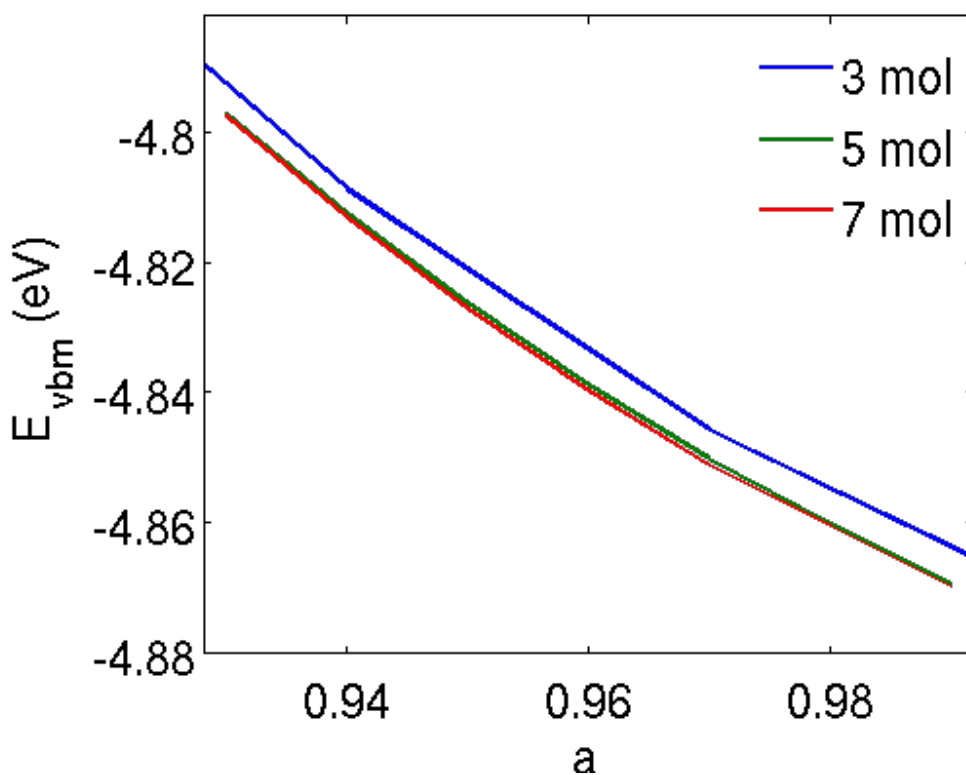


Figure 3-27 The E_{vbm} against periodic cell length, normalized a , along the b direction of anthracene with different size of periodic cell. These periodic cells consist of 3, 5 and 7 molecules, respectively.

3.5.4 Band, hopping and experimental mobilities

Hopping electronic couplings

Anthracene exhibits the strongest electronic coupling between P1 (“Parallel”) dimers (33.0 meV) due to its almost perfect pi-pi stacking in this direction and small intermolecular distance. Therefore, the highest mobility by time-of-flight method was found along the b -axes.¹¹⁴ The coupling between the T-shaped pairs (T) within the same herringbone layer is significantly smaller (18.0 meV) but still sizable.

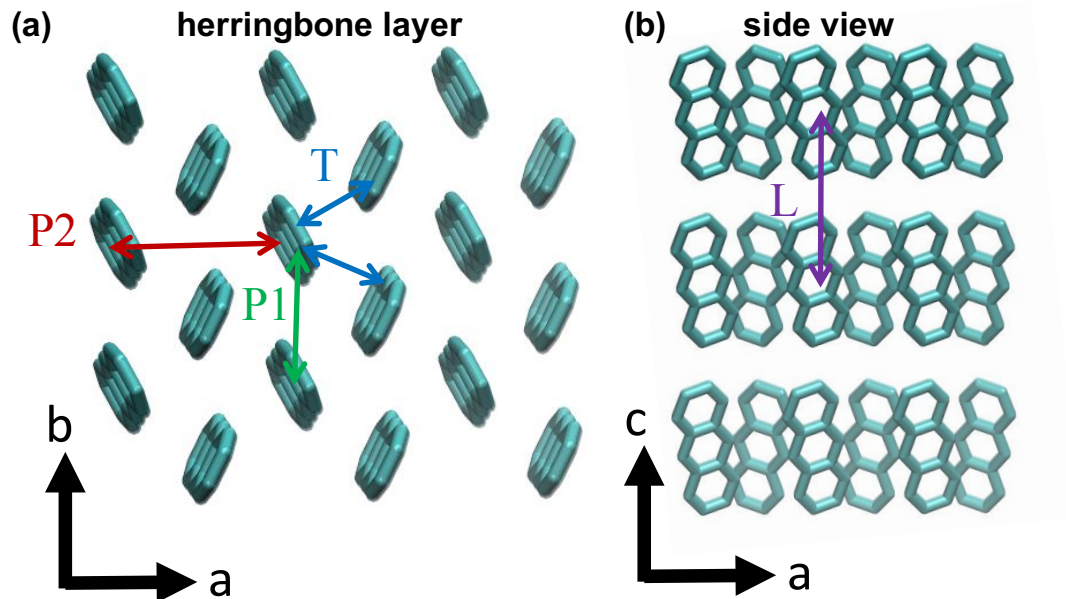


Figure 3-28 Orientation of nearest neighbour molecular pairs in anthracene crystal within herringbone layer (a) and from side view (b).

Table 3-8 Electronic coupling matrix elements for intermolecular hole transfer in anthracene

dimer type	distance of center of mass (Å)	$\langle H_{ij} \rangle$ (meV)
T	5.2	18.0
P1	6.0	33.0
P2	8.6	0.3
L	11.2	0.4

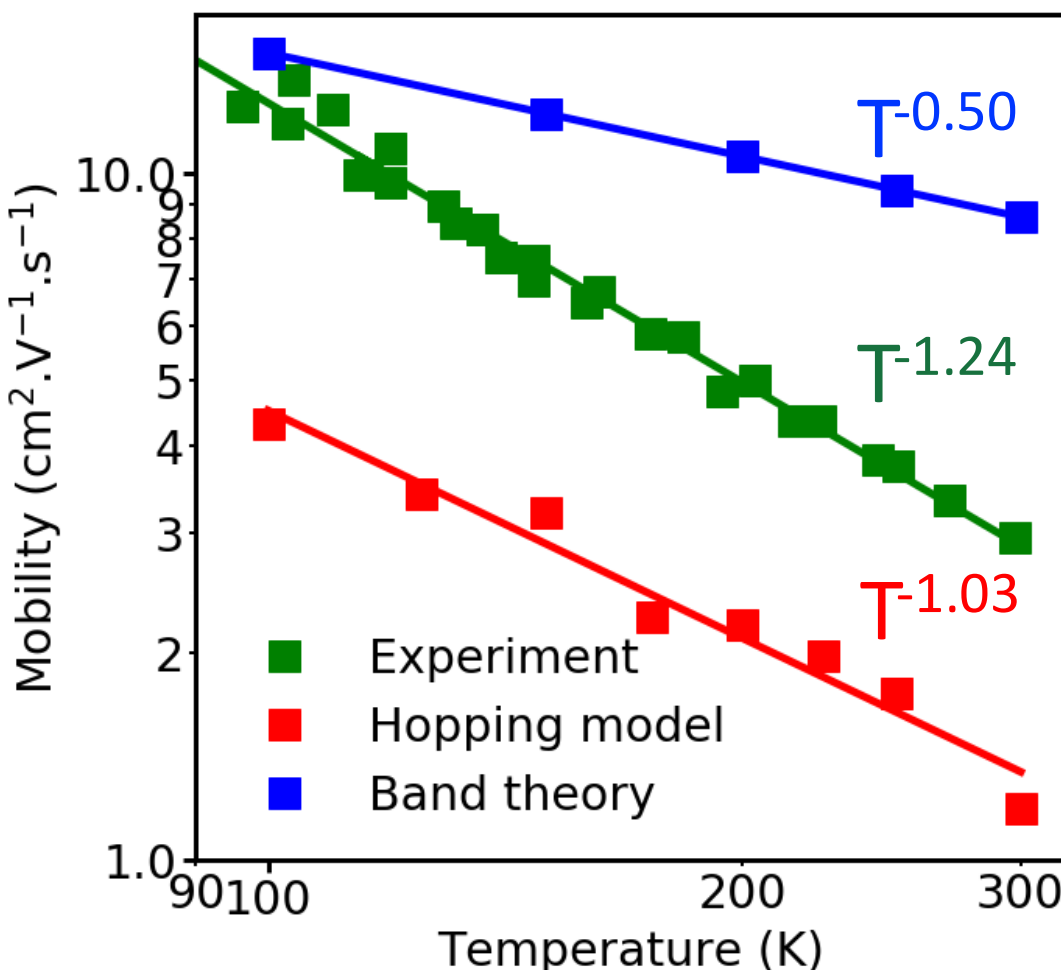


Figure 3-29 Mobility decay with temperature along the direction b. Band, hopping and experimental mobilities are compared.

Anthracene exhibits the highest hole mobility along the parallel (P) direction ($\mu_1 = 3 \text{ cm}^2 \text{ V}^{-1} \text{ s}^{-1}$) and a smaller hop mobility along the direction intersecting the two transverse (T) directions ($\mu_2 = 1.5 \text{ cm}^2 \text{ V}^{-1} \text{ s}^{-1}$) via time-of-flight measurement at room temperature.¹¹⁴ The room temperature mobilities along the b-axes are predicted by the hopping model and band model to be 1.3 and $8.6 \text{ cm}^2 \text{ V}^{-1} \text{ s}^{-1}$, respectively.

At low temperature, the band mobility is very close to experimental data, but it is getting higher and higher than experimental data as the temperature increase. In the

band model in this work, only acoustic modes have been taken into account, and phonons get more pronounced when the temperature is high. The hopping model underestimates the mobility because the charge carrier hop is constrained in this 1-D chain. Zigzag paths for charge carriers have been found when the dimension of the antracene expand to 2D.

The mobility decreases with temperature as T^{-n} where $n \sim 1, 0.5$ for hopping model and band model, respectively, whereas in experiment $n = 1.24$. As the hopping rates and diffusion constant obtained from KMC are almost temperature-independent because of the small or vanishing activation free energies for charge hopping, the T^{-l} dependence of charge mobility is simply due to the denominator in the Einstein Equation (Eq 17). And in band model, $T^{-0.5}$ dependence of charge mobility is simply due to the denominator in $\bar{\tau}$ Eq 27.

3.6 Summary

In this work I have computed the parameters that determine CT in five different OS materials: electronic coupling, reorganization energy, and electron-phonon couplings. I evaluate the validity of polaron hopping model for some of the most popular organic semiconductors, pentacene, rubrene and C₆₀. I find that for a significant fraction of conformations electronic coupling is so large in rubrene and pentacene that a small polaron cannot form. Similar results have been reported for fullerene derivatives by our group¹⁸ and other groups^{15,21} suggesting that this is a more general characteristic

of (crystalline) organic semiconductors. For C₆₀ the coupling matrix elements are smaller and a small but finite barrier for charge transport exists in any transport direction.

My present work substantiates the view that polaron hopping, the most widely adopted model in the chemistry community for the last ten years, is not sound for the description of CT in crystalline OS.¹⁶ The relatively good agreement between computed hopping mobilities and experimental results near room temperature that is often reported in the literature is likely due to a cancellation of errors. This becomes evident when considering the temperature dependence of mobility in the hopping model. The small activation energies lead to an almost T -independent charge diffusion constant at ambient temperatures, resulting in a T^{-1} dependence for any OS investigated. This is in contrast to the experimental T dependence, which decays faster and is specific to the OS considered.

Furthermore, I delivered theoretical insight into another common-used charge transport mechanism, the band theory, from first principle calculations, on the case study of anthracene crystal. The relaxation time was calculated from the acoustic deformation potential model. The effective mass was simply obtained from parabolic fit of the VBM for holes. The computational results show that the band mobilities are approximately one order of magnitude higher than the hopping mobilities, and time-

of-flight mobilities are in between. The mobility decreases with temperature as T^{-n} where $n \sim 0.5, 1$ and 1.24 , respectively.

The discussion of charge transfer parameters and the validity of polaron hopping models in rubrene, pentacene and C_{60} described in this chapter has been published in H. Yang, F. Gajdos, and J. Blumberger, *the Journal of Physical Chemistry C*, vol. 121, pp. 7689-7696, 2017.

<https://pubs.acs.org/doi/10.1021/acs.jpcc.7b00618>

A paper on the methodology comparison of polaron hopping model, band model and non-adiabatic MD in ananthracene is in preparation in the collaboration with Dr Antoine Carof from École Normale Supérieure, France.

4 Pentacene Thin Films

In the previous chapter, I investigated charge transport in single crystalline organic semiconductor materials, and showed that crystalline rubrene and pentacene have high mobility within the herringbone layer. In this chapter, I will move from the intrinsic charge transport study of the three-dimensional perfectly crystalline systems to two-dimensional thin films. I will present the computational research on modeling the experimental structure of few-layer crystalline pentacene thin films on hexagonal boron nitride (hBN). Charge transfer within and between layers are characterized and compared.

The challenges of this work is the setting up of the structural modelling. On one hand, a periodic supercell needs to be built that consists of four different unit cells, one for each of the four layers: substrate layer hBN and three layers of pentacene with different tilt angles. Furthermore, some structural information has not been experimentally reported yet, e.g. the adsorption structure of the first pentacene layer (hereafter denoted wetting layer, WL) on hBN and how they stack. On the other hand, current force field could not reproduce tilt angle differences in the different thin film layers due to some remaining inaccuracies. The structural model of the different layers that includes thermal fluctuations were stabilized using collective variables (short for “colvar”) in molecular dynamics simulations.

After a structural model was obtained, thickness-dependent electrical transport in pentacene thin films was studied. The parameters determining electronic transport in pentacene thin films were calculated, in particular the interlayer and intralayer electronic couplings. Charge mobilities were computed using the hopping model, similarly as in the single crystal. Furthermore, the frequencies of charge hops within the layer and hops between layers are characterized. The results were then compared to calculations on the single crystals formed by the same material.

4.1 Structure of thin film pentacene

4.1.1 Experimental observation

Highly ordered single-crystalline pentacene thin film were grown by Yuhan Zhang, et al. via van der Waals (vdW) epitaxy on hBN.¹¹⁸ The thickness of ultrathin films is varied from mono- to triplelayers in order to study how molecular packing and charge transport are modulated near the interface. The structures have been characterised by atomic force microscopy (AFM), selected-area electron diffraction (SAED) and transmission electron microscopy (TEM), see Figure 4-1 d-f. The molecular packing is schematically illustrated in Figure 4-1 a. The initial wetting monolayer of pentacene lies flat on the hBN with thickness as small as 0.5nm; The next layer, termed 1L, is a new polymorph, in which the molecules form herringbone stacking; The next (2L) and subsequent layers are structurally consistent with herringbone structure commonly in pentacene thin films.

Table 4-1 Experimental lattice parameters of pentacene bulk, thin film, 1L, 2L and WL motifs.
Structural data of 1L, 2L and WL is from ref¹¹⁸

Lattice parameters	bulk phase	thin film phase ^a	1L	2L	WL	hBN
a(Å)	6.3	6.0	6.23 ±0.07	5.98 ±0.09	8.9	2.46
b(Å)	7.8	7.6	7.77 ±0.08	7.61 ±0.13	16.3	2.46
c(Å)	14.5	15.6	14.2 ^b	12.9 ^b		6.70
α(deg)	76.7	81.2	82	61		90.0
β(deg)	87.5	86.6	91	88.25 ±1.22		90.0
γ(deg)	84.6	89.8			60	120.0
crystal system	triclinic	triclinic	-	-	-	hexagonal

^a CCDC code is PENCEN10, ref¹¹⁹

^b The number is the vertical distances of the molecular skeleton rather than lattice parameters c

Compared to bulk phase, pentacene thin film phase (2L) have similar unit cell parameters, as Table 4-1 shows, but molecules in thin film are more upright (87° to herringbone layer) than that in bulk (68° to herringbone layer). 2L and subsequent layers have upright configuration because interlayer interaction is weak, especially being far from BN layer. Differently, in the wetting layer, strong interaction forces drive pentacene molecules to lay flat on the surface with the long molecular axis pointing along BN [1 1 $\bar{2}$]. The most interesting but not unsurprising phenomenon is that 1L, a new polymorph, is a transition between WL and 2L thin film phase. The molecule in 1L tilt mainly along b axis to optimize interlayer and intralayer interactions. The tilting angles are 61° and 82° for the 1L and 2L molecules with respect to the b-axis; while they are close to 90° with respect to the a-axis, see Figure 4-2(a)(b). Further leaning of the molecule in 2L along b introduces more repulsion between molecules and leads to their reorientation, the plane of the molecules further

parallel to the a axis, see Figure 4-2 (c). Thus, in 1L, the unit cell has longer distance along a axis than that in 2L. Experimental lattice parameters of pentacene bulk, thin film 2L, 1L and WL polymorph are summarized in Table 4-1.

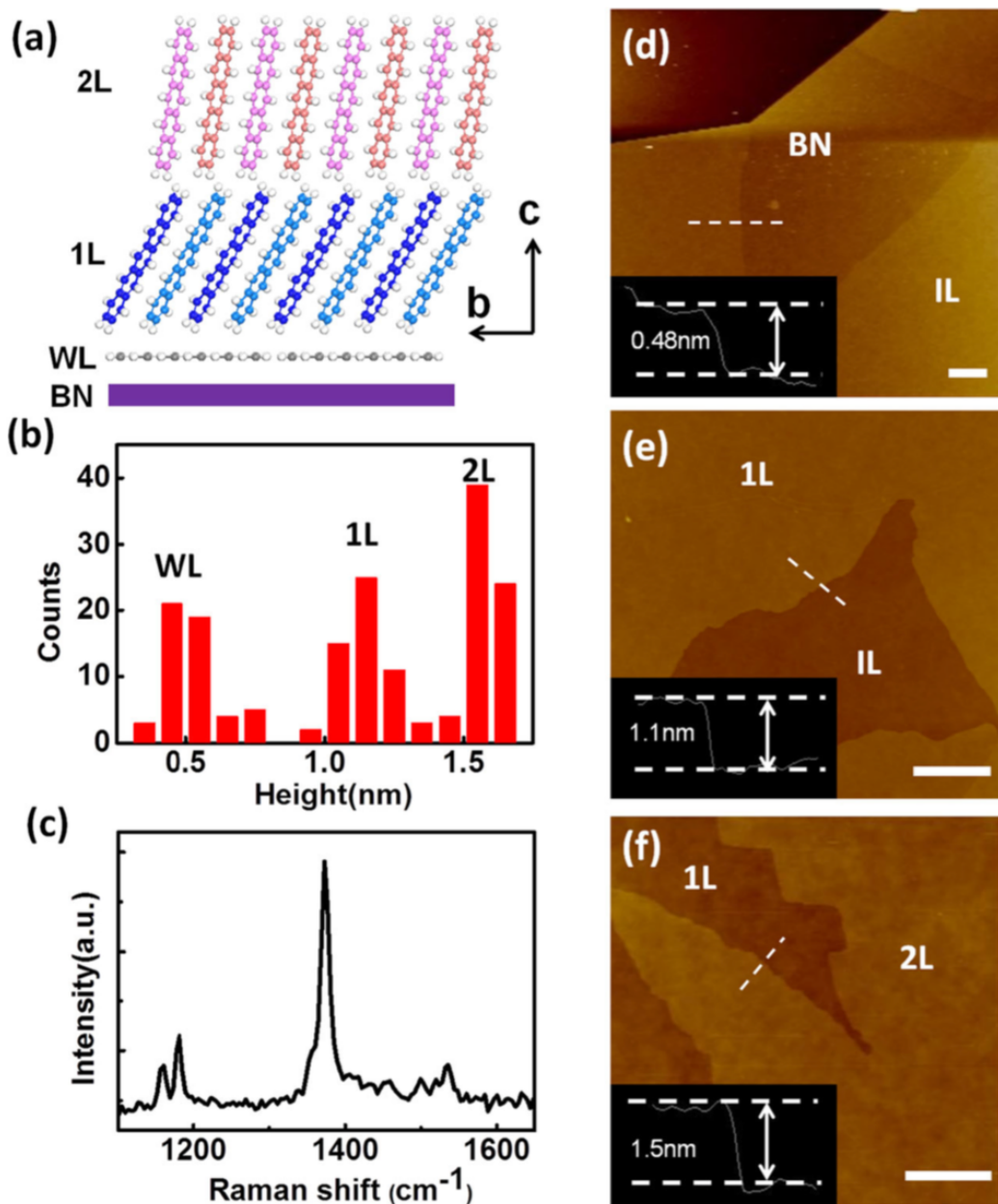


Figure 4-1 Epitaxial growth of 2D pentacene crystals on BN. **(a)** Schematic illustration of the molecular packing of WL, 1L, and 2L within b - c plane. **(b)** Histogram distribution of the thickness of WL, 1L, and 2L, each taken from over 10 samples. **(c)** Raman spectrum of the pentacene crystals on BN, taken from a 2L sample. **(d)-(f)** AFM images of WL, 1L, and 2L pentacene crystals on BN, showing height measurements.

respectively. The layer numbers are marked on each image. Insets show the height profiles along the dashed lines. The scale bars are $2 \mu\text{m}$. The plots from ref¹¹⁸

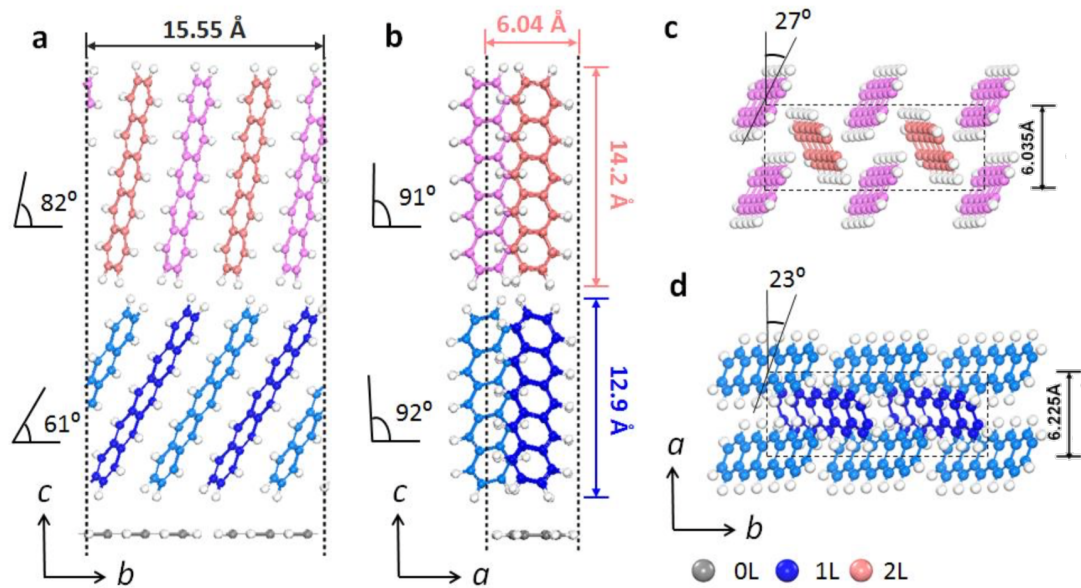


Figure 4-2 Molecular packing of 1L (lower panel in blue) and 2L (upper panel in pink) pentacene within (a) b-c plane (b) a-c plane (c-d) a-b plane. The plots from ref¹¹⁸

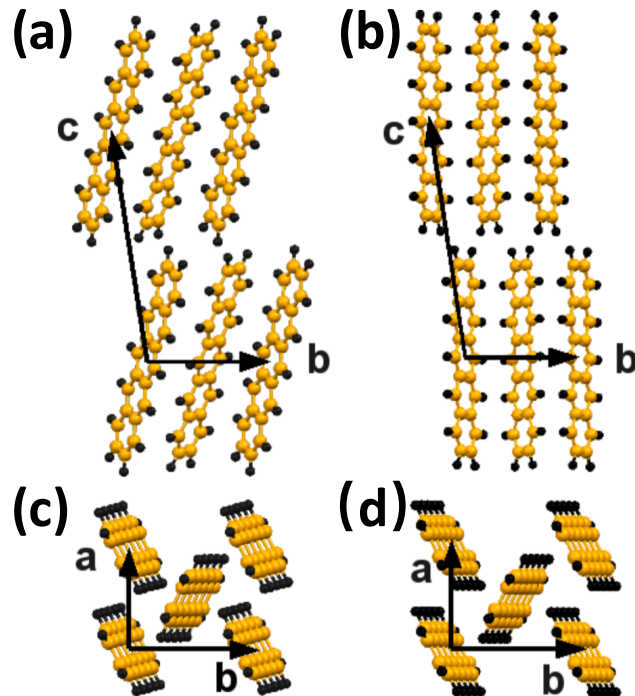


Figure 4-3 illustration of unit cell for (a) (c) bulk and (b) (d) thin film. a,b,c are lattice parameters. (a)(b) are b-c plane and (c)(d) are a-b plane. The herringbone angle is $\sim 54^\circ$.

4.2 Set up of simulations

4.2.1 Periodic box size for thin film model

To build the model of hybrid structure and keep it as simple as possible for the reason of computational efficiency, the strategy is to find the lowest common multiple of the unit cell parameters along the a and b axis for BN substrate, WL, 1L (and 2L) shown in Table 4-1 as periodic supercell, as well as to keep the mismatch of difference layers as small as possible. With this mismatch calculations, the periodic supercell of BN+WL+1L(+2L) consists of 69*24 BN unit cells, 11*9 WL unit cells, 22*10 1L unit cells (and 22*10 2L unit cells). There are two BN layers with the considerations of interlayer vdW interaction. In total, the 2L supercell includes ~50000 atoms. The molecular model for 1L and 2L supercell has a mismatch of less than 3%. The size of the periodic cell is schematically illustrated in Figure 4-4 (side view) and Figure 4-5 (top view).

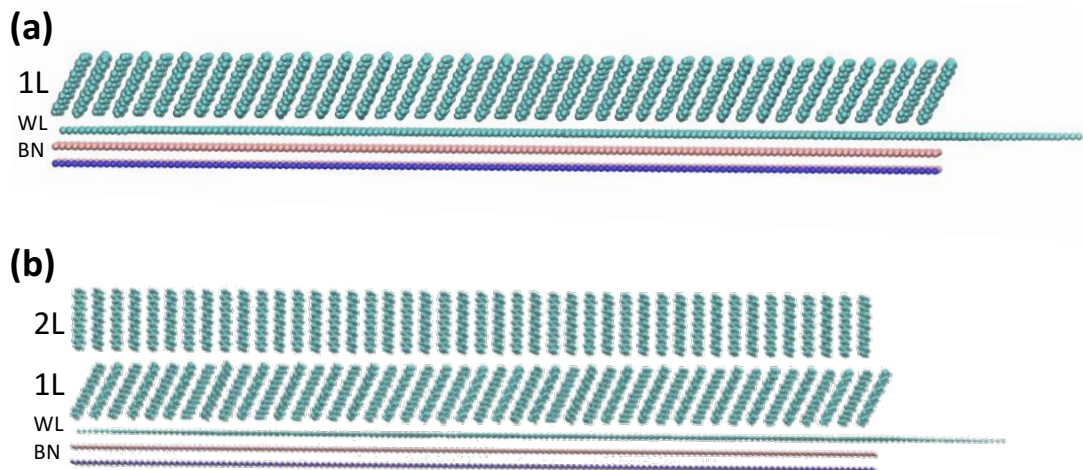


Figure 4-4 The side view of periodic cell for (a) 1L model (b) 2L models.

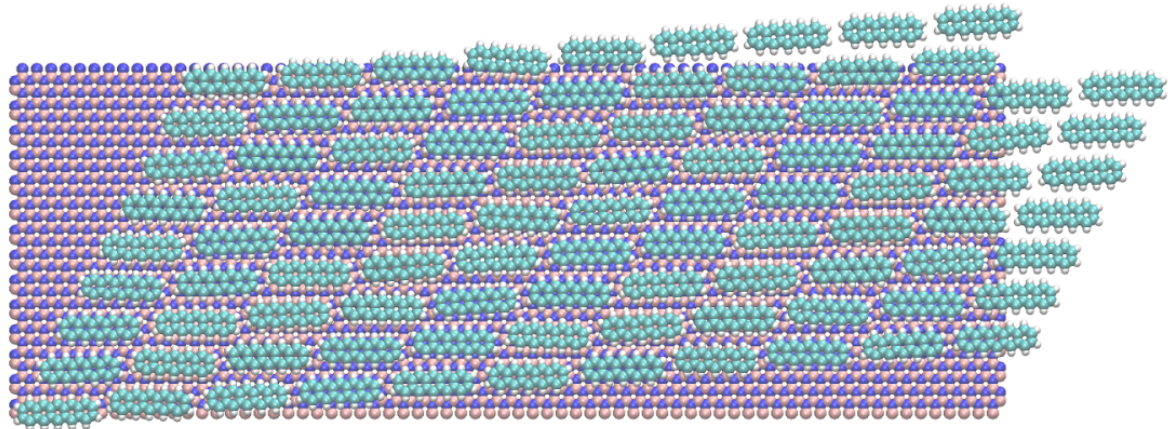


Figure 4-5 The top view of periodic cell for WL pentacene on the BN substrates.

4.2.2 Structure and force field for pentacene layer on BN

Structure model of pentacene layer WL on the substrate hBN

WL suggests that the molecules adopt the face-on configuration similar to that of pentacene on graphite¹²⁰ and on metal¹²¹. Following growth procedure in experiment and bottom up processing, the structure model was built firstly from wetting layer of pentacene on hexagonal boron-nitride (hBN). The hBN has a geometry similar to graphite, which is schematically illustrated in Figure 4-6. Both of them have covalent bonds of length 1.44 Å and intra-layer distance of 3.3 Å.

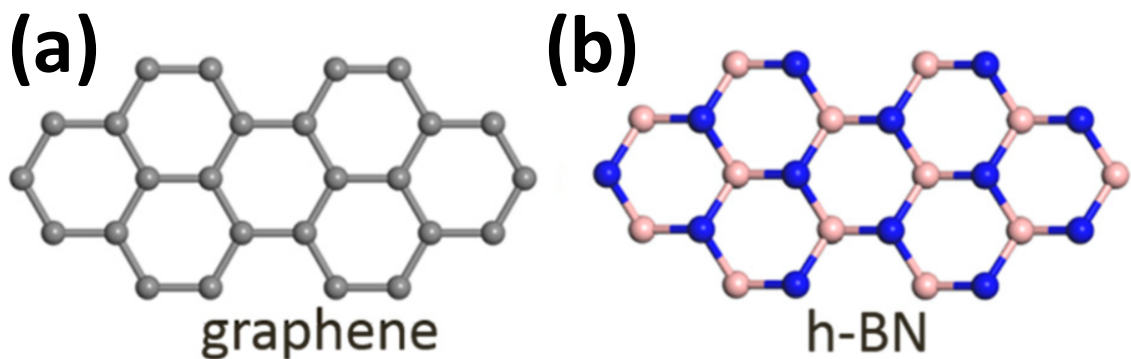


Figure 4-6 Similarity of geometry for (a)graphite and (b)hexagonal boron-nitride. Grey, red and blue balls represent C, B and N atoms, respectively

Currently, there is no literature reporting accurate experimental favorable configuration of pentacene on hBN. But, the molecular packing in wetting layer can be analogous to that on graphite due to their similarity in geometry. The only difference is the intralayer bonds. The former has highly polar B-N bonds, whereas the latter has non-polar homonuclear C-C bonds. STM images for lying-down pentacene monolayer on graphite and schematic drawing of the pentacene on graphite are shown in Figure 4-7. On the other hand, some researchers have predicted that this configurable analogy in adsorption structures is correct based on FF and DFT calculations.^{118 122}

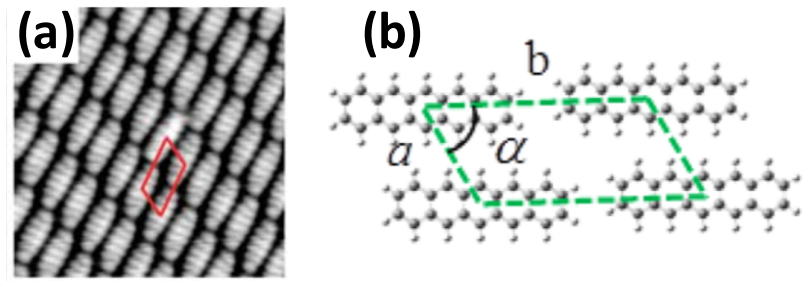


Figure 4-7 (a) STM images for lying-down pentacene monolayer on graphite. (b) Schematic drawing of unit cell of lying-down pentacene monolayer on graphite. Lattice parameters are from ref¹²³: $a=8.9\pm0.5$ Å, $b=16.3\pm0.5$ Å, $\alpha=60^\circ\pm2^\circ$

Force field of hBN

As there are no available parameters for hBN substrate in standard AMBER force field, I use here the force field parameters from Zhao's work,¹²⁴ in which the parameters of BN are fitted to reproduce the DFT results (see Figure 4-8c). By analyzing the fitted results, The force field parameters are $\sigma_B = 0.325$ nm, $\varepsilon_B = 2.32$ kJ/mol, $\sigma_N = 0.325$ nm, $\varepsilon_N = 7.11$ kJ/mol. Some researchers also carried out DFT calculations to show the adsorption distance is 3.27 Å and the most energetically favorable configuration of WL pentacene molecules on BN is schematically illustrated in Figure 4-8(a). I tested those FF parameters by scanning the distance of a single pentacene between BN, and obtained the same potential as Zhao. He also states in the paper that the AMBER force field can provide a good description of the pentacene-pentacene interaction on BN substrate.

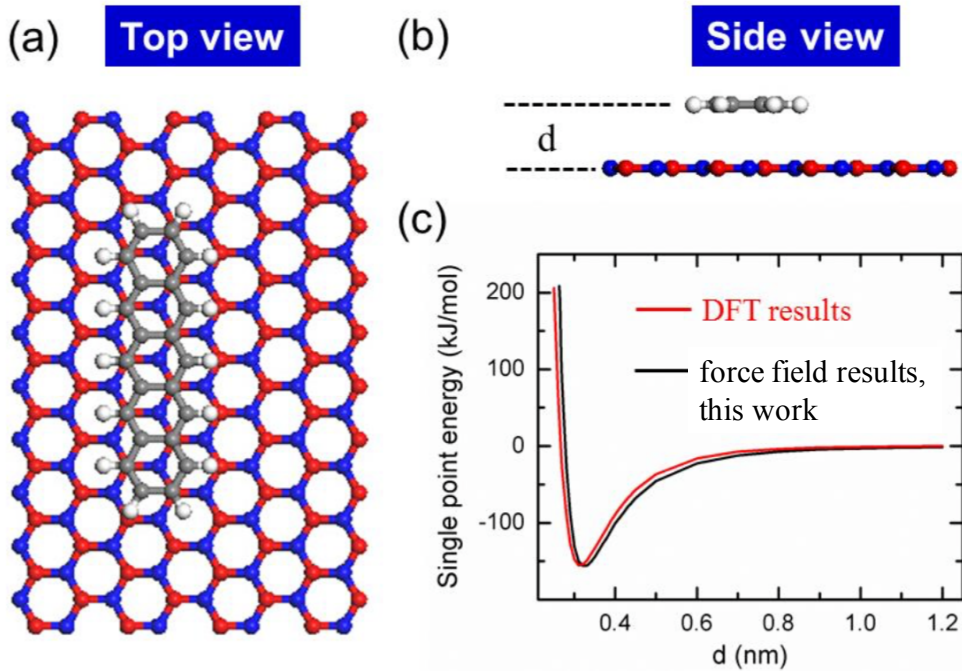


Figure 4-8 Generation of force field of hBN. (a,b) Top view and side view of pentacene on hBN. (c) parameterized FF to reproduce DFT potential of scanning the distance d in (b). Data from ref ¹²⁵.

In classical FF calculations, B and N atoms are fixed to the equilibrium positions to make the simulation cheap (only non-bond interaction are taken into consideration between pentacene molecules and BN substrate). Figure 4-5 shows top view of periodic cell for WL pentacene on the BN substrate. My simulations show that WL layer are stable with the determined force field and even with thermal fluctuations in MD.

4.2.3 Restraining pentacene layers with collective variables

In the previous section, the experimental thin film has been reproduced by my structural model successfully and it is good enough to investigate static properties of

charge transport in this thin film system. However, it would be better to take thermal stability into account for more elaborate simulation.

Unfortunately, the current force field could not reproduce tilt angle differences in the different thin film layers due to some remaining inaccuracies. As shown in Figure 4-9, the initial pentacene molecules have the same tilt angle as in experiment, but when minimizing the energy, the tilt angle of 1L changes from 61° to 65° along a (or “y axis”), from 92° to 101° along b (or “x axis”), and the one for 2L changes largely from 82° to 65° along a, from 91° to 101° along b.

To eliminate size effect as a possible cause for this artefact, the periodic cell was tripled along a axis to reduce the mismatch from 3% down to less than 1%. But, the results show the minimized structure still does not reproduce the experimental tilt angles for 1L and 2L. Thus, lacking accurate force field is the most likely reason to not reproducing the designated tilt angles.

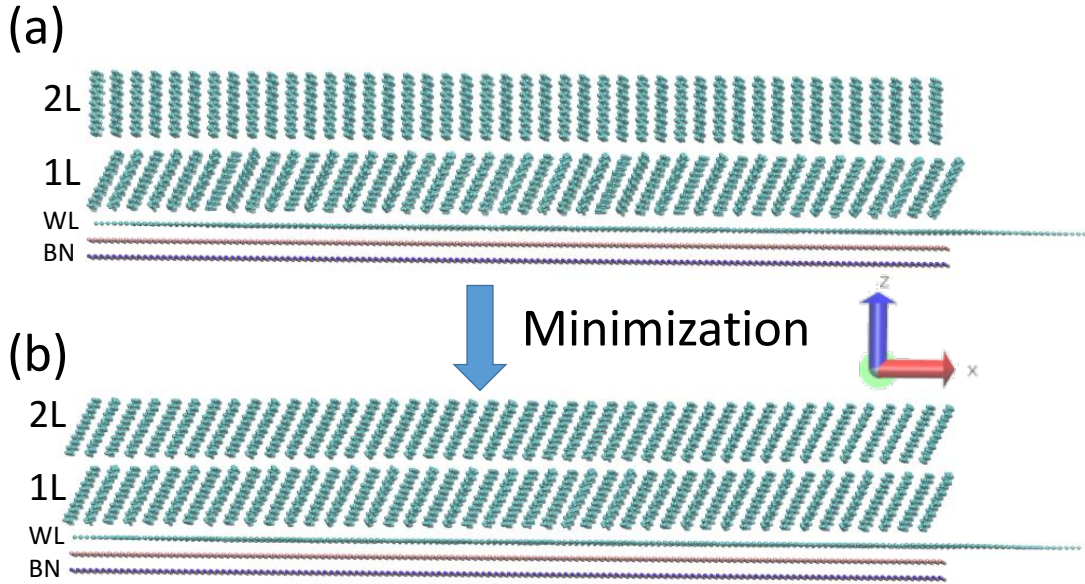


Figure 4-9 The side view of periodic cell for double-layer pentacene system. **(a)** initial motif built based on experiment geometry **(b)** structure after minimization using current force field.

To solve this issue, restraining potentials are used to restrain the tilt angles of each molecule in 1L and 2L to the experimental value. To be specific, I declared and used collective variables (short for colvars), distanceZ (projection of a distance vector on an axis) in NAMD. The cost of MD simulation of 2L model is 14hrs/ns with 12 cores and 8% overhead for the colvars.

Restraint force constants have been tested for different values, 0.5, 1.0, 2.0 and 4.0 kcal/mol/ \AA^2 . The details are shown in Table 4-2 and Figure 4-10. The larger the constants, the closer the distribution of tilt angles to the experiment. But restrain force constant of 4.0 is too strong to keep molecule planar. Thus, a value of 2.0 was chosen for the following energy minimization and MD simulation. The lattice constants are in good agreement with experimental values within 1.5%.

Table 4-2 Relation of restrain force constant for colvars and tilt angle pentacene.

Restrain force constant (kcal/mol/ Å^2)	2L tilt angle along x (deg)	2L tilt angle along y (deg)	1L tilt angle along x (deg)	1L tilt angle along y (deg)
0.0	67.1	100.8	66.0	100.5
0.5	71.8	84.7	63.5	86.7
1.0	77.3	85.2	63.1	87.4
2.0	79.9	86.0	62.6	87.8
2.0 (minimization)	81.4	87.1	61.7	88.1
experiment	82.0	91.0	61.0	92.0

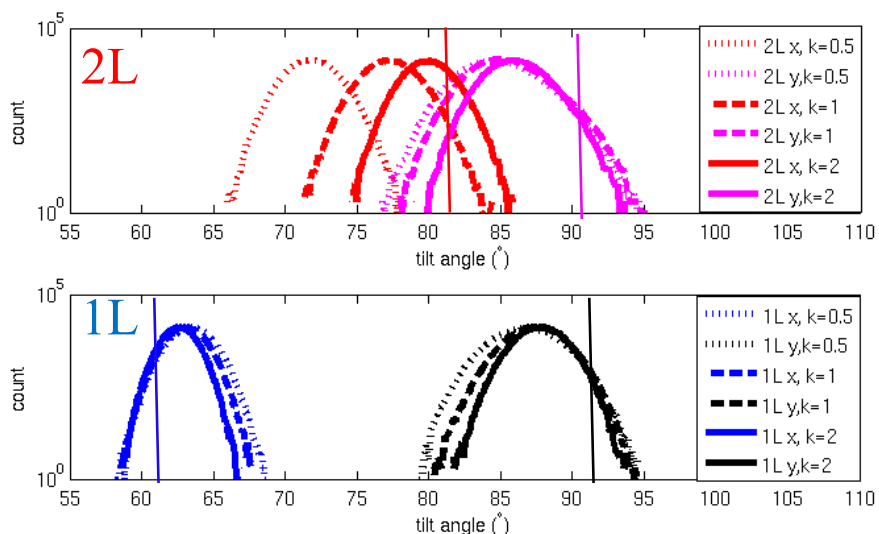


Figure 4-10 Restrain force constant for colvars v.s. tilt angle distribution of pentacene in 2L (top) and in 1L (bottom) in 1ns long NVT MD. Colour code, red, pink, blue and black are represented tilt angle of 2L molecule along x axis, along y axis, 1L molecule along x axis, along y axis, respectively. Dot, dash, solid curves are obtained with restrain force constant of 0.5, 1, and 2 kcal/mol/ Å^2 , respectively. Vertical solid line shows the respective experimental tilt angles.

4.3 Results and discussion

4.3.1 Intralayer and interlayer electronic couplings

Within herringbone layer 1L, H_{ij} are 28.0 meV, 9.5meV and 1.0meV for dimer pairs

t_a , t_1 and t_2 , which are inversely correlated with the inter-molecular distances of 5.0 Å,

6.3 Å, and 7.9 Å. The pair t_a with the largest electronic coupling indicates that the $[1/2, \pm 1/2]$ direction is the most likely direction for current flow. t_a and t_1 pairs within 2L have the same intermolecular distance and similar orientation configuration, while their coupling values are 25-89% larger than that in 1L due to more constructive orbital overlap.

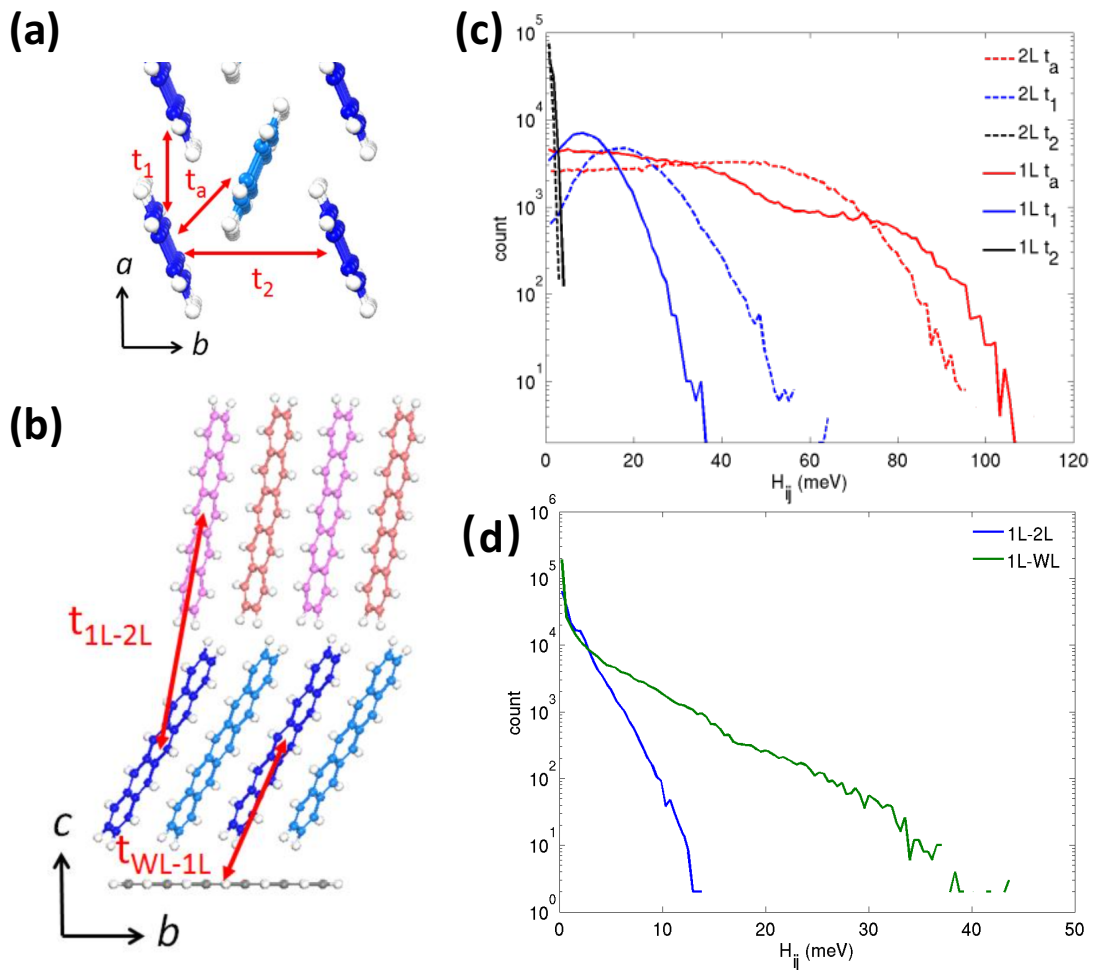


Figure 4-11 (a-b) Orientation of nearest neighbour intralayer pairs t_1 , t_2 , t_a (a) and interlayer pairs t_{1L-2L} and t_{WL-1L} (b). **(c-d)** Distribution of electronic coupling matrix elements $|H_{ij}|$ for hole transfer between nearest neighbor pairs within herringbone layer (c) and across herringbone layer (d).

t_{WL-1L} has a range of values, corresponding to different dimer pairs between WL and 1L. t_{WL-1L} is comparable to the intralayer counterparts in 1L, suggesting strong WL-

1L electronic coupling. The transfer integral between 1L and WL has a similar magnitude to that between the adjacent 1L molecules. Thus, carriers can easily hop from 1L to WL. Due to the lack of π - π stacking in WL, the carriers can be further localized. While the transport in 2L is nearly unperturbed from 1L, ascribed to the much smaller transfer integrals between them.

Table 4-3 Comparison of electronic coupling values for the similar orientational configurations of single crystal, thin film and amorphous pentacene. T₁, T₂ and P pairs are in the bulk. t_a, t₁ and t₂ pairs are in the thin film. The values in brackets are the corresponding center-to-center distance.

	Bulk (100K)	TF 1L (110K)	TF 2L (110K)	Amorphous (100K/300K)
T ₁ / t _a	76.6 (4.8 Å)	28.0 (5.0 Å)	35.0 (5.0 Å)	
T ₂	43.2 (5.2 Å)			
P / t ₁	18.4 (6.3 Å)	9.5 (6.3 Å)	18.0 (6.3 Å)	
t ₂		1.0 (7.9 Å)	0.5 (7.9 Å)	
Amorphous				24 (3-7 Å)

The electronic couplings of the nearest neighbours in the thin film pentacene are compared with that with similar geometry in the bulk, see Table 4-3. Both the T₁ pair in the bulk and the t_a pair in thin films form a T-shape in each system with the same herringbone angle of 54°. The T₁ pair is more than 2 times stronger coupled than t_a pair because the exponentially decay of the coupling with increasing intermolecular distance. On the other hand, the P pair in the single crystal and the t₁ pair in TF 2L have the same coupling values. The t₁ pair in TF 1L also have the same intermolecular

distance but the coupling is $\frac{1}{2}$ smaller. The weaker orbital overlap of the t_1 pair results from the fact of the reinforce tilting angle of 1L making the molecules reorient their shorter axis closer the a-axis (23° in 1L compared with 27° in 2L in Figure 4-2 c-d).

4.3.2 Charge carrier hopping

A charge carrier is initialized at an arbitrary molecular site in a KMC trajectory and the initial position follows a discrete uniform distribution. Thus, the probability of which layer the charge starts from is proportional to the number of pentacene molecules in that layer in the simulation box. There are 95, 440, and 440 molecules in WL, 1L, and 2L, respectively.

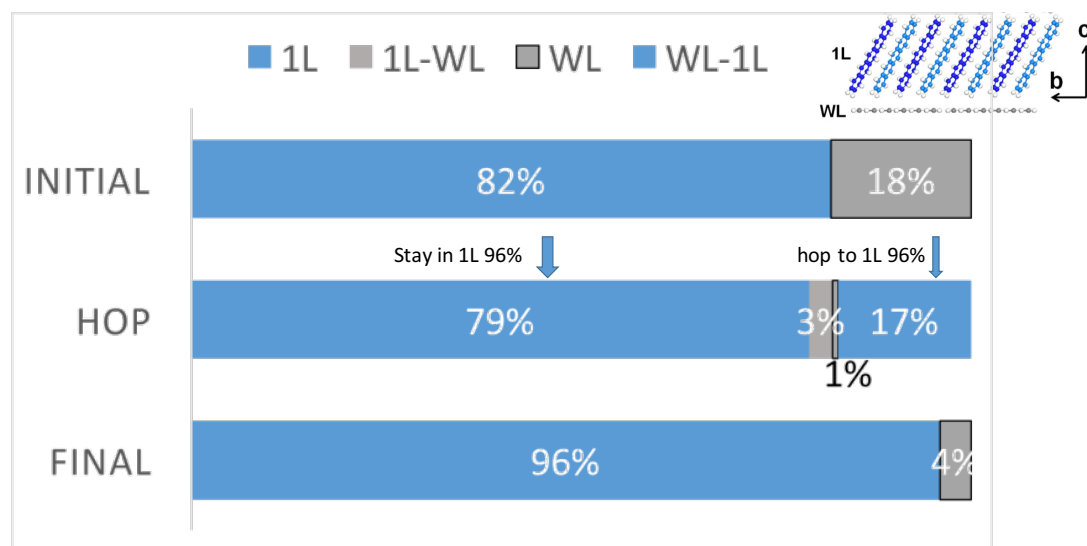


Figure 4-12 Dynamic distribution of the holes before and after hopping for WL+1L system.

Thus, Figure 4-12 shows that in the case of WL+1L model (Figure 4-4 a), a charge carrier has the probability of 82% initialized in 1L and 18% in WL. For the former, the electron will stay in 1L with the probability of 96% or will hop down to WL with

the probability of 4%; while for the latter, the electron will most likely hop up to 1L by 96% and less likely will stay in WL by 4%. Because the coupling between nearest neighbors within WL (the mean is 7 meV and the max is 12 meV) is much lower than interlayer couplings between WL and 1L (the max is 44 meV). As a result, the electron will end up in 1L with the probability as high as 96% after KMC hop.

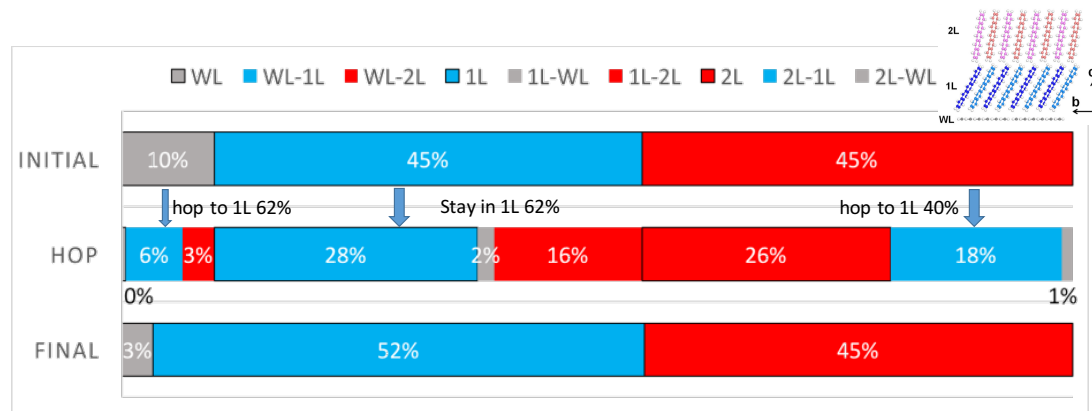


Figure 4-13 Dynamic distribution of the holes before and after hops for WL+1L+2L system.

In WL+1L+2L model (single snapshot) in Figure 4-4 b, an electron is initialized with a probability of 10% in WL (4% stay in WL, 62% finalize 1L, 34% finalize in 2L), 45% in 1L (62% stay in 1L, 4% finalize down to WL, 35% finalize up to 2L), and 45% in 2L (58% stay in 2L, 40% finalize down to 1L, 2% finalize in WL). It is worth noticing that an electron initializes from 1L or 2L with the same rate, while the electron is more likely to end up in 1L than 2L by 7%.

To study the impact of dynamic disorder, a probability analysis is carried out on 100 snapshots taken from MD. The results show that all the rates are similar to the one obtained for a single snapshot above, which means the statistical error is small and

dynamic disorder has little impact on electron propagation. According to the data, we can see that a charge carrier is more likely end up in 1L for both models.

4.3.3 Charge mobility

The mobility of WL+1L model within herringbone layer is as low as $2.9 \text{ cm}^2/(\text{Vs})$ at 110K. This is the temperature of the thin film structure being characterized. WL+1L+2L system has slightly higher mobilities due to the less tilted molecular packing in 2L leading to stronger couplings between adjacent molecules. Overall, pentacene thin films have significantly smaller mobilities than a single crystal.

Table 4-4 Comparison of computed mobilities of TF and single crystal from current work with experimental mobilities from the literature at 110K^a

	TF 1L	TF 1L+2L	single crystal
μ from current work	2.9	5.2	14.0
experimental μ from literature	< 1 ^b	2.9-4.0 ^b	

^a The structural characterization of the thin film is done at 110K. All values are given in $\text{cm}^2/(\text{Vs})$.

^b FET mobilities from ref¹¹⁸

4.4 Summary

In this work, I set up the models of few-layer crystalline pentacene thin films based on the experimental structure of FET device. Using a bottom-up approach, the structural model is comprised of hexagonal boron-nitride, wetting layer of pentacene, 1L with a new polymorph and/or 2L with the common thin film polymorph. Despite of the limited experimental measurements and observations, in particular the lack of

information on the stacking of WL on the BN layer, I have successfully modelled the microstructure of these multi-layer structures.

Electronic transport parameters and charge mobilities within and across layers have been computed with the same computational approaches. The T-shaped pairs have the strongest couplings in thin film pentacene for both the model of WL+1L and the model of WL+1L+2L, similarly as in the case in the single crystal presented in Chapter 3. In the former two systems, the coupling values are roughly half of those in the latter due to larger intermolecular distances. Thus, the mobilities of thin films are significantly smaller than that in the bulk. Furthermore, the interlayer electronic couplings between WL and 1L is on the same order of magnitude as intralayer couplings, while couplings between 1L and 2L are ignorable. Thus, transport within 1L is affected by WL but transport within 2L is nearly unperturbed by 1L.

5 Pentacene Amorphous Solid

In the previous two chapters, I discussed charge transport in the highly ordered single crystalline organics and in the few-layer crystalline pentacene thin films. In this chapter, the application of polaron hopping model will be expanded to amorphous organic molecular materials, which are in more common use than single crystals as they can be much more easily fabricated. In order to compare charge transport parameters and mobilities for distinct morphologies, the same molecule, pentacene, is used to study. Structures of amorphous pentacene will be generated by simulated annealing, i.e. melting of a crystal at high temperature followed by cooling to room temperature at different cooling rates. The structural characterizations include the cooling-rate effects on material volumes and morphologies, radial distribution functions and angle distributions for all the molecular pairs. The thermal distribution of electronic couplings and mobilities for the amorphous samples are presented, and are further compared with that in the ordered materials discussed in Chapter 3 and Chapter 4.

5.1 Amorphous materials and controlling of the growth

Charge transport in amorphous organic materials is of much interest because most OSs in real devices are amorphous instead of crystalline,¹²⁶ even though recent studies on amorphous molecular materials have revealed that they exhibit lower mobility (10^{-}

4 to $1 \text{ cm}^2 \text{ V}^{-1} \text{ s}^{-1}$) compared with the organic crystals. An amorphous film is known to be formed when an organic material is vapor-deposited onto a substrate maintained at low temperature and fast deposition rate in vacuum. X-ray is one of the most common used techniques to characterize the morphology. The density is also an indicator due to its loose packing. However, the fabrication process is complicated and the molecular packing of amorphous solid is difficult to observe experimentally.

It has generally been accepted that charge transport in organic disordered systems with small intermolecular electronic couplings takes place by a hopping process. Molecular simulations are often used to help understand the structure of amorphous materials and possibly reveal their charge transport properties.

Different from thermally stable organic single crystal, the thin film phase is a metastable polymorph and it is more sensitive to the deposition process. Different thermal deposition parameters and substrate properties might lead to different organics structures resulting in different properties. Therefore, to improve the charge carrier transport properties, rational control of the processing conditions for enhancing intermolecular interactions and maximizing electron orbital overlap is crucial for further improvement of charge carrier mobility in OSs.

The vapor deposition process is usually used for small organic molecules. Deposition rate and substrate temperature are two important parameters widely used to control the film growth mode as well as the solid microstructures. It is generally accepted that

low deposition rate and high substrate temperature are preferred to achieve large crystalline domains, leading to efficient charge carrier transport and high carrier mobility.^{127,128} For example, the diffraction and XRD spectra in Figure 5-1 show that the pentacene crystalline quality degrades with the decrease of temperature and increase of deposition rate. From the dynamic point of view, at higher substrate temperature, the deposited molecules have sufficient energy to overcome substrate interactions and thereby prefer to stand on the substrate (edge-on orientation) and make it possible to self-assemble into large domains, while lower deposition rate provides enough time for the molecules to rearrange themselves and form packing structures with high order.¹²⁷

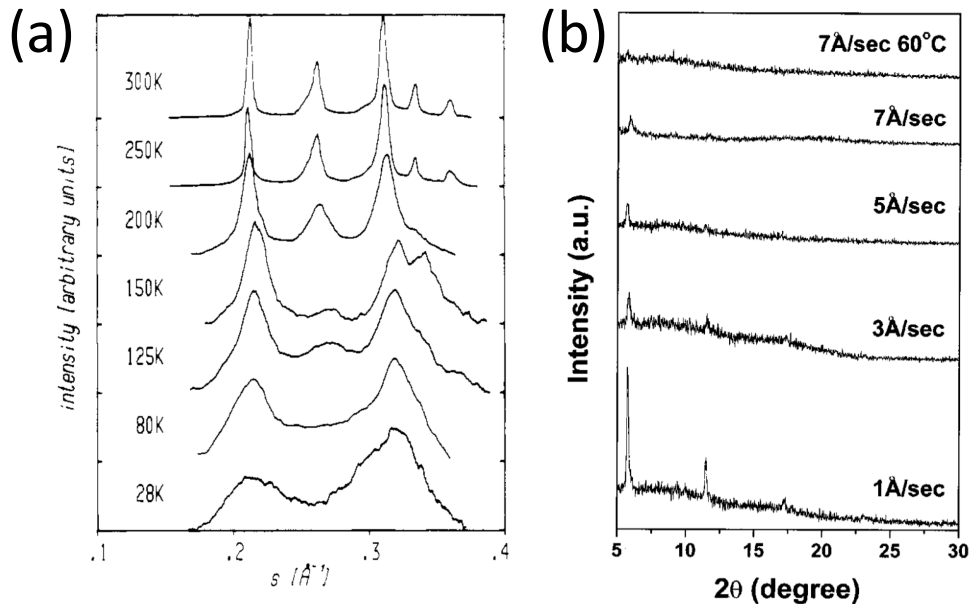


Figure 5-1 (a) Diffraction spectra for as-grown pentacene films. the film-formation temperature ranges from 28K to 300K. (b) XRD spectra of the pentacene films fabricated by evaporating at rates of 1, 3, 5, and 7 $\text{\AA}/\text{s}$ at 25 °C room temperature, and 7 $\text{\AA}/\text{s}$ at 60 °C. The data are from ref ¹²⁷ and ref ¹²⁸, respectively. In general, the crystalline quality degrades with the decrease of temperature and the increase of deposition rate.

5.2 Disorder morphologies - structural modelling

In a recent computational study, Jenny Nelson and co-workers¹²⁹ generated the disordered C₆₀ thin films simulated directly physical vapour deposition (PVD) process over a range of substrate temperatures. In their work, individual C₆₀ molecules are released one at a time from the source at a random position above the substrate at a given temperature and molecules are moved consecutively by one Monte Carlo step at a time.

In this work, I generate amorphous structures using molecular dynamic simulations. Although it does not strictly model the growth process, this method allows me to generate larger systems in a relatively short time. The disordered organic systems are generated by melting crystalline pentacene and cooling them down to room temperature over a range of cooling rates. The final equilibrium structures driven by intermolecular interactions during cooling and annealing process are compared and their mobilities are evaluated.

5.2.1 Set up of quenching process

Disordered pentacene systems are generated in classical MD simulations by melting crystalline pentacene at 800K and then quenching to room temperature. The periodic supercell contains 20*20*3 unit cells, i.e. 2400 molecules. The neutral charge state of the molecules is modeled with the generalized Amber force field (GAFF)¹³⁰. The MD simulations are performed with the NAMD program package.⁹²

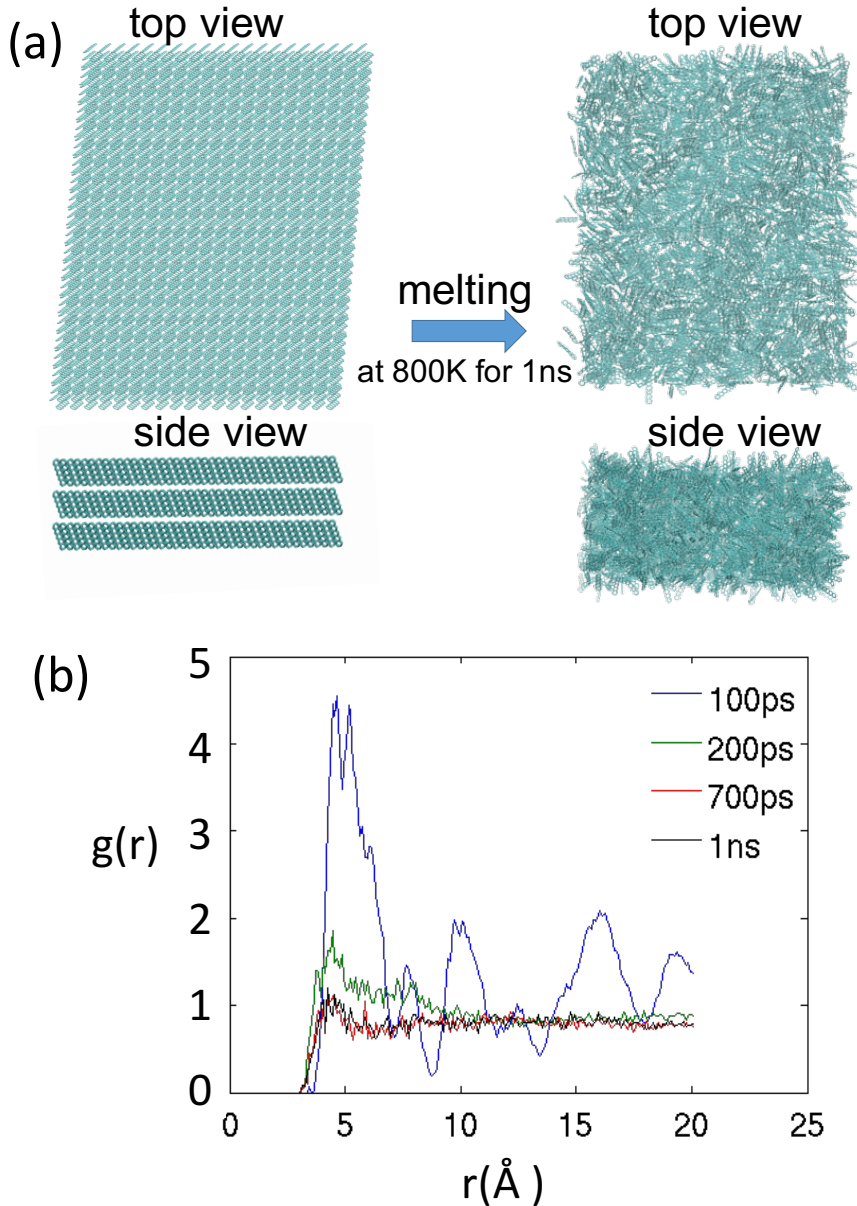


Figure 5-2 (a) Snapshots of crystalline pentacene melting to amorphous phase at 800 K in the MD simulation. (b) The radial distribution functions $g(r)$ of the center of mass of molecules when the MD simulations last 100, 200, 700, and 1000 ps. The peaks of $g(r)$ degrade gradually as the simulation lasts and converge after 700 ps, which is an indicator of generating an amorphous solid.

First, the initial crystalline structure of the MD simulation melts to a complete liquid within a NVT ensemble MD under 800 K for 1 ns (see Figure 5-2). The peaks in $g(r)$ gradually degrade into a broad peak after 200 ps in panel b, and figures of 700 ps and 1 ns nearly overlay, which means the system has reached equilibrium before the

simulation lasting 700ps. Second, the melting simulations are followed by four quenching simulations from 800 K to 300 K in a NPT ensemble on the distinct time scales of 10ns, 1ns, 100ps and 10ps, respectively, see Figure 5-3 a and b. Here, a Nose–Hoover thermostat and barostat are used. Several configurations of arbitrary snapshots from the end of the melting simulations have been used as starting structures for quenching simulations in order to minimize the probability of the system relaxing into a local minima of the potential energy surfaces. Third, after quenching, the systems of MD simulations further relax within a NPT ensemble for several nanoseconds at a fixed temperature of 300 K. During the NPT simulations, the simulation cell shrank and finally reached a constant volume, see Figure 5-3 c and d. I note that although the current protocol covers 4 orders of magnitudes of quenching times, they are still several orders of magnitudes faster than in experiment.

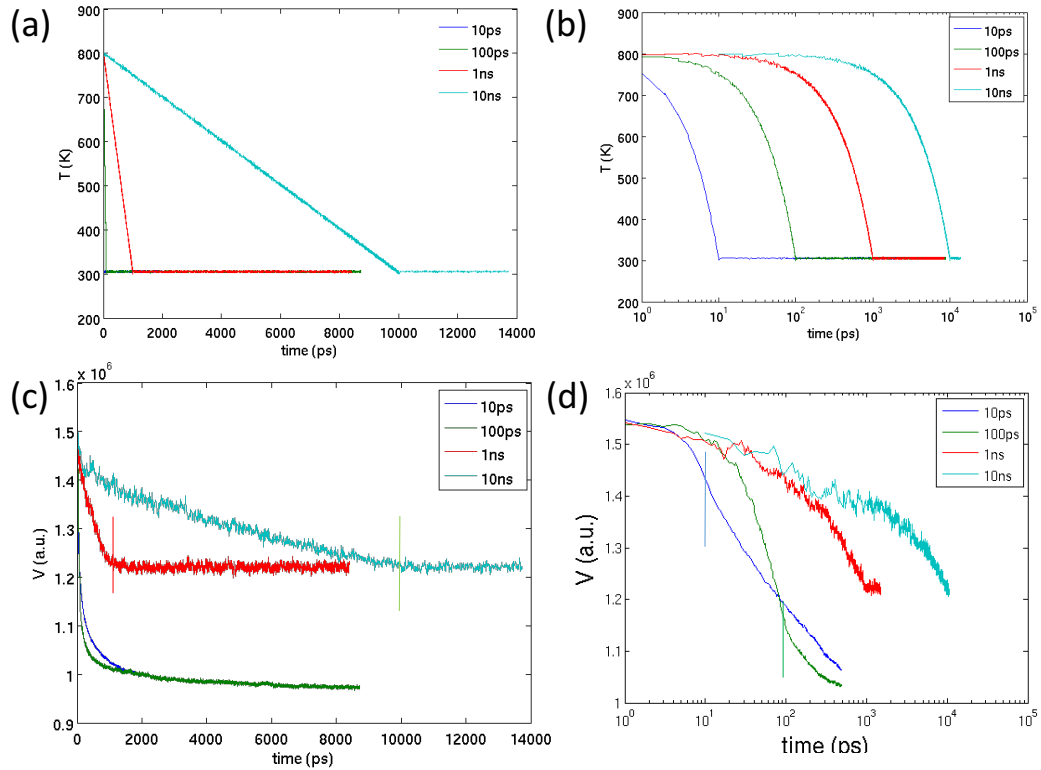


Figure 5-3 (a-b) Quenching simulations for melted pentacene from 800 K to 300 K in a NPT ensemble in the distinct time scales of 10ns, 1ns, 100ps and 10ps, respectively. **(c-d)** During the NPT simulations, the simulation cell shrank and finally reached a constant volume. (b) and (d) are in log scale. The vertical lines show the moment of halting the cooling.

5.2.2 Structures – How amorphous are the disorder systems?

The density of the disordered system depends on the cooling rate. The quenching simulations last a range of time scales: 10ps, 100ps, 1ns, and 10ns. As shown in Figure 5-3 c, the material systems can be divided into two categories: the former two systems shrank to the same size of density (referred to as “fast cooling” or “low density”), which is 22% larger than the latter two systems (referred to as “slow cooling” or “high density”).

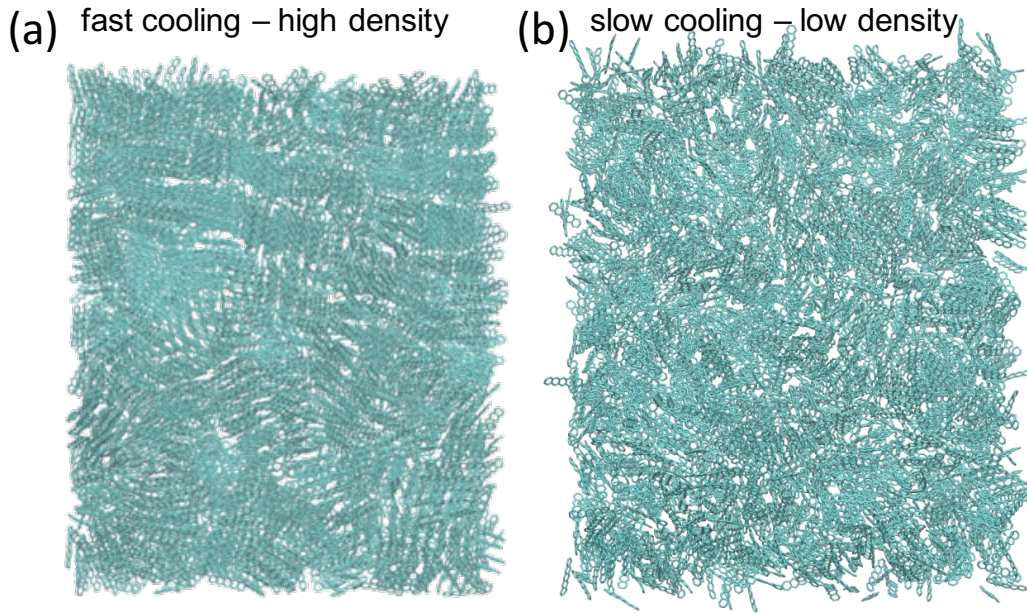


Figure 5-4 Schematic diagram of disordered pentacene obtained after quenching process. **(a)** High density system after fast cooling includes many (shift) cofacial configurations due to molecule self-assembling. **(b)** Low density system after slow cooling is amorphous.

How amorphous are the structures? Schematic diagram of these two systems are shown in Figure 5-4. From panel (a) for the high density system, we can see by eye many (shift) cofacial pairs; In the contrast, in panel (b), the low density system is very amorphous with all the molecules randomly distributed and oriented. Next, I will introduce the quantitative investigations by analyzing the densities, radial distribution functions, and distributions of angles between molecular pairs.

Densities

These disordered solids have densities of 1.11 and 0.91 g/cm³ for the materials cooling fast and slow, respectively. They compare with a density of 1.30 g/cm³ for crystalline pentacene experimentally and 0.88 g/cm³ for melted pentacene in my simulations. The

ratio between melted and crystalline states is 0.68, close to the work of NaokiSato et al.,¹³¹ who find that this ratio for pentacene is ~0.75, and between 0.78 to 0.87 for anthracene, naphthalene and benzene. The ratios between the density of two disordered systems and crystalline pentacene are 0.85 and 0.70, respectively. It indicates that the high and low density amorphous solids generated in this work are midway between the crystal and the liquid, and the latter one is nearly complete amorphous phase.

In Figure 5-3 d, it is interesting to see the former two systems are still turning to be more condensed when the temperature stops dropping and keeps constant at 300 K, which is different for the latter systems. It suggests that in the cases of fast cooling, the molecules have not enough time to reorganize themselves completely to adapt the rapidly changing environment, so that they have to reorganized themselves when the temperature remains constant. During the latter process at room temperature, the molecules assemble themselves to favorable configurations, thus form the polycrystalline phase. Differently, in the cases of slow cooling, the rate of temperature change is slow enough to let the systems reach equilibrium at each T change.

Radial distribution functions

The radial distribution function is another indicator for the packing in materials. In Figure 5-5, different from peaked distribution in the case of a single crystalline pentacene, a broad peak appears in the distribution curve and followed by a long and

smooth tail in the case of melted phase as well as in the case of the low density phase.

It reflects loose packing in amorphous materials. By contrast, the high density phase has two higher peaks in the distribution, which can be interpreted as the 1st and 2nd neighboring molecules respectively.

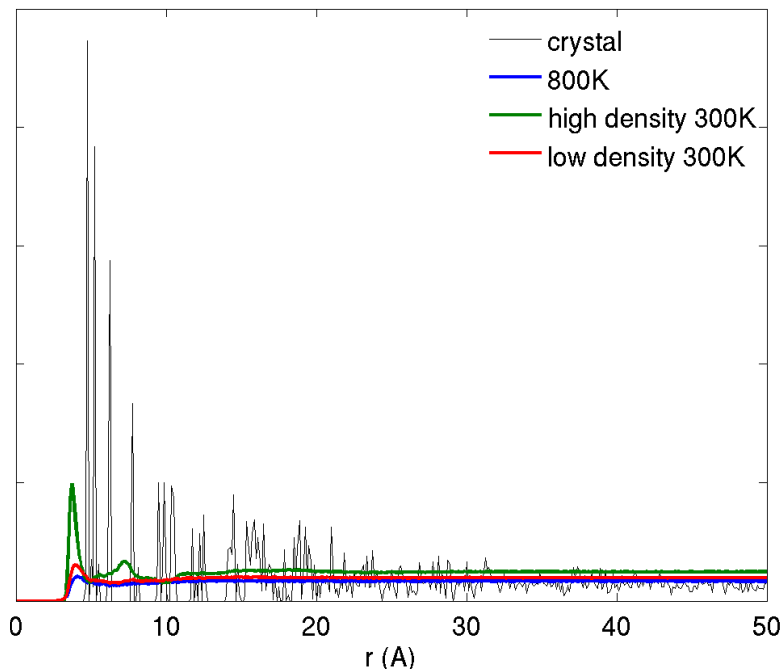


Figure 5-5 The radial distribution functions for the single crystal pentacene (in black), melted phase at 800K (in blue), the high density phase relaxing with fast cooling (in green), and the low density phase relaxing with slow cooling (in green). The data are obtained from 1 ns MD simulation.

Distributions of angles between molecular pairs.

The structures have been further investigated by characterizing the thermal distributions of the angles between each molecular dimer. Here, three orthogonal vectors have been defined for each molecule (see Figure 5-6 a): V_1 is the direction along the long molecular axes; perpendicular to V_1 , V_2 associate with V_1 define the plane of the molecular backbone; V_3 is the vector that orthogonal to this plane. The

thermal distribution of cosine of the angles between neighboring molecules for each of these three vectors are shown in Figure 5-6 b-d. The distance cutoff is 20 Å.

The distributions are in good agreement with experimental observations for a single crystal. On one hand, the directions along the long molecular axes are all parallel leading a sharp peak at cosine value of -1 in the distribution of angles between V_1 vectors (panel b); on the other hand, the single crystalline pentacene has the herringbone angle of $\sim 54^\circ$,¹¹⁹ thus, the peaks around cosine value of ± 0.7 are observed in panel c and d, respectively. The asymmetrical distribution only takes place for the case of crystal by initial definition of the vectors.

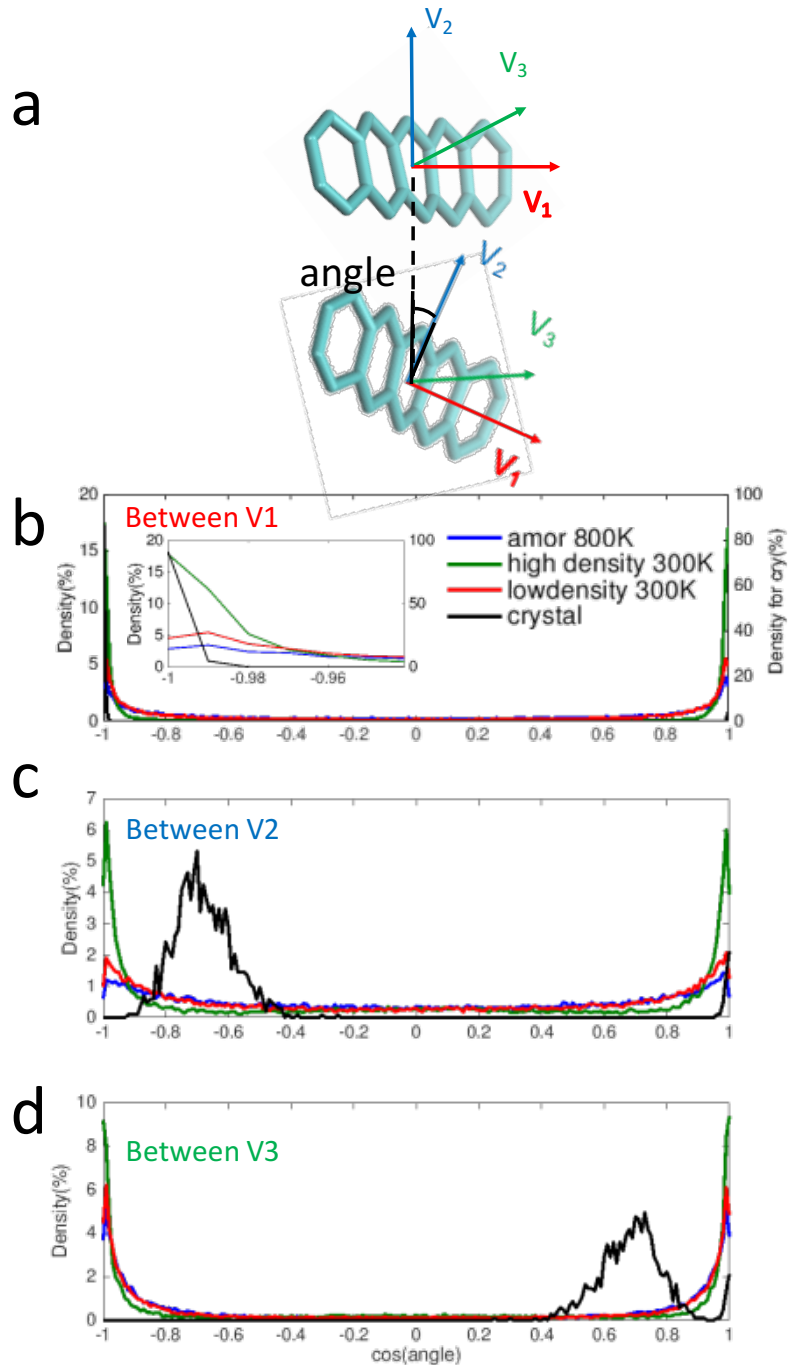


Figure 5-6 (a) Schematic diagram of three orthogonal vectors for each molecule in the disordered pentacene. V_1 is along the long molecular axes; V_1 and V_2 form the plane of the molecular backbone; V_3 is orthogonal to this plane. **(b-d)** The thermal distribution of cosine of the angles between neighboring molecules for each of these three vectors. The data are obtained from 1 ns MD simulation at 300 K.

The low density amorphous sample (red curves) has almost the same features as the melted pentacene (blue curves) in panel b-d, which indicate that it is a complete amorphous solid. By contrast, the high density system has much higher peaks at $\cos(0^\circ)$ and $\cos(180^\circ)$ in all three angle distributions, especially for the one between V_1 vectors, see the zoom-in plot in panel b. It shows that the molecules form favorably cofacial configurations, which explains the polycrystalline domains in Figure 5-4 a.

5.3 CT Results and discussion

5.3.1 Electronic coupling

Electronic coupling matrix elements $|H_{ij}|$ are calculated using AOM method as described in previous chapter. Calculations are performed for all pairs with a centre-to-centre distance within 20 Å. The coupling values versus the intermolecular distance plots are shown in Figure 5-7 (a) and (b) for the high density and low disordered systems, respectively. Panel c shows the distributions of the calculated $|H_{ij}|$ for hole transfer in pentacene. The former system has more pairs with strong couplings than the latter system due to the electronic coupling strongly depends on wave function overlap and decreases exponentially with increasing center to center distance.

In terms of the comparable coupling values in the amorphous system, the 1st shell of neighbours are considered, i.e. the first board peak in $g(r)$ in Figure 5-5 with a centre-to-centre distance within 7 Å. The coupling values cover 7 order of magnitude ranging from 10^{-5} to ~ 100 meV because they are very sensitive to intermolecular distances and

orientational configurations. Furthermore, the mean $|H_{ij}|$ is 24 meV, which is on the same order of magnitude as the nearest neighbour coupling in the bulk and thin films according to Table 4-3. The coupling values in the amorphous system are higher than my initial expectation but they turn out to be reasonable according to the geometry characterization. Figure 5-6 shows us a large portion of molecular pairs perpendicular to each other to some degree.

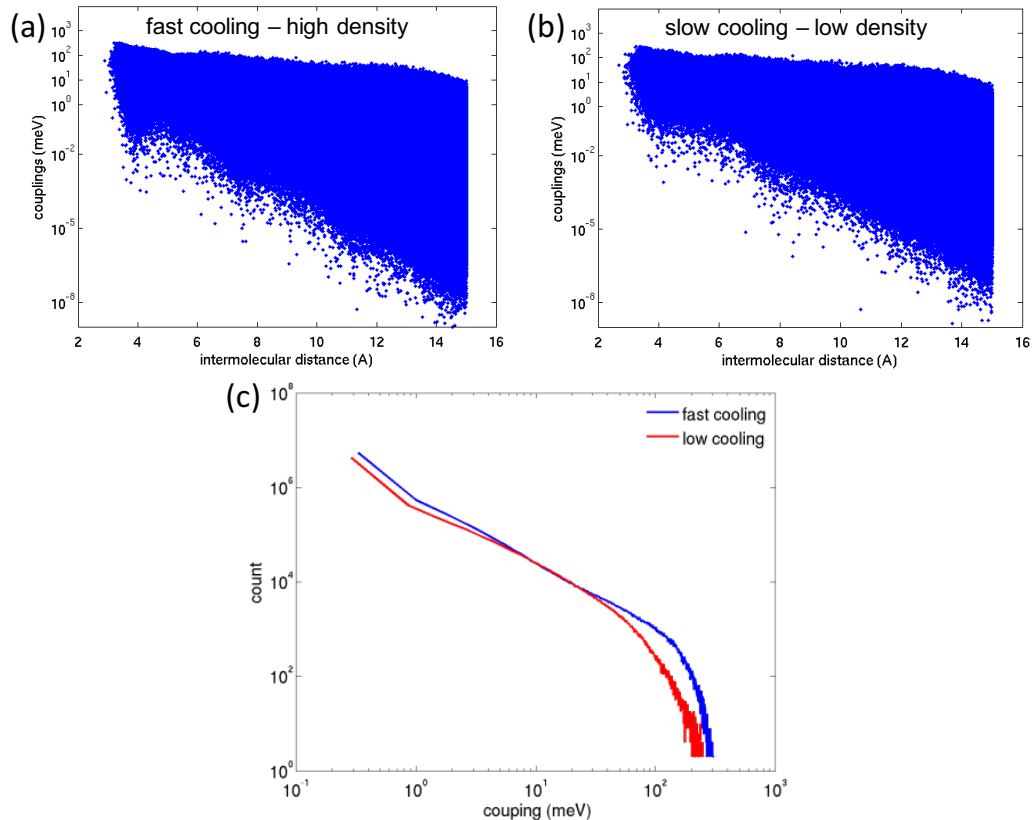


Figure 5-7 (a-b) Electronic coupling matrix elements $|H_{ij}|$ versus intermolecular centre-to-centre distance for (a) the high density disordered pentacene and (b) the low density disordered pentacene. (c) Distribution of $|H_{ij}|$ for hole transfer between nearest neighbor pairs. The data are obtained from 1 ns MD simulation at 300 K.

5.3.2 Charge mobility

Hopping hole mobilities were calculated using Kinetic Monte Carlo (KMC) simulation as before. The eigenvalues of the charge mobility tensor obtained for the structures from 1ns MD are shown in Figure 5-8 (for 300 K). The calculations show that low-density amorphous system has isotropy in mobilities ($0.49 \text{ cm}^2/\text{Vs}$), while high-density disordered system's mobilities are slightly anisotropic: one is $0.55 \text{ cm}^2/\text{Vs}$ for the direction along the most loose packing and the rest two eigenvalues are $0.64 \text{ cm}^2/\text{Vs}$. Reliable estimation of material density is therefore critical for the accurate prediction of hole mobility in amorphous organic materials. The computed mobilties are in good agreement with experimental mobility ($0.3 \text{ cm}^2/\text{Vs}$) of amorphous thin-film transistors.¹²⁸

Clearly, the amorphous pentacene has three-dimensional mobility, which is different from the crystal and the thin films have 2D charge transport within the herringbone layer discussed in previous two chapters. Furthermore, the mobility of the former is a factor of 8 smaller than for the latter. Because the molecules in the amorphous are positioned randomly with respect to each other and the overlap is much smaller than in the crystalline state, the carrier transport is significantly inhibited. Besides, the pairs with small couplings are frequently used as charge hopping sites although their coupling values are significantly smaller than the maximum. In amorphous organics, the pairs with weak couplings form effective charge transport paths that also largely contribute to the mobilities.

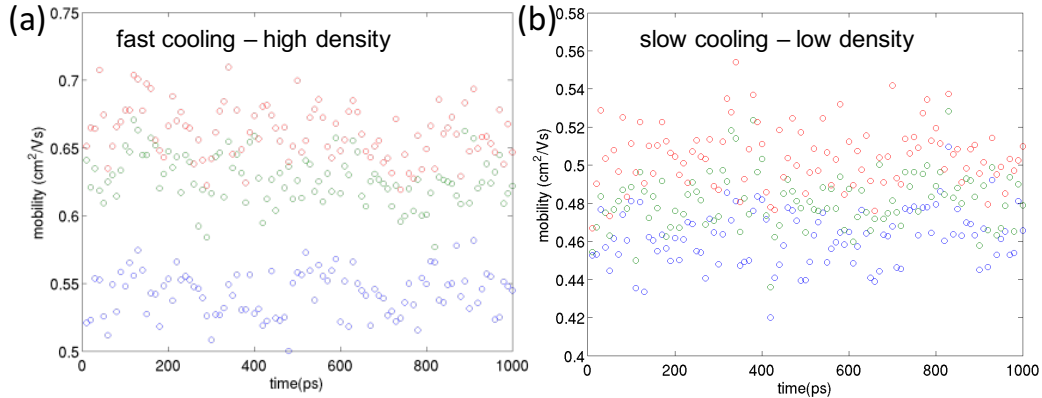


Figure 5-8 Charge hopping mobilities for disordered pentacene at room temperature as obtained from KMC simulation. Data points are instantaneous mobility values for snapshots equidistantly spaced along the 1ns trajectory. Three colors represent three orthorgal eigenvectors of the mobility tensor.

5.4 Summary

In conclusion, the application of hopping theory has been studied in details to predict hole mobility in the disordered (polycrystalline and amorphous) pentacene. I have demonstrated models that incorporates the microscopic structural and electronic details of disordered molecular pentacene.

By simulating the process over a range of cooling rates, I have investigated the effect of morphology. Amorphous pentacene with relative low density and polycrystalline with relative high density are generated by fast cooling and slow cooling, respectively.

By explicitly considering the molecular structure and the disordered intermolecular packing, the results reproduce well the experimental hole electron mobilities for pentacene FET without using any adjustable parameters. I find that large portion of molecular pairs have favorable (shift) cofacial configurations, so that the electronic

couplings of the 1st shell neighboring molecules are sizable. The amorphous pentacene have isotropic charge mobilities and they are a factor of 8 smaller than the highest mobility in single crystal mobilities. In amorphous pentacene, molecular pairs with relatively small H_{ij} are found to form effective paths for charge transport, thus, they largely contribute to μ .

This work described in this chapter along with that in previous two chapters will be presented in a paper on the comparable study of CT in single crystal, crystalline thin films and amorphous pentacene. The paper demonstrates the structure-property relationship of charge transport for OS materials, via analysis of CT parameters, especially coupling distributions, in different polymorph

6 Conclusion and Outlook

6.1 Conclusion

Although OS have already revolutionized the semiconductor market in form of OLEDs and OFETs, there is still enormous potential for rational improvement of their properties, especially their charge carrier mobilities. The current upper limit in organic molecular crystals is an order of magnitude smaller even in highly purified single crystalline samples when compared to inorganic semiconductors (the order of 100 cm²/Vs). In order to improve the efficiency of OSs, much research has been investigated in the last few decades to obtain a better understanding of CT in OS in the single crystalline, polycrystalline, thin films and amorphous.^{129,132,133}

In this thesis, I have demonstrated detailed analysis of the computational characterization of the charge transport properties for a number of application-relevant organic semiconductors. I not only discussed theoretical insight into possible charge transport mechanism, but also delivered some insights into how solid state order impacts on charge transport properties using solids formed by the same molecule: from single crystals, to experimentally characterised ordered thin films to fully disordered amorphous samples.

A computational protocol to predict mobilities for organic molecular materials has been presented. It is the application of the commonly assumed polaron hopping model.

This model is based on the assumption that the charge carrier is localized, i.e. forms a polaron that hops from one molecule to the next. A combination of first principle calculations, molecular dynamics and Kinetic Monte Carlo simulations are used. First principle calculations identify the orbitals relevant for charge transport and explain the electronic couplings vs molecular alignment; molecular dynamics simulation help to get access to realistic molecular motion so that both static and dynamic disorder are taken into consideration for detailed analysis of CT parameters; Kinetic Monte Carlo simulations provide the map of the charge carrier's pathways and then the mobility tensors. The validation of the computational approaches has been done in the case of benzene crystal.

Despite the theoretical problems surrounding the polaron transport model, I find that mobilities based on this model (as obtained from Kinetic Monte Carlo simulation) reproduce very well the room temperature experimental mobility and anisotropy in pentacene and rubrene. However, it fails to reproduce the correct temperature dependence of mobility, predicting a too shallow decay with temperature compared to experiment.

The band mobilities have been also investigated for the case of anthracene crystal. The relaxation time is calculated from the acoustic deformation potential model, and the effective mass is simply obtained from parabolic fit of the valence band maximum (VBM) for holes. I find that van der Waals interaction significantly contributes to the

accurate relaxation time calculations. The computational results show that the band mobilities are approximately one order of magnitude higher than the hopping mobilities, and time-of-flight mobilities are in between. The mobility along the direction with the most likely current in anthracene crystal decreases with temperature as T^{-n} where $n \sim 0.5, 1$ and 1.24 , respectively. The results call for further development of more advanced simulation approaches, such as non-adiabatic molecular dynamics simulation and their scale-up to large, application-relevant systems.

I built the model of few-layer crystalline pentacene thin film, restraint tilt angle, and stabilized them on hexagonal boron nitride in molecular dynamics. The electronic coupling and hops within and across layers have been characterized. The T-shape pairs have the strongest couplings in thin film pentacene like the case in the single crystal, but the averaged couplings are roughly $\frac{1}{2}$ smaller, which lead to significantly smaller mobilities in the thin films compared with that in the single crystal. The transport WL has impact on that within 1L due to horizontal orientation of molecules in the wetting layer, but the transport in 2L is nearly unperturbed from 1L.

With increasing degree of disorder, the amorphous pentacene has low mobility by a factor of 8 smaller than that in the case of a single crystal. Because a large number of molecular pairs have smaller wave function overlap and bigger center to center distance, which essentially leads to weaker electronic coupling. The molecules in 1st neighbouring shell (within center-to-center distance of 3-7 Å) large range of electronic

couplings that cover 7 order of magnitudes. The molecules' thermal average coupling values and orientational configurations are comparable with the nearest P pairs in a single crystal of pentacene. I find that in amorphous organics, even the pairs with weak couplings contribute to the mobilities because they can form effective charge transport paths.

6.2 Outlook

More advanced simulation approaches are necessary to describe the problem of CT in OS such as nonadiabatic molecular dynamics simulation. First in-roads have been made in this regard^{20,39,62,63}, but these methods need to be made more efficient for application to CT in real 3D systems. In addition, several issues of more fundamental nature need to be addressed and their influence on charge mobility calculations investigated. This includes the type of coupling scheme used for nuclear and electronic motion (Ehrenfest vs surface hopping), the correction schemes used for electronic overdecoherence, the problem of trivial surface crossings, and the questions of internal consistency of quantum amplitudes and detailed balance. Our group currently working on these issues within the framework of our recently developed FOB-SH approach and are confident to apply this methodology in the near future to the systems investigated here. A follow-up project has been in process which assesses the application of FOB-SH protocol on small organic molecular system, such as

anthracene. The CT parameters presented in this work provide a sound basis for these future simulations.

References

- (1) Karl, N. Charge carrier transport in organic semiconductors. *Synthetic Metals* **2003**, *133*, 649-657.
- (2) Coropceanu, V.; Cornil, J.; da Silva Filho, D. A.; Olivier, Y.; Silbey, R.; Brédas, J.-L. Charge transport in organic semiconductors. *Chemical Reviews* **2007**, *107*, 926-952.
- (3) Gershenson, M.; Podzorov, V.; Morpurgo, A. Colloquium: Electronic transport in single-crystal organic transistors. *Reviews of Modern Physics* **2006**, *78*, 973.
- (4) Nelson, J.; Kwiatkowski, J. J.; Kirkpatrick, J.; Frost, J. M. Modeling charge transport in organic photovoltaic materials. *Accounts of Chemical Research* **2009**, *42*, 1768-1778.
- (5) Wong, W. S.; Salleo, A. *Flexible electronics: Materials and applications*; Springer Science & Business Media, 2009; Vol. 11.
- (6) Dimitrakopoulos, C. D.; Malenfant, P. R. Organic thin film transistors for large area electronics. *Advanced Materials* **2002**, *14*, 99.
- (7) Jurchescu, O. D.; Baas, J.; Palstra, T. T. M. Effect of impurities on the mobility of single crystal pentacene. *Applied Physics Letters* **2004**, *84*, 3061.
- (8) Jurchescu, O. D.; Baas, J.; Palstra, T. T. Electronic transport properties of pentacene single crystals upon exposure to air. *Applied Physics Letters* **2005**, *87*, 052102.
- (9) Dong, H.; Fu, X.; Liu, J.; Wang, Z.; Hu, W. 25th anniversary article: Key points for high - mobility organic field - effect transistors. *Advanced Materials* **2013**, *25*, 6158-6183.
- (10) Oberhofer, H.; Reuter, K.; Blumberger, J. Charge transport in molecular materials: An assessment of computational methods. *Chemical Reviews* **2017**, *117*, 10319-10357.

- (11) Grozema, F. C.; Siebbeles, L. D. Mechanism of charge transport in self-organizing organic materials. *International Reviews in Physical Chemistry* **2008**, *27*, 87-138.
- (12) Troisi, A. Charge transport in high mobility molecular semiconductors: Classical models and new theories. *Chemical Society Reviews* **2011**, *40*, 2347-2358.
- (13) Gershenson, M. E.; Podzorov, V.; Morpurgo, A. F. Colloquium: Electronic transport in single-crystal organic transistors. *Reviews of Modern Physics* **2006**, *78*, 973-989.
- (14) Fratini, S.; Ciuchi, S. Bandlike motion and mobility saturation in organic molecular semiconductors. *Physical Review Letters* **2009**, *103*, 266601.
- (15) Cheung, D. L.; Troisi, A. Theoretical study of the organic photovoltaic electron acceptor p_cbm: Morphology, electronic structure, and charge localization. *The Journal of Physical Chemistry C* **2010**, *114*, 20479-20488.
- (16) Troisi, A. Charge transport in high mobility molecular semiconductors: Calssical models and new theories. *Chemical Society Reviews* **2011**, *40*, 2347-2358.
- (17) Oberhofer, H.; Blumberger, J. Revisiting electronic couplings and incoherent hopping models for electron transport in crystalline c\$_{60}\$ at ambient temperatures. *Physical Chemistry Chemical Physics*. **2012**, *14*, 13846-13852
- (18) Gajdos, F.; Oberhofer, H.; Dupuis, M.; Blumberger, J. On the inapplicability of electron-hopping models for the organic semiconductor phenyl-c₆₁-butyric acid methyl ester (p_cbm). *The Journal of Physical Chemistry Letters* **2013**, *4*, 1012-1017.
- (19) Gajdos, F.; Oberhofer, H.; Dupuis, M.; Blumberger, J. Correction to “inapplicability of electron-hopping models for the organic semiconductor phenyl-c₆₁-butyric acid methyl ester (p_cbm)”. *The Journal of Physical Chemistry Letters* **2014**, *5*, 2765.

- (20) Ren, J. F.; Vukmirovic, N.; Wang, L. W. Nonadiabatic molecular dynamics simulation for carrier transport in a pentathiophene butyric acid monolayer. *Physical Review B* **2013**, *87*, 205117-205114.
- (21) Ide, J.; Fazzi, D.; Casalegno, M.; Meille, S. V.; Raos, G. Electron transport in crystalline pcbm-like fullerene derivatives: A comparative computational study. *Journal of Materials Chemistry C* **2014**, *2*, 7313-7325.
- (22) Coropceanu, V.; Cornil, J.; da Silva Filho, D. A.; Olivier, Y.; Silbey, R.; Bredas, J. L. Charge transport in organic semiconductors. *Chem Review* **2007**, *107*, 926-952.
- (23) Kim, Y.; Nelson, J.; Zhang, T.; Cook, S.; Durrant, J. R.; Kim, H.; Park, J.; Shin, M.; Nam, S.; Heeney, M.; McCulloch, I.; Ha, C. S.; Bradley, D. D. Distorted asymmetric cubic nanostructure of soluble fullerene crystals in efficient polymer:Fullerene solar cells. *ACS Nano* **2009**, *3*, 2557-2562.
- (24) Grozema, F. C.; Siebbeles, L. D. A. Mechanism of charge transport in self-organizing organic materials. *International Reviews in Physical Chemistry* **2008**, *27*, 87-138.
- (25) Eyring, H. The activated complex in chemical reactions. *The Journal of Chemical Physics* **1935**, *3*, 107-115.
- (26) Zener, C. Non-adiabatic crossing of energy levels. *Proceedings of the Royal Society A* **1932**, *137*, 696-702.
- (27) Landau, L. On the theory of transfer of energy at collisions ii. *Physikalische Zeitschrift der Sowjetunion* **1932**, *2*, 118.
- (28) Blumberger, J. Recent advances in the theory and molecular simulation of biological electron transfer reactions. *Chemical Reviews* **2015**, *115*, 11191-11238.
- (29) Newton, M. D.; Sutin, N. Electron transfer reactions in condensed phases. *Annual Review of Physical Chemistry* **1984**, *35*, 437-480.

- (30) Nitzan, A. *Chemical dynamics in condensed phases: Relaxation, transfer and reactions in condensed molecular systems: Relaxation, transfer and reactions in condensed molecular systems*; Oxford University Press, 2006.
- (31) Spencer, J.; Scalfi, L.; Carof, A.; Blumberger, J. Confronting surface hopping molecular dynamics with marcus theory for a molecular donor–acceptor system. *Faraday Discussions* **2016**.
- (32) Oberhofer, H.; Blumberger, J. Revisiting electronic couplings and incoherent hopping models for electron transport in crystalline c60 at ambient temperatures. *Physical Chemistry Chemical Physics* **2012**, *14*, 13846-13852.
- (33) Marcus, R. A. Electrostatic free energy and other properties of states having nonequilibrium polarization. I. *The Journal of Chemical Physics* **1956**, *24*, 979-989.
- (34) Marcus, R. A. On the theory of oxidation - reduction reactions involving electron transfer. I. *The Journal of Chemical Physics* **1956**, *24*, 966-978.
- (35) Kubas, A.; Hoffmann, F.; Heck, A.; Oberhofer, H.; Elstner, M.; Blumberger, J. Electronic couplings for molecular charge transfer: Benchmarking cdft, fodft, and fodftb against high-level ab initio calculations. *The Journal of Chemical Physics* **2014**, *140*, 104105.
- (36) Gajdos, F.; Valner, S.; Hoffmann, F.; Spencer, J.; Breuer, M.; Kubas, A.; Dupuis, M.; Blumberger, J. Ultrafast estimation of electronic couplings for electron transfer between π -conjugated organic molecules. *Journal of Chemical Theory and Computation* **2014**, *10*, 4653-4660.
- (37) Hoffmann, R. An extended hückel theory. I. Hydrocarbons. *The Journal of Chemical Physics* **1963**, *39*, 1397-1412.
- (38) Oberhofer, H.; Blumberger, J. Charge constrained density functional molecular dynamics for simulation of condensed phase electron transfer reactions. *The Journal of Chemical Physics* **2009**, *131*, 064101.

- (39) Spencer, J.; Gajdos, F.; Blumberger, J. Fob-sh: Fragment orbital-based surface hopping for charge carrier transport in organic and biological molecules and materials. *The Journal of Chemical Physics* **2016**, *145*, 064102.
- (40) Tully, J. C. Nonadiabatic molecular dynamics. *International Journal of Quantum Chemistry* **1991**, *40*, 299-309.
- (41) Oberhofer, H.; Blumberger, J. Revisiting electronic couplings and incoherent hopping models for electron transport in crystalline $c\text{ }60$ at ambient temperatures. *Physical Chemistry Chemical Physics* **2012**, *14*, 13846-13852.
- (42) Blumberger, J.; Lamoureux, G. Reorganization free energies and quantum corrections for a model electron self-exchange reaction: Comparison of polarizable and non-polarizable solvent models. *Molecular Physics* **2008**, *106*, 1597-1611.
- (43) Nitzan, A. *Chemical dynamics in condensed phases: Relaxation, transfer and reactions in condensed molecular systems*; Oxford University Press, 2006.
- (44) Atkins, P.; De Paula, J.; Oxford: Oxford University Press: 2006.
- (45) Norris, J. R. *Markov chains*; Cambridge University Press, 1998.
- (46) Bortz, A. B.; Kalos, M. H.; Lebowitz, J. L. A new algorithm for monte carlo simulation of ising spin systems. *Journal of Computational Physics* **1975**, *17*, 10-18.
- (47) Fishchuk, I.; Kadashchuk, A.; Bässler, H.; Abkowitz, M. Low-field charge-carrier hopping transport in energetically and positionally disordered organic materials. *Physical Review B* **2004**, *70*, 245212.
- (48) Stephan, J.; Liemant, A.; Albrecht, F.; Brehmer, L. Interplay of polaronic and disorder effects on electronic charge transport. *Synthetic Metals* **2000**, *109*, 327-331.
- (49) Stephan, J.; Schrader, S.; Brehmer, L. Monte carlo simulations of charge transport in molecular solids: A modified miller abrahams type jump rate approach. *Synthetic Metals* **2000**, *111*, 353-357.

- (50) Joshi, R.; Ferry, D. Effect of multi-ion screening on the electronic transport in doped semiconductors: A molecular-dynamics analysis. *Physical Review B* **1991**, *43*, 9734.
- (51) Kerisit, S.; Rosso, K. M. Kinetic monte carlo model of charge transport in hematite (α -fe₂o₃). *The Journal of Chemical Physics* **2007**, *127*, 124706.
- (52) Djurabekova, F.; Malerba, L.; Domain, C.; Becquart, C. Stability and mobility of small vacancy and copper-vacancy clusters in bcc-fe: An atomistic kinetic monte carlo study. *Nuclear Instruments and Methods in Physics Research Section B: Beam Interactions with Materials and Atoms* **2007**, *255*, 47-51.
- (53) Zeng, B.; Li, M.; Zhang, X.; Yi, Y.; Fu, L.; Long, M. First-principles prediction of the electronic structure and carrier mobility in hexagonal boron phosphide sheet and nanoribbons. *The Journal of Physical Chemistry C* **2016**, *120*, 25037-25042.
- (54) Wang, G. Density functional study on the increment of carrier mobility in armchair graphene nanoribbons induced by stone-wales defects. *Physical Chemistry Chemical Physics* **2011**, *13*, 11939-11945.
- (55) Kobayashi, H.; Kobayashi, N.; Hosoi, S.; Koshitani, N.; Murakami, D.; Shirasawa, R.; Kudo, Y.; Hobara, D.; Tokita, Y.; Itabashi, M. Hopping and band mobilities of pentacene, rubrene, and 2,7-diethyl[1]benzothieno[3,2-b][1]benzothiophene (c8-btbt) from first principle calculations. *The Journal of Chemical Physics* **2013**, *139*, 014707.
- (56) Fedorov, I. A. First-principles study of band structures of anthracene and tetracene under pressure. *Materials Chemistry and Physics* **2017**, *199*, 173-178.
- (57) Szulczewski, G.; Sanvito, S.; Coey, M. A spin of their own. *Nature Materials* **2009**, *8*, 693.
- (58) Bardeen, J. J. Bardeen and w. Shockley, phys. Rev. 80, 72 (1950). *Physical Review*. **1950**, *80*, 72.

- (59) Wilson, E. Electron motion in one-dimensional semiconductors. *Journal of Physics C: Solid State Physics* **1982**, *15*, 3733.
- (60) Troisi, A. *The Journal of Chemical Physics* **2011**, *134*, 034702.
- (61) Wang, L.; Beljonne, D. Flexible surface hopping approach to model the crossover from hopping to band-like transport in organic crystals. *The Journal of Physical Chemistry Letters* **2013**, *4*, 1888-1894.
- (62) Heck, A.; Kranz, J. J.; Kuban, T.; Elstner, M. Multi-scale approach to non-adiabatic charge transport in high-mobility organic semiconductors. *Journal of Chemical Theory and Computation* **2015**, *11*, 5068-5082.
- (63) Pal, S.; Trivedi, D.; Akimov, A. V.; Aradi, B.; Frauenheim, T.; Prezhdo, O. V. Nonadiabatic molecular dynamics for thousand atom systems: A tight-binding approach toward pyxaid. *Journal of Chemical Theory and Computation* **2016**, *12*, 1436–1448.
- (64) Prezhdo, O. V.; Rossky, P. J. Evaluation of quantum transition rates from quantum-classical molecular dynamics simulations. *The Journal of Chemical Physics* **1997**, *107*, 5863-5878.
- (65) Fang, J. Y.; Hammes-Schiffer, S. Improvement of the internal consistency in trajectory surface hopping. *Journal of Physical Chemistry A* **1999**, *103*, 9399-9407.
- (66) Jasper, A. W.; Nangia, S.; Zhu, C.; Truhlar, D. G. Non-born-oppenheimer molecular dynamics. *Accounts of Chemical Research* **2006**, *39*, 101-108.
- (67) Granucci, G.; Persico, M. Critical appraisal of the fewest switches algorithm for surface hopping. *The Journal of Chemical Physics* **2007**, *126*, 134114.
- (68) Landry, B. R.; Subotnik, J. E. How to recover marcus theory with fewest switches surface hopping: Add just a touch of decoherence. *The Journal of Chemical Physics* **2012**, *137*, 22A513-513.

- (69) Nelson, T.; Fernandez-Alberti, S.; Roitberg, A. E.; Tretiak, S. Nonadiabatic excited-state molecular dynamics: Treatment of electronic decoherence. *The Journal of Chemical Physics* **2013**, *138*, 224111.
- (70) Nelson, T.; Fernandez-Alberti, S.; Roitberg, A. E.; Tretiak, S. Artifacts due to trivial unavoidable crossings in the modeling of photoinduced energy transfer dynamics in extended conjugated molecules. *Chemical Physics Letters* **2013**, *590*, 208-213.
- (71) Wang, L.; Prezhdo, O. V. A simple solution to the trivial crossing problem in surface hopping. *The Journal of Physical Chemistry Letters* **2014**, *5*, 713-719.
- (72) Jain, A.; Subotnik, J. E. Surface hopping, transition state theory, and decoherence. Ii. Thermal rate constants and detailed balance. *The Journal of Chemical Physics* **2015**, *143*, 134107.
- (73) Sifain, A. E.; Wang, L. J.; Prezhdo, O. V. Communication: Proper treatment of classically forbidden electronic transitions significantly improves detailed balance in surface hopping. *The Journal of Chemical Physics* **2016**, *144*, 211102.
- (74) Chen, H.-T.; Reichman, D. R. On the accuracy of surface hopping dynamics in condensed phase non-adiabatic problems. *The Journal of Chemical Physics* **2016**, *144*, 094104.
- (75) Carof, A.; Giannini, S.; Blumberger, J. Detailed balance, internal consistency, and energy conservation in fragment orbital-based surface hopping. *The Journal of Chemical Physics* **2017**, *147*, 214113.
- (76) Nayak, S. K.; Sathishkumar, R.; Row, T. G. Directing role of functional groups in selective generation of c-h π interactions: In situ cryo-crystallographic studies on benzyl derivatives. *CrystEngComm* **2010**, *12*, 3112-3118.
- (77) Jurchescu, O. D.; Meetsma, A.; Palstra, T. T. Low-temperature structure of rubrene single crystals grown by vapor transport. *Acta Crystallographica Section B: Structural Science* **2006**, *62*, 330-334.

- (78) Siegrist, T.; Kloc, C.; Schön, J. H.; Batlogg, B.; Haddon, R. C.; Berg, S.; Thomas, G. A. Enhanced physical properties in a pentacene polymorph. *Angewandte Chemie International Edition* **2001**, *40*, 1732-1736.
- (79) David, W. I. F.; Ibberson, R. M.; Matthewman, J. C.; Prassides, K.; Dennis, T. J. S.; Hare, J. P.; Kroto, H. W.; Taylor, R.; Walton, D. R. M. Crystal-structure and bonding of ordered c60. *Nature* **1991**, *353*, 147-149.
- (80) Mason, R. The crystallography of anthracene at 95 K and 290 K. *Acta Crystallographica* **1964**, *17*, 547-555.
- (81) Cheng, Y. C.; Silbey, R. J.; da Silva Filho, D. A.; Calbert, J. P.; Cornil, J.; Brédas, J. L. Three-dimensional band structure and bandlike mobility in oligoacene single crystals: A theoretical investigation. *The Journal of Chemical Physics* **2003**, *118*, 3764-3774.
- (82) da Silva Filho, D. A.; Kim, E. G.; Brédas, J. L. Transport properties in the rubrene crystal: Electronic coupling and vibrational reorganization energy. *Advanced Materials* **2005**, *17*, 1072-1076.
- (83) Heiney, P. A. Structure, dynamics and ordering transition of solid c60. *Journal of Physics and Chemistry of Solids* **1992**, *53*, 1333-1352.
- (84) Heiney, P. A. Structure, dynamics and ordering transition of solid c60. *The fullerenes*; Elsevier: 1993, p 163-182.
- (85) Frisch, M.; Trucks, G.; Schlegel, H.; Scuseria, G.; Robb, M.; Cheeseman, J.; Scalmani, G.; Barone, V.; Mennucci, B.; Petersson, G. Gaussian 09 c. 01. *Gaussian Inc., Wallingford CT* **2009**.
- (86) Andreoni, W.; Curioni, A. New advances in chemistry and materials science with cpmd and parallel computing. *Parallel Computing* **2000**, *26*, 819-842.
- (87) Case, D. A.; Babin, V.; Berryman, J.; Betz, R.; Cai, Q.; Cerutti, D.; Cheatham Iii, T.; Darden, T.; Duke, R.; Gohlke, H. Amber 14. **2014**.

- (88) Wang, J.; Wolf, R. M.; Caldwell, J. W.; Kollman, P. A.; Case, D. A. Development and testing of a general amber force field. *Journal of Computational Chemistry* **2004**, *25*, 1157-1174.
- (89) Bacon, G.; Curry, N. t.; Wilson, S. In *Proceedings of the Royal Society of London A: Mathematical, Physical and Engineering Sciences*; The Royal Society: 1964; Vol. 279, p 98-110.
- (90) Siegrist, T.; Kloc, C.; Schon, J. H.; Batlogg, B.; Haddon, R. C.; Berg, S.; Thomas, G. A. Enhanced physical properties in a pentacene polymorph. *Angewandte Chemie International Edition* **2001**, *40*, 1732-1736.
- (91) Jurchescu, O. D.; Meetsma, A.; Palstra, T. T. Low-temperature structure of rubrene single crystals grown by vapor transport. *Acta Crystallographica B* **2006**, *62*, 330-334.
- (92) Phillips, J. C.; Braun, R.; Wang, W.; Gumbart, J.; Tajkhorshid, E.; Villa, E.; Chipot, C.; Skeel, R. D.; Kale, L.; Schulten, K. Scalable molecular dynamics with namd. *Journal of Computational Chemistry* **2005**, *26*, 1781-1802.
- (93) David, W.; Ibberson, R.; Jeffrey, G.; Ruble, J. The crystal structure analysis of deuterated benzene and deuterated nitromethane by pulsed-neutron powder diffraction: A comparison with single crystal neutron diffraction analysis. *Physica B: Condensed Matter* **1992**, *180*, 597-600.
- (94) Jeffrey, G.; Ruble, J.; McMullan, R.; Pople, J. In *Proceedings of the Royal Society of London A: Mathematical, Physical and Engineering Sciences*; The Royal Society: 1987; Vol. 414, p 47-57.
- (95) Yamagata, H.; Norton, J.; Hontz, E.; Olivier, Y.; Beljonne, D.; Brédas, J.-L.; Silbey, R. J.; Spano, F. The nature of singlet excitons in oligoacene molecular crystals. *The Journal of Chemical Physics* **2011**, *134*, 204703.
- (96) Ahn, T.-S.; Müller, A. M.; Al-Kaysi, R. O.; Spano, F. C.; Norton, J. E.; Beljonne, D.; Brédas, J.-L.; Bardeen, C. J. Experimental and theoretical study of

- temperature dependent exciton delocalization and relaxation in anthracene thin films. *The Journal of Chemical Physics* **2008**, *128*, 054505.
- (97) Zhang, X.; Zhou, Q.; Huang, Y.; Li, Z.; Zhang, Z. Contrastive analysis of the raman spectra of polychlorinated benzene: Hexachlorobenzene and benzene. *Sensors* **2011**, *11*, 11510-11515.
- (98) Baumeier, B.; Kirkpatrick, J.; Andrienko, D. Density-functional based determination of intermolecular charge transfer properties for large-scale morphologies. *Physical Chemistry Chemical Physics*. **2010**, *12*, 11103-11113.
- (99) Kobayashi, H.; Kobayashi, N.; Hosoi, S.; Koshitani, N.; Murakami, D.; Shirasawa, R.; Kudo, Y.; Hobara, D.; Tokita, Y.; Itabashi, M. Hopping and band mobilities of pentacene, rubrene, and 2,7-dioctyl[1]benzothieno[3,2-b][1]benzothiophene (c8-btbt) from first principle calculations. *The Journal of Chemical Physics* **2013**, *139*, 014707.
- (100) Sokolov, A. N.; Atahan-Evrenk, S.; Mondal, R.; Akkerman, H. B.; Sanchez-Carrera, R. S.; Granados-Focil, S.; Schrier, J.; Mannsfeld, S. C.; Zoombelt, A. P.; Bao, Z.; Aspuru-Guzik, A. From computational discovery to experimental characterization of a high hole mobility organic crystal. *Nature Communications* **2011**, *2*, 437.
- (101) Gajdos, F.; Oberhofer, H.; Dupuis, M.; Blumberger, J. On the inapplicability of electron-hopping models for the organic semiconductor phenyl-c61-butyric acid methyl ester (pcbm). *The Journal of Physical Chemistry Letters* **2013**, *4*, 1012-1017.
- (102) Wang, L.; Beljonne, D. Flexible surface hopping approach to model the crossover from hopping to band-like transport in organic crystals. *The Journal of Physical Chemistry Letters* **2013**, *4*, 1888-1894.
- (103) Ren, J. F.; Vukmirovic, N.; Wang, L. W. Nonadiabatic molecular dynamics simulation for carrier transport in a pentathiophene butyric acid monolayer. *Physical Review. B* **2013**, *87*, 205117-205114.

- (104) Troisi, A. Dynamic disorder in molecular semiconductors: Charge transport in two dimensions. *The Journal of Chemical Physics* **2011**, *134*, 034702.
- (105) Troisi, A. Prediction of the absolute charge mobility of molecular semiconductors: The case of rubrene. *Adv. Mater.* **2007**, *19*, 2000-2004.
- (106) Podzorov, V.; Menard, E.; Borissov, A.; Kiryukhin, V.; Rogers, J. A.; Gershenson, M. E. Intrinsic charge transport on the surface of organic semiconductors. *Physical Review Letters* **2004**, *93*, 086602.
- (107) Podzorov, V.; Menard, E.; Rogers, J. A.; Gershenson, M. E. Hall effect in the accumulation layers on the surface of organic semiconductors. *Physical Review Letters* **2005**, *95*, 226601.
- (108) Lee, J. Y.; Roth, S.; Park, Y. W. Anisotropic field effect mobility in single crystal pentacene. *Applied Physics Letters* **2006**, *88*, 252106-252106.
- (109) Jurchescu, O. D.; Baas, J.; Palstra, T. T. M. Effect of impurities on the mobility of single crystal pentacene. *Applied Physics Letters* **2004**, *84*, 3061-3063.
- (110) Frankevich, E.; Maruyama, Y.; Ogata, H. Mobility of charge carriers in vapor-phase grown c60 single crystal. *Chemical Physics Letters* **1993**, *214*, 39-44.
- (111) Sundar, V. C.; Zaumseil, J.; Podzorov, V.; Menard, E.; Willett, R. L.; Someya, T.; Gershenson, M. E.; Rogers, J. A. Elastomeric transistor stamps: Reversible probing of charge transport in organic crystals. *Science* **2004**, *303*, 1644-1646.
- (112) Zeis, R.; Besnard, C.; Siegrist, T.; Schlockermann, C.; Chi, X.; Kloc, C. Field effect studies on rubrene and impurities of rubrene. *Chemistry of Materials* **2006**, *18*, 244-248.
- (113) Ling, M.-M.; Reese, C.; Briseno, A. L.; Bao, Z. Non-destructive probing of the anisotropy of field-effect mobility in the rubrene single crystal. *Synth. Met* **2007**, *157*, 257-260.
- (114) Karl, N.; Marktanner, J. Electron and hole mobilities in high purity anthracene single crystals. *Molecular Crystals and Liquid Crystals Science and Technology. Section A. Molecular Crystals and Liquid Crystals* **2006**, *355*, 149-173.

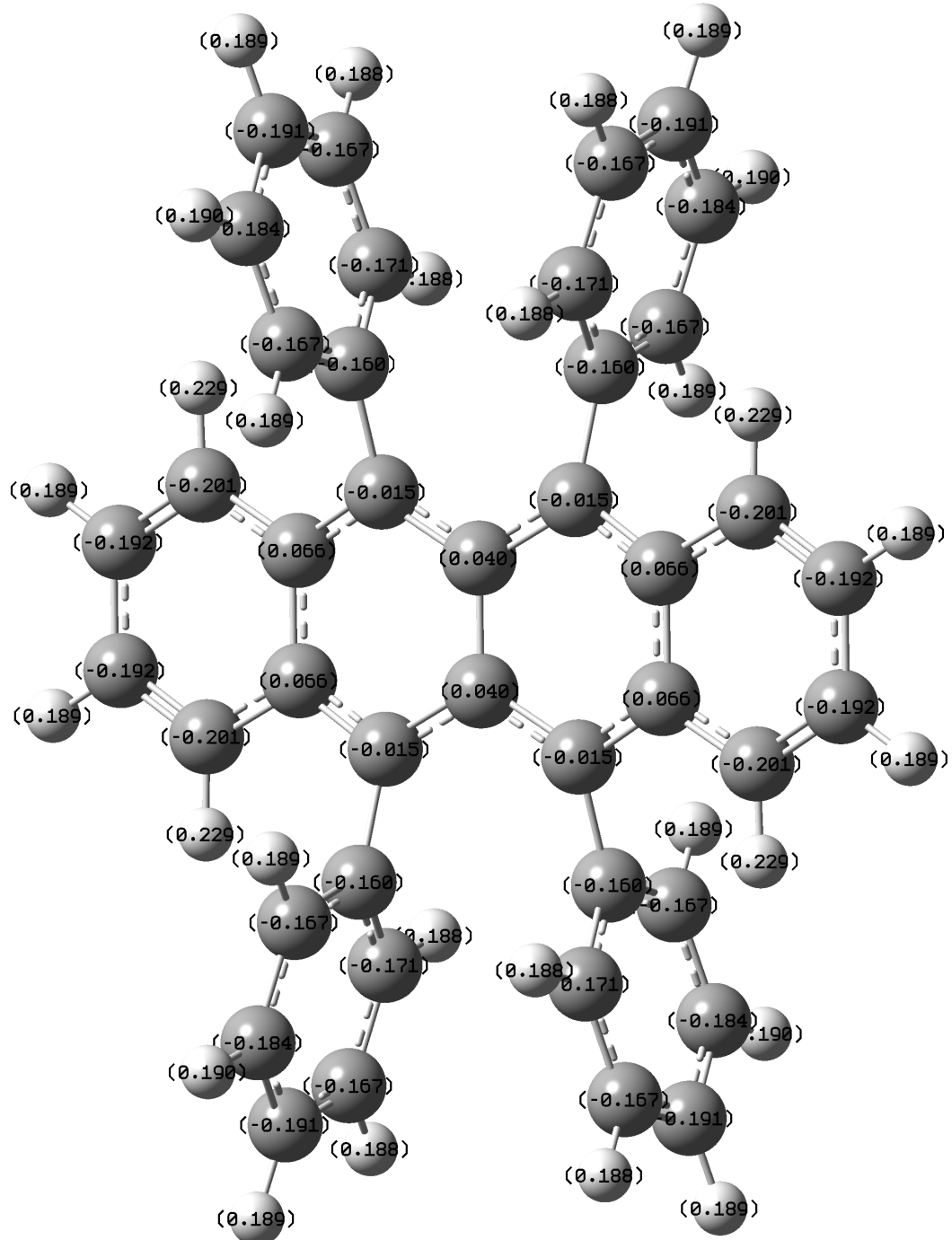
- (115) Perdew, J. P.; Burke, K.; Ernzerhof, M. Generalized gradient approximation made simple. *Physical Review Letters* **1996**, *77*, 3865.
- (116) Monkhorst, H. J.; Pack, J. D. Special points for brillouin-zone integrations. *Physical Review B* **1976**, *13*, 5188-5192.
- (117) Grimme, S. Semiempirical gga - type density functional constructed with a long - range dispersion correction. *Journal of Computational Chemistry* **2006**, *27*, 1787-1799.
- (118) Zhang, Y.; Qiao, J.; Gao, S.; Hu, F.; He, D.; Wu, B.; Yang, Z.; Xu, B.; Li, Y.; Shi, Y.; Ji, W.; Wang, P.; Wang, X.; Xiao, M.; Xu, H.; Xu, J. B.; Wang, X. Probing carrier transport and structure-property relationship of highly ordered organic semiconductors at the two-dimensional limit. *Physical Review Letters* **2016**, *116*, 016602.
- (119) Nabok, D.; Puschnig, P.; Ambrosch-Draxl, C.; Werzer, O.; Resel, R.; Smilgies, D.-M. Crystal and electronic structures of pentacene thin films from grazing-incidence x-ray diffraction and first-principles calculations. *Physical Review B* **2007**, *76*, 235322.
- (120) Harada, Y.; Ozaki, H.; Ohno, K. Selective observation of outermost surface layer during epitaxial growth by penning-ionization electron spectroscopy: Pentacene on graphite. *Physical Review Letters* **1984**, *52*, 2269.
- (121) Wang, Y.; Ji, W.; Shi, D.; Du, S.; Seidel, C.; Ma, Y.; Gao, H.-J.; Chi, L.; Fuchs, H. Structural evolution of pentacene on a ag (110) surface. *Physical Review B* **2004**, *69*, 075408.
- (122) Wang, X.; Broch, K.; Scholz, R.; Schreiber, F.; Meixner, A. J.; Zhang, D. Topography-correlated confocal raman microscopy with cylindrical vector beams for probing nanoscale structural order. *The Journal of Physical Chemistry Letters* **2014**, *5*, 1048-1054.

- (123) Chen, W.; Huang, H.; Thye, A.; Wee, S. Molecular orientation transition of organic thin films on graphite: The effect of intermolecular electrostatic and interfacial dispersion forces. *Chemical Communications* **2008**, 4276-4278.
- (124) Zhao, Y.; Wu, Q.; Chen, Q.; Wang, J. Molecular self-assembly on two-dimensional atomic crystals: Insights from molecular dynamics simulations. *The Journal of Physical Chemistry Letters* **2015**, 6, 4518-4524.
- (125) Zhao, Y.; Wu, Q.; Chen, Q.; Wang, J. Molecular self-assembly on two-dimensional atomic crystals: Insights from molecular dynamics simulations. *The Journal of Physical Chemistry Letters* **2015**, 6, 4518-4524.
- (126) Tessler, N.; Preezant, Y.; Rappaport, N.; Roichman, Y. Charge transport in disordered organic materials and its relevance to thin - film devices: A tutorial review. *Advanced Materials* **2009**, 21, 2741-2761.
- (127) Eiermann, R.; Parkinson, G.; Bässler, H.; Thomas, J. Structural investigations of amorphous tetracene and pentacene by low-temperature electron diffraction. *The Journal of Physical Chemistry* **1983**, 87, 544-551.
- (128) Zhu, Z.-T.; Mason, J. T.; Dieckmann, R.; Malliaras, G. G. Humidity sensors based on pentacene thin-film transistors. *Applied Physics Letters* **2002**, 81, 4643-4645.
- (129) Kwiatkowski, J. J.; Frost, J. M.; Nelson, J. The effect of morphology on electron field-effect mobility in disordered c60 thin films. *Nano Letters* **2009**, 9, 1085-1090.
- (130) Wang, J.; Wolf, R. M.; Caldwell, J. W.; Kollman, P. A.; Case, D. A. Development and testing of a general amber force field. *Journal of Computational Chemistry* **2004**, 25, 1157-1174.
- (131) Sato, N.; Seki, K.; Inokuchi, H.; Harada, Y. Photoemission from an amorphous pentacene film. *Chemical physics* **1986**, 109, 157-162.
- (132) Fornari, R. P.; Troisi, A. Theory of charge hopping along a disordered polymer chain. *Physical Chemistry Chemical Physics* **2014**, 16, 9997-10007.

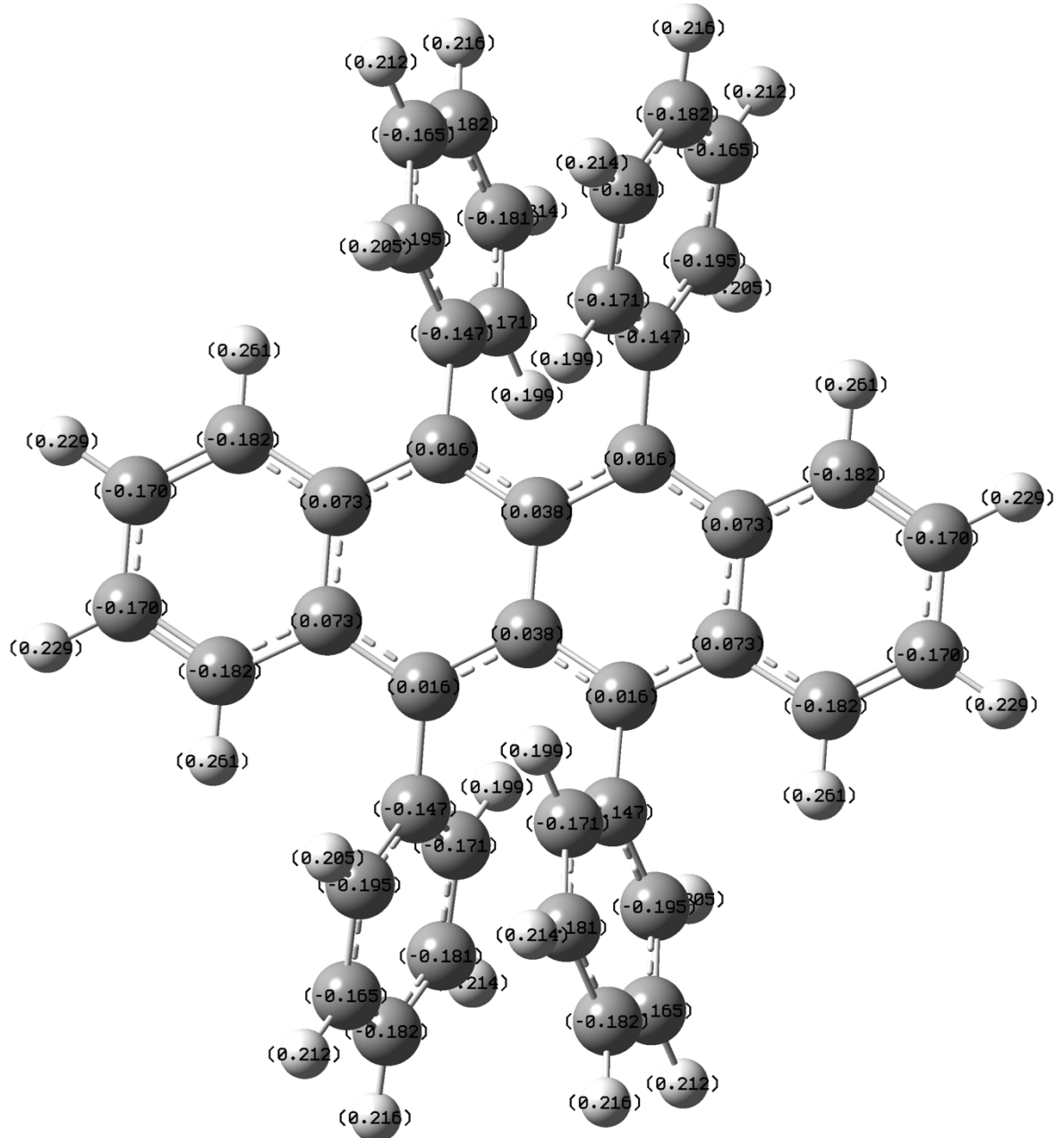
Reference

- (133) Troisi, A. Charge transport in high mobility molecular semiconductors: Classical models and new theories. *Chemical Society Reviews* **2011**, *40*, 2347-2358.

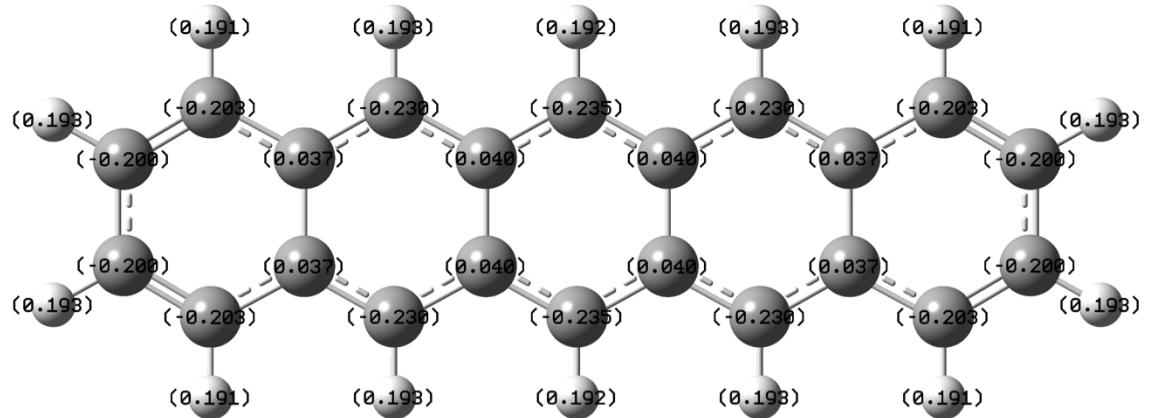
Appendix



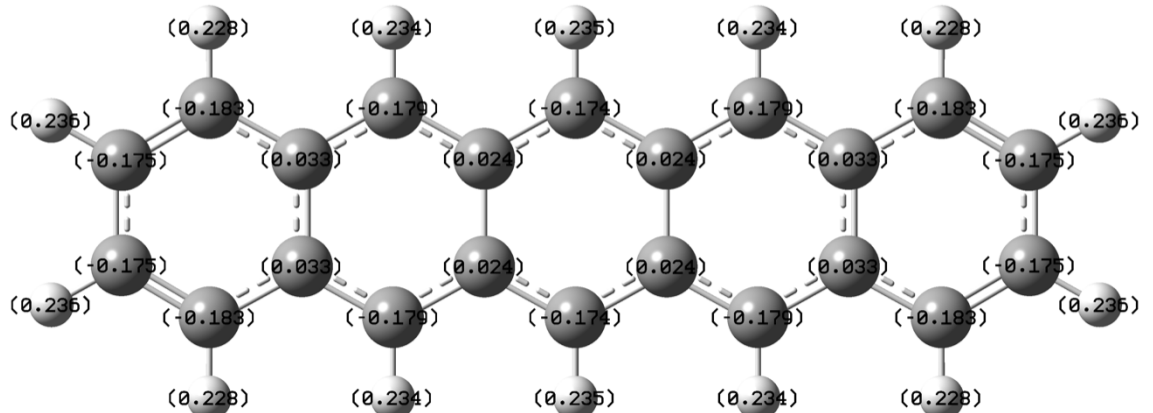
(a)



(b)

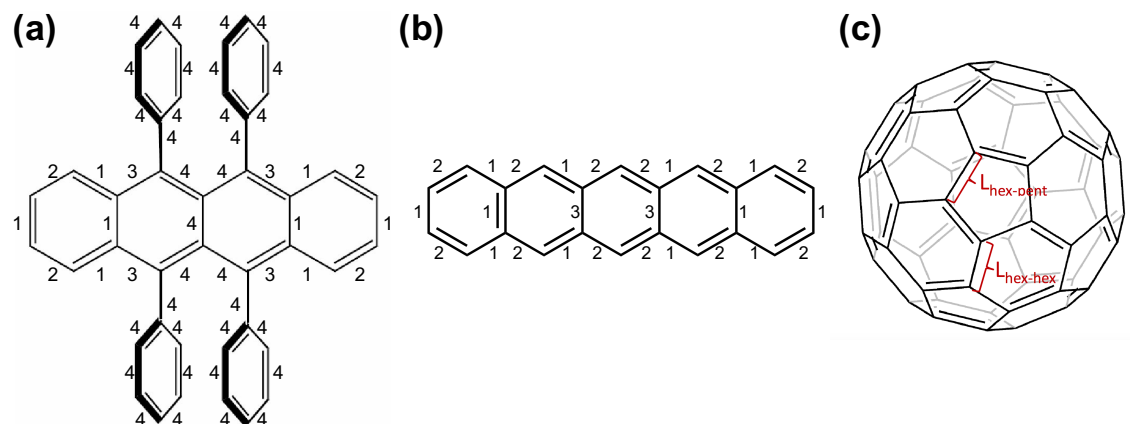


(c)



(d)

Figure S1. Atomic charges of carbon for the molecules simulated in this work, in neutral and charged states: (a) neutral rubrene (b) [rubrene]⁺ (c) neutral pentacene (d) [pentacene]⁺. Each atom in neutral C₆₀ has zero charge and in C₆₀⁻ -0.01667e (not shown).



rubrene

pentacene

 C_60

Bond type	Neutral	Charged	Bond type	Neutral	Charged	Bond type	Neutral	Charged
1	1.387	1.366	1	1.387	1.377	hex-hex	1.401	1.405
2	1.387	1.406	2	1.387	1.397	hex-pent	1.458	1.454
3	1.387	1.411	3	1.387	1.387			
4	1.387	1.387	C-H	1.087	1.087			
C-H	1.087	1.087						

Figure S2. The bond lengths for (a) rubrene (b) pentacene (c) C_60 in neutral and charged states.

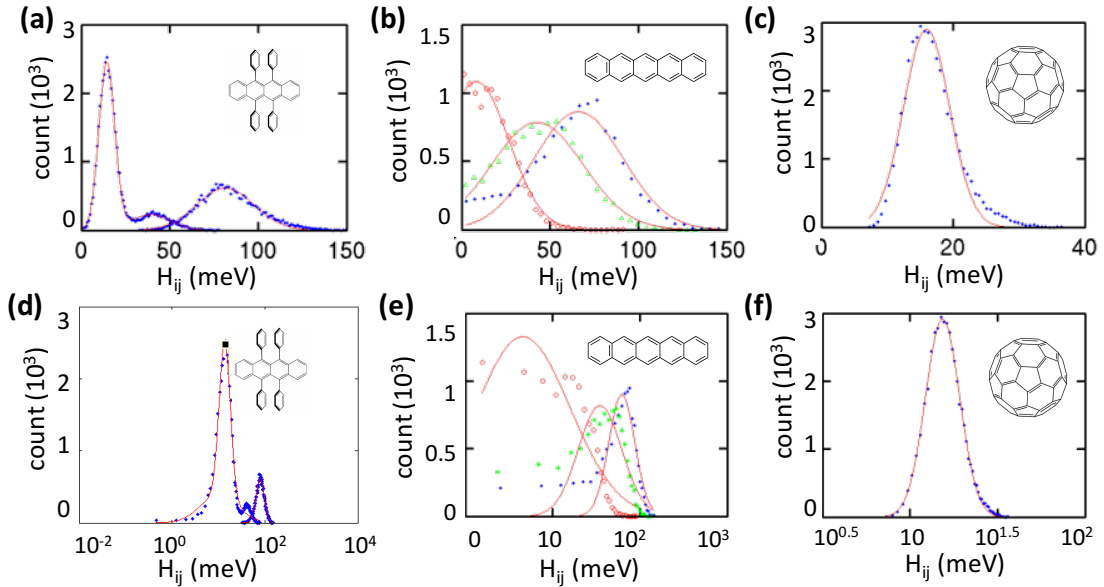


Figure S3 The points show the distribution of electronic coupling matrix elements $|H_{ij}|$ for hole transfer between nearest neighbor pairs in rubrene (a) and (d), pentacene (b) and (e), and for electron transfer in C₆₀ (c) and (f). The data are obtained from 1 ns MD simulation at 300 K. The information of the corresponding pairs can be found below in Figure 3-16 (d)-(f). The red solid lines are Gaussians fitting for each set of $|H_{ij}|$ values at linear scale in (a)-(c) and log scale in (d)-(f).

Protocol of parameterize amber force field to reproduce DFT reorganization energy

1. Download an experimental single crystal structure from CCDC. The structure file is normally a Crystallographic Information File (cif), e.g. rubrene.cif, which is a standard text file format for representing crystallographic information.
2. Covert *.cif to a target format using MERCURY (also from CCDC), e.g. *.mol2, *.pbe, *.xyz . Now, a file includes a single molecule is used for the parameterization.

If a unit cell or crystal structure is needed later on, MERCURY can also generates them. A unit cell structure can be duplicated to crystal structure in

MERCURY by calculation => packing (up to $10 \times 10 \times 10$ unit cell). Alternatively, a simple python code can generate crystal structure for the desired size.

3. Calculate DFT reorganisation energy using 4-point scheme, and extract key parameters including equilibrium bond lengths and point charges.
 - Do geometry optimization calculations for a neutral molecule and a charged molecule. And then, extract the total energies of GnEn and GcEc, respectively.
 - Extract optimized coordinates from these two outputs and then calculate the energies of GnEc and GcEn.
 - Reorganization energy = $GnEc + GcEn - GnEn - GcEc$ (It is the reorganization energy for a pair with infinite distance)
 - Extract information of key parameters form these DFT simulations and calculate point charge differences and bond length differences (growing/shrinking/ unchanged) for later usage.
4. Change the equilibrium bond lengths and point charges in the charged molecule in the force field to reproduce the differences between the charged and neutral molecule calculated by DFT that from the last step in the point 3. When a charge has been put in a neutral molecule, the equilibrium C-C bond will grow, shrink or unchanged (Figure S4 takes the rubrene as an example). Adjust the equilibrium bond distances slightly in the charged molecule force field until the force field can reproduce DFT reorganization energy.

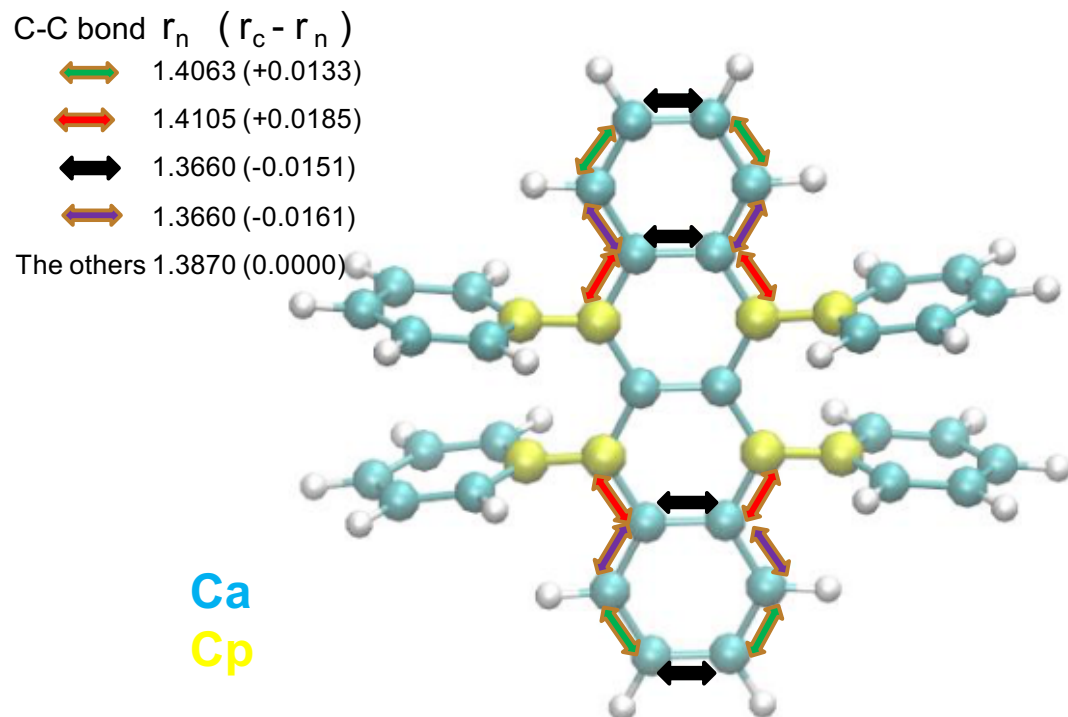


Figure S4. A schematic diagram of rubrene with bond lengths in the neutral state (r_n) and bond length changes ($r_c - r_n$) compared with the charged state in the unit of Å. The equilibrium C-C bond will grow (“+”), shrink (“-”) or unchanged compared with the neutral state. In AMBER force field, two C atoms have been identified, Ca (blue) and Cp (yellow). These two C atoms are not chemically identity in rubrene: The former is a sp^2 aromatic carbon in general and the latter is a sp^2 aromatic carbon linked to an aromatic ring.